TOPOLOGY OPTIMIZATION OF CONVECTIVE COOLING SYSTEM DESIGNS

by

Kyungjun Lee

A dissertation submitted in partial fulfillment
of the requirements for the degree of
Doctor of Philosophy
(Mechanical Engineering)
in The University of Michigan
2012

Doctoral Committee:

Professor Noboru Kikuchi, Chair
Professor Greg Hulbert
Professor Kenneth G. Powell
Research Scientist Zheng-Dong Ma

To my family

ACKNOWLEDGEMENTS

I would like to express my appreciation to my advisor, Professor Noboru Kikuchi for his gentle guidance, great inspiration and financial support during my doctoral studies at the University of Michigan. I also would like to sincerely acknowledge the helpful suggestions and criticisms made by my doctoral committee members, Professor Kenneth G. Powell, Professor Gregory M. Hulbert, Professor Kazuhiro Saitou and Dr. Zheng-Dong Ma. I would like to express my gratitude to Professor Yoon Young Kim and Professor Seungjae Min, for their guidance and advice in my research.

I wish to express my special thanks to Dr. Jeong Hun Seo, Dr. Jaewook Lee and Dr. Youngwon Hahn, who gave me a great help when studying the fundamental of topology optimization theory, for their kindness and friendship. My special thanks are expressed to Dr. Huerta Jill and Dr. Roann Altman for their tutoring me with writing in English.

Finally, I am grateful to my family and all my friends who physically and mentally support me to get through difficult times. This work would not have been possible without the support and encouragement of my parents, my sisters, and many others with whom I shared memories during my studies in Ann Arbor.

TABLE OF CONTENTS

LIST OF FIGURES

LIST OF TABLES

ABSTRACT

This research investigates an approach to finding the optimal geometry of convective cooling system structures for the enhancement of cooling performance. To predict the cooling effect of convective heat transfer, flow analysis is performed by solving the Brinkman-penalized Navier-Stokes equation, and the temperature profile is obtained from the homogenized thermal-transport equation. For accurate and cost-effective analysis, stabilized finite element methods (FEM) and the adjoint sensitivity method for the multiphysics system are implemented. Several stabilization methods with different definitions of their stabilization tensors and the Newton-Raphson iteration method are introduced to solve the governing equations.

This study investigates numerical instabilities, such as velocity and pressure oscillation at the fluid-solid interfaces, which result from the fact that the non body-conforming mesh for the topology optimization method fails to capture the sharp change in velocity gradient with a high Reynolds number flow. These oscillations are not problematic at the system analysis level, but prevent the design from converging to an optimized shape at the design optimization level, creating element-scale cavities near the solid boundaries. Several stabilization methods are examined for their ability to alleviate

the instabilities. The Galerkin/least-square method produces less oscillation in most cases but it is insufficient in resolving the convergence issue. The density and sensitivity filters do not effectively suppress the cavities at the design optimization level, while a move-limit scheme easily prevents this instability without significant increase in computational cost.

The topology optimization method is applied to the convective cooling system design, by using the same configuration that was successfully used in designing the Navier-Stokes flow system. The main design purpose is to design a flow channel to maximize cooling efficiency. A numerical issue concerning the behavior of the Brinkman penalization is presented with example designs. The optimizer frequently ignores the Brinkman penalization and creates infeasible designs. To resolve this issue, a multi-objective function that also minimizes pressure drop is suggested. As design examples, 2D and 3D cooling channels are designed by the multi-objective function, and the effect of Reynolds and Prandtl number change is discussed.

CHAPTER 1

INTRODUCTION

1.1. Motivation and goal

Design of an improved cooing system has become a more critical task for developing new products. In the automotive industry, next-generation engines, motors, generators and converters are designed more compactly for reducing mass, minimizing required space, reducing frictional loss and increasing fuel efficiency. Electric circuits also become denser and faster and multiprocessor computer system chips are clustered in closer proximity. This compactness makes power density of equipment higher and causes thermal load to constantly increase. As a consequence, the ability to efficiently remove heat from an increasingly restricted space is currently a very critical issue. The need to develop optimization methodologies in order to design efficient cooling systems is drawing the attention of a large number of industrial and university researchers.

Sizing, shape and topology optimization methods have great potential to advance cooling structure design. The rapid growth of computational power and CAE software makes it possible to model complex geometries and accurately take into account physical

processes and material behavior with reasonable computational efforts. Still, the developing procedure of cooling structure depends on the traditional trial-and-error method, which is very time consuming and requires enormous experimental data. Moreover, the trial and error method may become problematic because the outcome depends mainly on the expertise of the designer, and there is no guarantee of design improvement during the design process. Hence, there is a need to develop automated and computerized design optimization approaches, such as sizing, shape and topology optimization, which automatically determine a design change and furthermore guarantee the improvement of the structure design. These automated optimization processes speed up the design process and reduce development cost.

In this work, design optimization of convective cooling systems is carried out using the topology optimization approach. Of the automated optimization methods, topology optimization was most recently introduced by Bensøe and Kikuchi [1], and it has been successfully applied to structural design optimization problems. The main advantages of topology optimization are first, that it allows change of the structural topology during the optimization process and, second, that the final design barely depends on the initial design. Since the structural topology determines the configuration of cooling channels, the choice of appropriate structural topology is usually the most decisive factor influencing the efficiency of a new design. However, by using the size and shape optimization methods, it is challenging to change the roughly guessed structural topology in the conceptual stage of the optimization process. Therefore, the topology optimization method is a very valuable tool, particularly in the beginning stages, in that it can optimize the structural topology.

This new optimization approach has been applied to various physics problems such as electromagnetics, heat conduction, and fluidics. Yet, the topology optimization approach for heat convection problems is still in the initial stage, and has not been well established. Previous topology optimization problems for heat transfer problems focused mainly on heat conduction, although the heat convection coefficient 'h' is sometimes applied. In this study, fluid analysis is also carried out for topology optimization to produce better optimization results focusing on the behavior of coolant flow. For this purpose, this study first extends the study of topology optimization in two steps. First, it applies the topology optimization method of linear Stokes flow systems for designing nonlinear Navier-Stokes flow systems. Then, it combines the results with previous topology optimization studies of heat transfer problems.

Since topology optimization generally requires high computational cost, it is essential to establish a cost-effective procedure for system analysis and design optimization. This study presents the adjoint sensitivity method for nonlinear, weakly-coupled multiphysics systems and introduces stabilized finite element methods to reduce the computational cost without serious loss of accuracy. The stabilization method is also essential to simulate convective-dominant problems such as high Reynolds flow problems. Finally, this dissertation discusses numerical issues that arise when the previous topology optimization approach is applied to nonlinear and multiphysics systems.

In the introduction, the literature on cooling system design is summarized. In addition, the literature on the topology optimization and stabilized finite element methods are described. Then, the outline of this dissertation is presented.

1.2. Cooling system design optimization

Cooling system design is an important element in many industrial applications, such as cooling flows in combustion engines, electric motors and battery packs. In automotive industries, battery thermal management is critical in achieving performance and in extending the life of batteries in electric and hybrid vehicles under real driving conditions [2]. Many studies have sought to develop accurate finite element models to predict the temperature distribution in battery cells and to improve thermal performance [3-4]. In any engine part, the cooling system must remove enough heat to allow proper engine function and evenly distribute the heat, primarily throughout the water jacket. Improper design of the cooling flow path can result in significant overheating of engine parts, which limits performance and durability, and causes structural damage. On the other hand, an optimized engine cooling system leads to improved durability and lower fuel consumption [5]. For this reason, optimization methodologies for better engine coolant flow [6-7] and engine gasket hole designs [5, 8-9] have been developed.

Also, the growth in power electronics technologies has produced smaller devices with increased levels of current and voltage. As the power density of these devices becomes greater, thermal loss is increased, which leads to an increase in component failure and a decrease in reliability. Therefore, designers attempt to improve thermal management through innovation of cooling system design. First, thermal analysis was performed, providing guidelines for designing cooling channels and heat sinks for motors and converters [10-11]. Khorunzhii *et al*. [12] investigated the micro cooling design of a pin-fin heat converter for a power semiconductor.

Then, the above-mentioned optimization processes are all performed by manually and intuitively modifying design parameters. However, this process does not guarantee design improvement during the design process. To achieve design automation, many algorithms for numerical optimization technologies have been proposed such as size optimization, parametric shape optimization, shape optimization and topology optimization. The main advantage of these methods is that a design change will be determined automatically and the improvement of the structure is mathematically guaranteed.

For example, size optimization processes were used for pin-fin heat sink designs [13-15] to determine the best uniform fin heights, non-uniform fin heights and non-uniform fin gaps respectively. Figure 1.2.1 shows the optimized results of heat sink design using size optimization. Also, a parametric shape optimization technique was used to design a better cooling system. Lee *et al*. [16] selected geometric parameters to define overall design structure such as channel width, length, height, pin pitch and angles (see Figure 1.2.2) and found the best values for these parameters. Similarly, this technique is used in designing heat sink shape [17-19] and dimple shape in the cooling channel for laminar flow and turbulent flow, in [20-21] respectively. Also, Kuhl *et al*. presented optimization processes for designing cooling channels in the combustion chamber of a rocket engine [22].

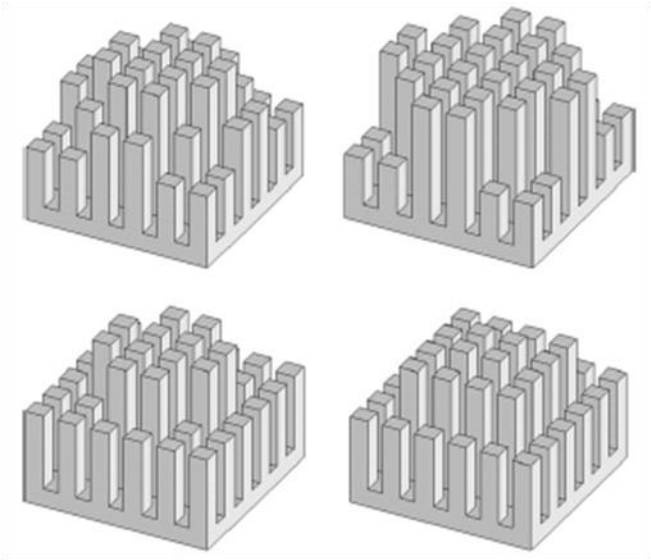

Figure 1.2.1. Schematic diagram of different heights design results for pin-fin heat sink [14]

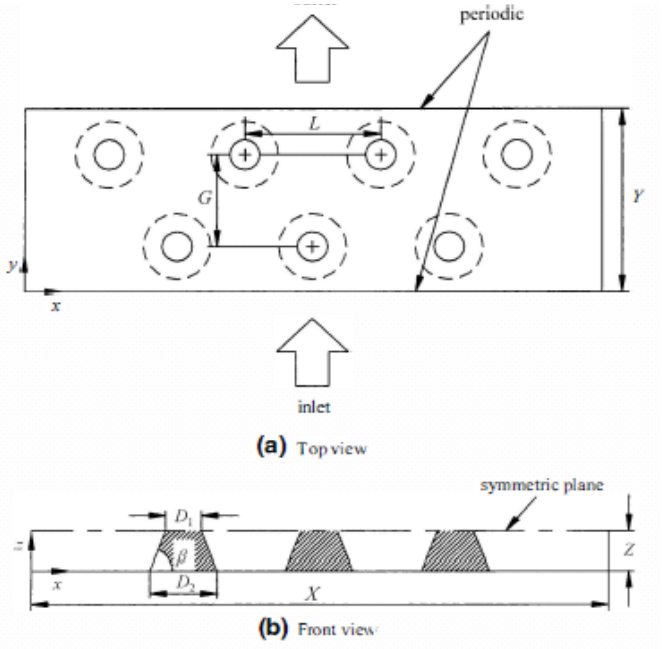

Geometric parameter
X (width of the channel)
Y (length of the channel)
Z (height of the channel)
L (pin spacing)
G (pin pitch)
β (pin angle)
D_1 (pin diameter at the symmetric plane)
D_2 (pin diameter at the bottom)

Figure 1.2.2. Schematic diagram of design variables in parametric shape optimization [16]

While parametric shape optimization uses geometric parameters, shape optimization uses geometrical information of boundary mesh. To optimize structure, shape optimization searches for the best location of boundary by shape variations of the mesh morphing. Balagangadhar *et al*. [23] shows the sensitivity calculation for thermal fluid shape optimization. Two dimensional oval tubes in the heat exchangers are optimized for maximizing heat transfer [24-25] and three dimensional corrugated wall cooling channel [26]. Airfoil-type heat exchangers are designed [27-28] as shown in Figure 1.2.3. Recently, Non-Uniform, Rational, B-spline (NURB) is widely used for shape optimization which enables easy control of boundary geometry. NURB is used to design heat sink [29-30] and internally finned cooling pipe [31-33].

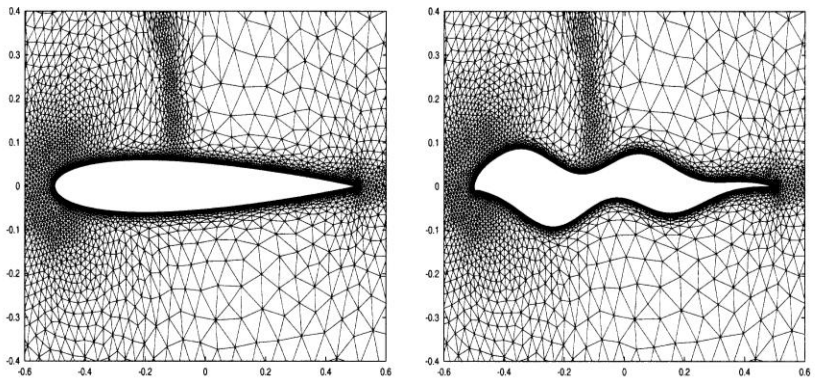

Figure 1.2.3. Shape deformation by shape optimization process (left: initial, right: deformed) [34]

However, size and shape optimization have a limitation when they handle complicated geometry and topology such as engine cooling jacket. For example, shape and location of holes sometimes play a vital role in cooling system as shown in engine gasket design [5-9]. It is impractical to use size and shape optimization for designing new holes by

changing structural topology. For this reason, topology optimization has a significant potential and can play a vital role.

1.3. Topology optimization of thermal-fluid cooling system

The goal of topology optimization is to determine the optimal distribution of materials for minimizing design objectives. The material phases are indicated by 0-1 local design variables, for example φ=1 indicates a solid phase and φ=0 indicates a void phase. By optimizing the variables, the structural topology (i.e., the structural connectivity of inside holes) evolves. Since topology optimization was initiated by Bensøe and Kikuchi [1], it has been successfully adopted to the structural optimization of solid mechanics problems, such as minimum compliance designs, compliant mechanism designs and microstructures (see [35] and references therein for the application of the topology optimization technique). Since the numerical instabilities are revealed within the design framework of topology optimization, many studies have been conducted to explain and suppress instabilities such as checkerboard patterns, mesh dependency and local minima [36-38].

Along with the successful introduction of the topology optimization method to solid mechanics problems, topology optimization problems for fluid systems were initiated by the work of Borrvall and Petersson [39]. They added the Darcy friction force term $-\alpha u$, which is the multiplication of the Darcy friction coefficient and velocity [40], to the original fluid equation such as Stokes equation. Then, they represent the structural topology by the distribution of two-phase material having different material properties: solids ($\alpha_s \approx \infty$) and fluids ($\alpha_f = 0$), where α is the Darcy friction coefficient. Since the

Darcy friction coefficient has infinite value in the solid region, the velocity in the solid region converges to zero, satisfying no-slip boundary conditions. On the other hand, the added Darcy friction term becomes zero in the fluid region Ω_f, and the original fluid equation is recovered. It should be noted that this analysis method is a fictitious domain approach with Brinkman penalization based on porous media theory, and the mathematical justification is achieved in [41-44]. To combine this analysis approach with the conventional topology optimization technique, the Darcy friction coefficient (the Brinkman penalization parameter) α is interpolated as a function of local design variables φ. With this interpolation, φ=0 indicates a fluid region (i.e., $\alpha(0)=0$) and φ=1 indicates a solid region (i.e., $\alpha(1) \approx \infty$) so that the design problem become a typical 0-1 topology optimization problem.

Following this idea, numerous studies have been performed. Wiker *et al*. added effective viscosity variation as an additional property control of two-phase material [45-46]. Gersborg-Hansen *et al.* suggested a topology optimization method for Navier-Stokes flow [47], which is similar to the Borrvall and Petersson's work [39]. Various example problems followed such as Stokes flow [48], microfluidics [49-50], 3D Stokes flow [51], mixing [52-53], reactor design [54] and fluid-structure interaction problem [55]. In addition, Pingen *et al*. presented topology optimization for nano-fluid problem by using Lattice Boltzmann equation [56-57] and Duan *et al*. demonstrated topology optimization for Stokes' flow and Navier-Stokes' flow via variational level set method [58-60]. In industrial applications, Daimler-Chrysler and Volkswagen engineers demonstrated the possibility of topology optimization for air channel flow design [61-62].

Besides the successful utilization of topology optimization for fluid systems, heat transfer problems have also been an issue of great concern as applications of the topology optimization method. Topology optimization is first applied to pure heat conduction problems [63-67]. In addition to heat conduction, heat convection physics is also taken into consideration by employing convection the coefficient '*h*' in [68-72]. In conventional topology optimization methods, it is not easy to clearly define boundary locations in the middle of the process, since they are blurry and constantly changing. Therefore, previous research assumed that the heat convection coefficient was constant without considering fluid motion, which varies significantly according to the geometry. Subsequently, these approaches may be infeasible for designing cooling channels that prevent re-circulation areas and hot spots.

To overcome this issue, Iga *et al*. [73] recently applied the design-dependent topology optimization method developed by Chen and Kikuchi [74]. They approximated design dependent heat convection coefficient by using the flow simulation of a simplified periodic fin model. Yet, the possibility of practical implementation of their assumption is an open question. Therefore, this study performs flow motion analysis without using such simplified model so as to figure out accurate heat transfer condition at the fluid-solid interfaces. Successful integration of CFD analysis into the topology optimization method of heat transfer problems might be a good solution, which has significant potential for the future design of complex cooling system.

1.4. Stabilized finite element method

Stabilized finite element methods are now commonly used in finite element computation of flow problems due to the computational difficulties and shortcomings of the Galerkin finite element method (GFEM) [75-76]. The main issue for the standard GFEM is the occurrence of velocity wiggles in flow problems. This numerical instability is a node-to-node oscillation, producing a large velocity gradient caused by the inability of GFEM to capture the steep gradient. It results in an imbalance between the convective and diffusive terms in the equation. Stabilized finite element methods bring numerical stability to flow problems with high Reynolds numbers and coarse meshes, without introducing excessive numerical dissipation. They also bring numerical stability to incompressible flow computation when using equal-order interpolation functions for velocity and pressure, which significantly reduce the computational cost.

Some of the earliest stabilized formulations are the streamline-upwind/Petrov–Galerkin (SUPG) formulation [77-78] and the pressure-stabilizing/Petrov–Galerkin (PSPG) formulation [79-80]. The SUPG method addresses the wiggle problem by introducing the concept of adding diffusion along the streamlines. The PSPG method allows us to use equal-order interpolation functions for velocity and pressure, without considering the LBB stability condition. Another method for enhancing the stability of the GFEM for incompressible flow is the Galerkin/Least-squares (GLS) approach, which involves the addition of various least-squares terms to the original Galerkin variational statement. Development and popularization of the GLS methods for flow problems [79, 81-84] follows as a generalization of SUPG and PSPG methods. The underlying

philosophy of the SUPG and GLS methods is to strengthen the classical variational formulations so that the discrete approximations, which would otherwise be unstable, become stable and convergent.

The sub-grid scale (SGS) stabilization method originated from the concept of representing multiscale phenomenon, which delivers similar results to the SUPG and GLS techniques unless the reaction term is dominant. Also, the variational multiscale method (VMS) was introduced by Hughes [85], providing the necessary mathematical framework for the SGS models. In this method, the different stabilization techniques come together as special cases of the underlying sub-grid scale concept. It should be noted that some of the stabilized methods discussed above were somewhat ad hoc in nature [75-76]. However, the introduction and development of the VMS method has remedied much of the confusion regarding stabilized procedures and provided much needed explanation and consistency in implementation. Masud and co-workers developed VMS formulations for the Darcy-Stokes flow equations [86-87], the advection–diffusion equation [88], the convection-diffusion-reaction equations [89] and the incompressible Navier–Stokes equations [90].

In these stabilization methods, an embedded stabilization tensor most commonly known as $\boldsymbol{\tau}$ plays an important role. The definitions of the stabilization tensors have been extensively studied and developed for the SUPG, PSPG and GLS stabilization methods [77, 84, 91-96] as well as for the SGS stabilization method [97-98]. The stabilization tensors are expressed in terms of the ratios of the norms of the matrices or vectors, taking into account local length scales, the advection field and the element Reynolds number.

1.5. Outline of dissertation

The remainder of this dissertation is organized as follows:

Chapter 2 presents an analysis method for topology optimization of thermal-fluid systems. Numerical issues in system analysis are described. Chapter 3 presents the topology optimization of Navier-Stokes flow systems and investigated numerical instabilities of the topology optimization of these nonlinear systems. Chapter 4 presents the topology optimization of thermal-fluid systems. After numerical issues concerning these multiphysics problems are investigated, 2D and 3D convective cooling systems are designed. Chapter 5 concludes the dissertation with remarks and future works. Appendices include the detailed derivations of the multi-scale stabilization tensors.

CHAPTER 2

THERMAL-FLUID ANALYSIS FOR TOPOLOGY OPTIMIZATION

2.1. Introduction

This chapter presents an analysis method for topology optimization of thermal-fluid systems. A fictitious domain approach [42-44, 99], with immersed boundaries and Brinkman penalization, which is based on the porous fluid theory, has been mainly used for the topology optimization of linear Stokes flow systems [45-46, 51, 100-102]. This study extends the analysis approach to topology optimization of nonlinear Navier-Stokes flow systems and further multiphysics thermal-fluid systems.

To establish a stable and cost-effective method, various stabilized finite element methods, such as SUPG, PSPG, GLS, SGS and VMS, are tested and compared with different stabilization tensors. The obtained solutions of the Brinkman-Penalized Navier-Stokes equation, which is based on the fictitious domain approach [42-44, 99], are confirmed whether or not the no-slip boundary condition at the immersed solid boundaries and the zero-velocity condition in the solid regions are satisfied. Numerical

issues concerning the value of the Brinkman penalization parameter are studied, and numerical instability at the immersed boundaries is investigated.

The outline of Chapter 2 is as follows: Section 2.2 introduces a system analysis method for thermal-fluid systems; Brinkman-penalized Navier-Stokes equation and homogenized thermal transport equation are explained. Section 2.3 presents different stabilized finite element methods and stabilization tensors. Section 2.4 explains in detail how to implement the Newton-Raphson methods. Section 2.5 discusses numerical issues arise from the solutions of Brinkman-penalized Navier-Stokes equation. Section 2.6 summaries this section.

2.2. Governing equations for topology optimization

During the topology optimization process for convective cooling systems, design domains consists of fluid, solid and porous regions, as shown in Figure 2.2.1. To simulate fluid flows around porous and solid obstacles having complex geometries, various immersed boundary methods can be used. The main advantage of using immersed boundary methods is efficient implementation of fixed non-body conformal Cartesian grids for representing complex stationary or moving solid boundaries. The shapes of solid structures are continuously changed during the topology optimization process. Therefore, it is more efficient to use the same fixed Cartesian grid than body-conformal grids that usually needs to be re-generated at each optimization step.

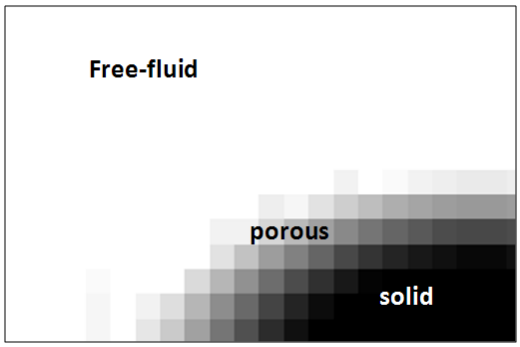

Figure 2.2.1. Fluid-solid system in topology optimization for fluid systems

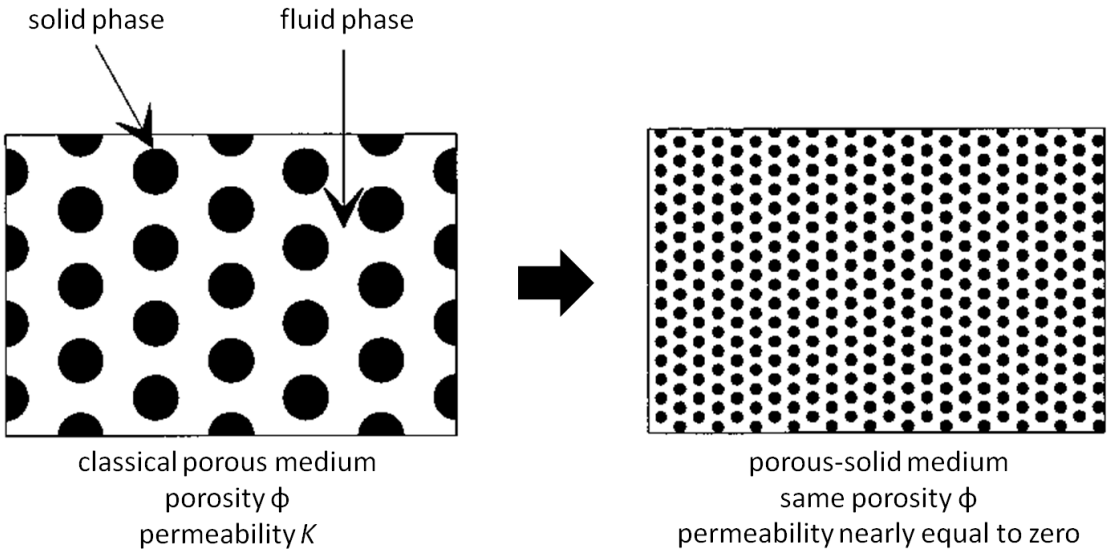

Figure 2.2.2. Representation of the solid region as a porous medium [42]

2.2.1. Brinkman-penalized Navier-Stokes equation

Among immersed boundary methods, the Brinkman penalization method [42-44, 99], which is proposed for solving incompressible viscous flow by penalizing the momentum equation, is widely used for the topology optimization of Stokes flow systems. The main idea of this method is to model solid obstacles as porous media with porosity near unity, but permeability approaching zero as shown in Figure 2.2.2.

A steady-state incompressible fluid is governed by the Navier-Stokes equation with the Boussinesq approximation as:

$$\rho_f \boldsymbol{v} \cdot \nabla \boldsymbol{v} - \mu_f \nabla^2 \boldsymbol{v} + \nabla p = \boldsymbol{f} \tag{2.2.1}$$

$$\nabla \cdot \boldsymbol{v} = 0 . \tag{2.2.2}$$

Here, ρ_f is fluid density, μ_f fluid dynamic viscosity, $\boldsymbol{v}$ fluid velocity, p pressure and $\boldsymbol{f}$ is body force. I assume incompressible flow, and gravitational acceleration and buoyancy force are not taken into consideration from a practical standpoint.

Then, the effect of the no-slip boundary condition is implemented by adding the Brinkman penalization term $\alpha \boldsymbol{v}$, which is physically interpreted as the Darcy-friction force, to the Navier-Stokes equation as

$$\rho_f \boldsymbol{v} \cdot \nabla \boldsymbol{v} - \mu_f \nabla^2 \boldsymbol{v} + \alpha \boldsymbol{v} + \nabla p = \boldsymbol{f} \tag{2.2.3}$$

where α is the Brinkman penalization parameter which varies spatially in the design domains, as shown in the following Table 2.2.1, so as to distinguish the physics between free-fluid and solid regions.

Table 2.2.1 The value of the Brinkman penalization parameter

	Fluid region	**Solid region**
Brinkman penalization parameter	$\alpha = \alpha_f \approx 0$	$\alpha = \alpha_s \approx \infty$

In the fluid region, the Brinkman penalization term $\alpha \boldsymbol{v}$ tends toward zero and is negligible compared to the other terms of the equation (2.2.3). Consequently, the classical Navier-Stokes equation (2.2.1) is recovered. However, in the solid region, the Brinkman penalization term has sufficiently large value, which causes the velocity to tend toward zero. Thus, the convection term becomes negligible, and the classical Brinkman equation (2.2.4) is solved.

$$-\mu_f \nabla^2 \boldsymbol{v} + \alpha_s \boldsymbol{v} + \nabla p = \boldsymbol{f} \ . \tag{2.2.4}$$

Finally, if α_s is sufficiently large and there is no body force f inside the solid region, all terms except the Brinkman penalization term are numerically ignored and the equation (2.2.4) becomes as

$$\alpha_s \boldsymbol{v} = 0\,, \tag{2.2.5}$$

which forces the velocity to converge to zero.

Since the velocity converges to zero in the solid region, the no-slip boundary condition at the solid surface is automatically satisfied, and there is no need to explicitly specify the fluid-solid interface condition. Likewise, the fluid velocity inside solid structures converges to zero, thus physically correct flow motions near solid obstacles are obtained. Mathematical justification of this method, based on the L^2-penalized equation, is derived in [43-44].

I set the value of α_f to zero without any numerical difficulties, but the value of penalty parameter α_s should be carefully assigned. The error estimate of the velocity field in the H^1-norm over the whole domain is the order of $\mathcal{O}\left(\alpha_f + \alpha_s^{-1/4}\right)$, whereas the L^2-norm of the velocity error inside the solid body is $\mathcal{O}\left(\alpha_s^{-3/4}\right)$. In theory, the higher α_s is set, the smaller the mathematical error is. However, in practice, using too large α_s decreases both the convergence speed and accuracy of Newton-Raphson iteration method when solving the nonlinear equation. Thus, the value of penalty parameter α_s should be carefully pre-assigned to reduce both theoretical errors and numerical errors, which will be presented in section 2.5.1.

2.2.2. Homogenized thermal transport equation

The traditional thermal transport equation is expressed as

$$\rho_f C_p \boldsymbol{v} \cdot \nabla T - \nabla \cdot \left(k \nabla T \right) = 0 . \tag{2.2.6}$$

where T is temperature, C_p constant-pressure specific heat and k is thermal conductivity. The viscous dissipation term is ignored compared to other terms from a practical standpoint [103-105]. In this work, the thermal conductivity varies in the two different regions as shown in Table 2.2.2.

Table 2.2.2 The value of the thermal conductivity

	Fluid region	**Solid region**
Thermal conductivity	$k = k_{\mathrm{f}}$	$k = k_{\mathrm{s}}$

In the solid region, the fluid velocity $\boldsymbol{v}$ becomes zero due to the Brinkman penalization, so that the thermal transport equation (2.2.6) becomes a pure conduction equation without the leftmost convective term as

$$-\nabla \cdot \left(k_s \nabla T \right) = 0 . \tag{2.2.7}$$

In the fluid region, the energy equation (2.2.6) maintains the original form with the thermal conductivity of fluid as

$$\rho_f C_p \boldsymbol{v} \cdot \nabla T - \nabla \cdot \left(k_f \nabla T \right) = 0 \tag{2.2.8}$$

These governing equations, for fluid physics (2.2.3) and heat transfer physics (2.2.6), are weakly coupled only through fluid velocity because all material properties are assumed to be independent from temperature and buoyancy force is ignored from a practical standpoint. Therefore, the momentum equation (2.2.3) and the incompressibility constraint (2.2.2) can first be solved together without considering temperature profile. Then the temperature profile is obtained by solving the energy equation (2.2.6). This two-step analysis strategy after decoupling temperature significantly decreases computational cost.

2.2.3. Slightly compressible fluid condition

Instead of the incompressible constraint (2.2.2), Anton Evgrafov suggested solving a slightly compressible fluid model so as to deal with impenetrable inner walls that may appear in the flow domain and to obtain a closed design-to-flow mapping [106]. This slightly compressible condition is implemented with a penalization in the continuity equation as

$$\nabla \cdot \boldsymbol{v} = -\frac{1}{\lambda} p \,. \tag{2.2.9}$$

where λ is a penalty parameter, which ensures the continuity equation when it has a sufficiently large value. In theory, this is a mathematically good approach. However, in

practice, there exist numerical difficulties in applying this slightly compressible condition for the topology optimization of Navier-Stokes flow systems.

First of all, too large of a value for λ decreases the effect of the Brinkman penalization inside solid regions preventing the velocity inside solid regions from converging to zero, whereas too small of a value for λ produces an inaccurate solution in the fluid analysis. By implementing the equation (2.2.9), the momentum equation including the Brinkman penalization term will become as

$$\rho_f \boldsymbol{v} \cdot \nabla \boldsymbol{v} - \mu_f \nabla \boldsymbol{\varepsilon}(\boldsymbol{v}) - \lambda \nabla (\nabla \cdot \boldsymbol{v}) + \alpha \boldsymbol{v} = \boldsymbol{f} \tag{2.2.10}$$

where $\boldsymbol{\varepsilon}(\boldsymbol{v}) = \nabla \boldsymbol{v} + (\nabla \boldsymbol{v})^T$. Since this momentum equation has two penalization terms $-\lambda \nabla (\nabla \cdot \boldsymbol{v})$ and $\alpha_S \boldsymbol{v}$ inside the solid region, the two values of λ and α_s should be carefully selected in order to make both penalizations function properly. For example, if the two values are very similar to each other, the momentum equation in the solid region will become as

$$-\lambda \nabla (\nabla \cdot \boldsymbol{v}) + \alpha_S \boldsymbol{v} = 0 . \tag{2.2.11}$$

This equation does not guarantee the zero velocity condition in the solid region. To satisfy both the slightly compressible and zero-velocity conditions, the value of α_s should be significantly larger than the value of λ to achieve both penalizations because the Brinkman penalization ($\boldsymbol{v}$ = 0) automatically satisfies the incompressible constraint.

Computational experience indicates that, although these values are dependent on problems, the value of α_s should be greater than $10^6 \times \lambda$ in some Navier-Stokes flow problems. Then, according to [75, 107-108], values of λ between 10^7 and 10^9 are adequate in most practical situations with double precision 64-bit words, which means α_s should be greater than 10^{13}. This too large value is hardly appropriate. It impairs both the convergence speed and accuracy of the Newton-Raphson iteration.

Instead of solving equation (2.2.10), another modified penalty formulation can be obtained by applying the assumption of a slightly compressible barotropic fluid. The modified penalty formulation is expressed as an iterative algorithm as follows:

$$\begin{bmatrix} \mathbf{A} & \mathbf{Q} \\ \mathbf{Q}^T & -\frac{1}{\lambda}\mathbf{I} \end{bmatrix} \begin{bmatrix} \mathbf{u}^{n+1} \\ \mathbf{p}^{n+1} \end{bmatrix} = \begin{bmatrix} \mathbf{F} \\ -\frac{1}{\lambda}\mathbf{p}^n \end{bmatrix}. \tag{2.2.12}$$

Here, **Au** is the summation of viscous, convective and Brinkman penalization terms, **F** the body force, and **Qp** and $\mathbf{Q}^T\mathbf{u}$ are the pressure gradient and divergence of the velocity field, respectively. Then, the second set of equations takes the form

$$\mathbf{p}^{n+1} = \mathbf{p}^n - \lambda \mathbf{Q}^T \mathbf{u}^{n+1}. \tag{2.2.13}$$

This modified formulation is equivalent to the introduction of a false transient in the steady-state calculation. Furthermore, it allows to use smaller penalty parameters, while satisfying the incompressibility constraint practically to the round-off error limit [107]. Therefore, using this modified penalty formulation with small λ might resolve the

numerical issues concerning too large of a value for α_s. However, this research focus on a nonlinear system, so adding this iterative algorithm to the Newton-Raphson iteration will significantly increase the computational cost. In conclusion, more studies are needed to properly applying both the slightly compressible condition and the Brinkman penalization to highly nonlinear Navier-Stokes flow analyses, and this research therefore limits itself to incompressible fluids.

2.3. Stabilized finite element method

Stabilized finite element methods are used to solve the weakly coupled governing equations (2.2.3) and (2.2.6). Stabilized finite element methods are now commonly used in finite element analysis of flow-concerned problems. They bring numerical stability to high Reynolds number flow problems without creating excessive numerical dissipation. They also bring numerical stability to incompressible flow computations when using equal-order interpolation functions for velocity and pressure [75-76, 80, 109]. The equal-order linear interpolation significantly reduces computational cost, thus it is very practical for the topology optimization that generally requires high computational power. Moreover, the equal-order linear interpolation leads to the convenient implementation of the analysis, and accordingly makes it simple to derive the design sensitivity.

The nonlinear Brinkman-penalized Navier-Stokes equation and the homogenized thermal transport equation can be assumed as a convection-diffusion-reaction equation with or without a zero reaction term. Therefore, we can define the two governing equations as

$$L(\phi) = \boldsymbol{f} \,. \tag{2.3.1}$$

where $\boldsymbol{f}$ is the body source vector, ϕ system response and L is a differential operator of the convection-diffusion-reaction (CDR) equation such as

$$L(\phi) = \boldsymbol{v} \cdot \nabla\phi - k\nabla^2\phi + s\phi \,. \tag{2.3.2}$$

where $\boldsymbol{v}$ is the advection velocity, k the diffusivity and s is the reaction coefficient. The reaction coefficient s for the thermal transport equation is zero. Then, the advective operator and the adjoint operator can be expressed as

$$L_{adv}(\phi) = \boldsymbol{v} \cdot \nabla\phi \tag{2.3.3}$$

$$L^*(\phi) = -\boldsymbol{v} \cdot \nabla\phi - k\nabla^2\phi + s\phi \,. \tag{2.3.4}$$

Consider the analysis space divided by N number of elements over the domain Ω. Then, the discrete solution of equation (2.3.1) can be obtained by solving the stabilized weak form for finite element analysis, which can be stated as: Find $\phi \in \mathcal{P}$, such that for all $w \in \mathcal{V}$,

$$\langle w, \boldsymbol{v} \cdot \nabla\phi \rangle_\Omega + \langle \nabla w, k\nabla\phi \rangle_\Omega + \langle w, s\phi \rangle_\Omega + \langle \tilde{L}w, \tau L\phi \rangle_{\tilde{\Omega}} = \langle w, f \rangle_\Omega + \langle w, t \rangle_{\Gamma_N} \tag{2.3.5}$$

where $\langle \cdot, \cdot \rangle_{\Omega} = \int_{\Omega} (\cdot) d\Omega$ is the inner product in L^2, w an weighting function, $\tilde{L}$ a stabilization operator applied to the variation in the stabilization term, Ω the spatial analysis domain, Γ_N the Neumann boundaries of the domain Ω and $\tilde{\Omega}$ is the sum of element interiors, i.e., $\tilde{\Omega} = \sum_{i=1}^{N} \Omega^e$. $\mathcal{V}$ and $\mathcal{P}$ are the standard variational functional spaces. For the detailed procedure, the reader is referred to [89].

2.3.1. Different stabilized finite element methods

The stabilized finite element methods can be categorized as the streamline-upwind Petrov-Galerkin (SUPG), the pressure-stabilizing Petrov-Galerkin (PSPG) the Galerkin/least-squares (GLS), the sub-grid scale (SGS) and the variational multi-scale (VMS) stabilization method by the choice of stabilization operator $\tilde{L}$ as shown in Table 2.3.1.

Table 2.3.1 Stabilization operators

Stabilization method	**SUPG+PSPG**	**GLS**	**SGS, VMS**
Stabilization operator $\tilde{L}$	$L_{adv}(\boldsymbol{w}) + \frac{1}{\rho_f} \nabla q$	$L(\boldsymbol{w})$	$-L^*(\boldsymbol{w})$
	$\boldsymbol{v} \cdot \nabla \boldsymbol{w} + \frac{1}{\rho_f} \nabla q$	$\boldsymbol{v} \cdot \nabla \boldsymbol{w} - k \nabla^2 \boldsymbol{w} + s \boldsymbol{w}$	$\boldsymbol{v} \cdot \nabla \boldsymbol{w} + k \nabla^2 \boldsymbol{w} - s \boldsymbol{w}$

Applying the described stabilization methods to the governing equation (2.2.3), the three types of the stabilized weak forms can be derived as follows:

SUPG+PSPG:
$$\left\{\begin{array}{c}\left\langle \boldsymbol{w},\left(\rho_f \boldsymbol{v}\cdot\nabla\boldsymbol{v}+\alpha\boldsymbol{v}\right)\right\rangle_\Omega+\left\langle\nabla\boldsymbol{w},\mu_f\nabla\boldsymbol{v}\right\rangle_\Omega-\left\langle\nabla\cdot\boldsymbol{w},p\right\rangle_\Omega \\ +\left\langle q,\nabla\cdot\boldsymbol{v}\right\rangle_\Omega+\left\langle\left(\rho_f\boldsymbol{v}\cdot\nabla\boldsymbol{w}+\nabla q\right),\boldsymbol{\tau}_U\boldsymbol{R}_U\right\rangle_{\tilde{\Omega}}\end{array}\right\}=\left\langle \boldsymbol{w},\boldsymbol{f}\right\rangle_\Omega+\left\langle \boldsymbol{w},\boldsymbol{t}\right\rangle_{\Gamma_N}$$

(2.3.6)

GLS:
$$\left\{\begin{array}{l}\left\langle \boldsymbol{w},\left(\rho_f \boldsymbol{v}\cdot\nabla\boldsymbol{v}+\alpha\boldsymbol{v}\right)\right\rangle_\Omega+\left\langle\nabla\boldsymbol{w},\mu_f\nabla\boldsymbol{v}\right\rangle_\Omega-\left\langle\nabla\cdot\boldsymbol{w},p\right\rangle_\Omega+ \\ \left\langle q,\nabla\cdot\boldsymbol{v}\right\rangle_\Omega+\left\langle\left(\rho_f\boldsymbol{v}\cdot\nabla\boldsymbol{w}-\mu_f\Delta\boldsymbol{w}+\alpha\boldsymbol{w}+\nabla q\right),\boldsymbol{\tau}_U\boldsymbol{R}_U\right\rangle_{\tilde{\Omega}}\end{array}\right\}=\left\langle \boldsymbol{w},\boldsymbol{f}\right\rangle_\Omega+\left\langle \boldsymbol{w},\boldsymbol{t}\right\rangle_{\Gamma_N}$$

(2.3.7)

SGS, VMS:
$$\left\{\begin{array}{l}\left\langle \boldsymbol{w},\left(\rho_f \boldsymbol{v}\cdot\nabla\boldsymbol{v}+\alpha\boldsymbol{v}\right)\right\rangle_\Omega+\left\langle\nabla\boldsymbol{w},\mu_f\nabla\boldsymbol{v}\right\rangle_\Omega-\left\langle\nabla\cdot\boldsymbol{w},p\right\rangle_\Omega+ \\ \left\langle q,\nabla\cdot\boldsymbol{v}\right\rangle_\Omega+\left\langle\left(\rho_f\boldsymbol{v}\cdot\nabla\boldsymbol{w}+\mu_f\Delta\boldsymbol{w}-\alpha\boldsymbol{w}+\nabla q\right),\boldsymbol{\tau}_U\boldsymbol{R}_U\right\rangle_{\tilde{\Omega}}\end{array}\right\}=\left\langle \boldsymbol{w},\boldsymbol{f}\right\rangle_\Omega+\left\langle \boldsymbol{w},\boldsymbol{t}\right\rangle_{\Gamma_N}$$

(2.3.8)

where $\boldsymbol{w}$ is the variation vector for velocity, q the variation for pressure, and $\boldsymbol{\tau}_U$ the stabilization tensor. $\boldsymbol{R}_U$ is the residual of the momentum equation, given by

$$\boldsymbol{R}_U=\rho_f\boldsymbol{v}\cdot\nabla\boldsymbol{v}-\mu_f\nabla^2\boldsymbol{v}+\alpha\boldsymbol{v}+\nabla p-\boldsymbol{f}\ . \tag{2.3.9}$$

For high Reynolds number flow, the least-square on incompressibility constraint (LSIC) stabilization scheme can additionally applied by adding the following equation (2.3.10) to the weak-form equations (2.3.6) ~(2.3.8).

$$\left\langle\nabla\cdot\boldsymbol{w},\boldsymbol{\tau}_{LSIC}\nabla\cdot\boldsymbol{v}\right\rangle=0 \tag{2.3.10}$$

where $\boldsymbol{\tau}_{LSIC}$ is a LSIC stabilization tensor.

Likewise, by applying the stabilization methods to the thermal transport equation (2.2.6), the stabilized weak form becomes as follows:

SUPG: $$\left\langle w, \rho_f C_p \boldsymbol{v}\cdot\nabla T\right\rangle_{\Omega} + \left\langle \nabla w, k\nabla T\right\rangle_{\Omega} + \left\langle \rho_f C_p \boldsymbol{v}\cdot\nabla T, \boldsymbol{\tau}_T \boldsymbol{R}_T\right\rangle_{\tilde{\Omega}} = \left\langle w, \boldsymbol{t}\right\rangle_{\Gamma_N} \tag{2.3.11}$$

GLS: $$\left\langle w, \rho_f C_p \boldsymbol{v}\cdot\nabla T\right\rangle_{\Omega} + \left\langle \nabla w, k\nabla T\right\rangle_{\Omega} + \left\langle \rho_f C_p \boldsymbol{v}\cdot\nabla T - k\Delta T, \boldsymbol{\tau}_T \boldsymbol{R}_T\right\rangle_{\tilde{\Omega}} = \left\langle w, \boldsymbol{t}\right\rangle_{\Gamma_N} \tag{2.3.12}$$

SGS, VMS: $$\left\langle w, \rho_f C_p \boldsymbol{v}\cdot\nabla T\right\rangle_{\Omega} + \left\langle \nabla w, k\nabla T\right\rangle_{\Omega} + \left\langle \rho_f C_p \boldsymbol{v}\cdot\nabla T + k\Delta T, \boldsymbol{\tau}_T \boldsymbol{R}_T\right\rangle_{\tilde{\Omega}} = \left\langle w, \boldsymbol{t}\right\rangle_{\Gamma_N} \tag{2.3.13}$$

where w is the variation for temperature, and $\boldsymbol{\tau}_T$ is the stabilization tensor $\boldsymbol{R}_T$ is the residual of the energy equation, given by

$$\boldsymbol{R}_T = \rho_f C_p \boldsymbol{v}\cdot\nabla T - \nabla\cdot\left(k\nabla T\right). \tag{2.3.14}$$

2.3.2. Stabilization tensors

Each stabilization method has a stabilization tensor, such as $\boldsymbol{\tau}_U$, $\boldsymbol{\tau}_{LSIC}$ and $\boldsymbol{\tau}_T$. Several schemes to determine the stabilization tensors are tested. For SUPG, PSPG and GLS stabilization methods, the stabilization tensors as suggested in [93, 95-96] are used as shown in Table 2.3.2. Here, $\boldsymbol{I}$ is an identity matrix, h the length of the finite element and N_a is the shape function associated with node number a. For SGS and LSIC stabilization methods, the schemes shown in Table 2.3.3 and Table 2.3.4 are used to calculate their stabilization tensor, respectively.

Table 2.3.2 Stabilization tensors for SUPG, PSPG and GLS stabilization method

	Stabilization tensor (SUPG/PSPG/GLS)
Shakib *et al.* [95]	$\boldsymbol{\tau}_U = \left\{ \left(\frac{h}{2\|\boldsymbol{v}\|} \right)^{-2} + \left(\frac{\rho}{\alpha} \right)^{-2} + 9\left(\frac{\rho h^2}{4\mu} \right)^{-2} \right\}^{\frac{-1}{2}} \boldsymbol{I}$ $\boldsymbol{\tau}_T = \left\{ \left(\frac{h}{2C_p\|\boldsymbol{v}\|} \right)^{-2} + 9\left(\frac{\rho h^2}{4k} \right)^{-2} \right\}^{\frac{-1}{2}} \boldsymbol{I}$
Tezduyar *el al*. [93]	$\boldsymbol{\tau}_U = \left\{ \left(\frac{h_{UGN}}{2\|\boldsymbol{v}\|} \right)^{-2} + \left(\frac{\rho}{\alpha} \right)^{-2} + \left(\frac{\rho h_{UGN}^2}{4\mu} \right)^{-2} \right\}^{\frac{-1}{2}} \boldsymbol{I}$ $\boldsymbol{\tau}_T = \left\{ \left(\frac{h_{UGN}}{2C_p\|\boldsymbol{v}\|} \right)^{-2} + \left(\frac{\rho h_{UGN}^2}{4k} \right)^{-2} \right\}^{\frac{-1}{2}} \boldsymbol{I}$ $h_{UGN} = 2\|\boldsymbol{v}\| \left(\sum_{a=1}^{n_{en}} \lvert \boldsymbol{v} \cdot \nabla N_a \rvert \right)^{-1}$
Tezduyar [96]	$\boldsymbol{\tau}_U = \left\{ \left(\frac{h_{RGN}}{2\|\boldsymbol{v}\|} \right)^{-2} + \left(\frac{\rho}{\alpha} \right)^{-2} + \left(\frac{\rho h_{RGN}^2}{4\mu} \right)^{-2} \right\}^{\frac{-1}{2}} \boldsymbol{I}$ $\boldsymbol{\tau}_T = \left\{ \left(\frac{h_{RGN}}{2C_p\|\boldsymbol{v}\|} \right)^{-2} + \left(\frac{\rho h_{RGN}^2}{4k} \right)^{-2} \right\}^{\frac{-1}{2}} \boldsymbol{I}$ $h_{RGN} = 2\left(\sum_{a=1}^{n_{en}} \lvert \boldsymbol{r} \cdot \nabla N_a \rvert \right)^{-1}$ $\boldsymbol{r} = \frac{\nabla\|\boldsymbol{v}\|}{\|\nabla\|\boldsymbol{v}\|\|}$

Table 2.3.3 Stabilization tensors for SGS stabilization method

	Stabilization tensor (SGS)
Codina [110]	$\boldsymbol{\tau}_U = \left\{ \frac{4\mu}{\rho h^2} + \frac{\alpha}{\rho} + \frac{2\|\boldsymbol{v}\|_\infty}{h} \right\}^{-1} \boldsymbol{I}$ $\boldsymbol{\tau}_T = \left\{ \frac{4k}{\rho h^2} + \frac{2C_p\|\boldsymbol{v}\|_\infty}{h} \right\}^{-1} \boldsymbol{I}$
Codina [98]	$\boldsymbol{\tau}_U = \left\{ \left(\frac{4\mu}{\rho h^2} + \frac{\alpha}{\rho} \right)^2 + \left(\frac{2\|\boldsymbol{v}\|_\infty}{h} \right)^2 \right\}^{\frac{-1}{2}} \boldsymbol{I}$ $\boldsymbol{\tau}_T = \left\{ \left(\frac{4k}{\rho h^2} \right)^2 + \left(\frac{2C_p\|\boldsymbol{v}\|_\infty}{h} \right)^2 \right\}^{\frac{-1}{2}} \boldsymbol{I}$

Table 2.3.4 Stabilization tensors for LSIC stabilization method

	Stabilization tensor
Tezduyar *el al*. [93]	$\tau_{LSIC} = \frac{h_{UGN}}{2}\|\boldsymbol{v}\| z$ $h_{UGN} = 2\|\boldsymbol{v}\|\left(\sum_{a=1}^{n_{en}} \|\boldsymbol{v}\cdot\nabla N_a\|\right)^{-1}$ $\mathrm{Re}_{UGN} = \frac{\rho\|\boldsymbol{v}\|h_{UGN}}{2\mu}$ $z = \begin{cases} \mathrm{Re}_{UGN}/3 & \mathrm{Re}_{UGN} \le 3 \\ 1 & \mathrm{Re}_{UGN} > 3 \end{cases}$
Tezduyar [96]	$\tau_{LSIC} = \boldsymbol{\tau}_U(1,1)\|\boldsymbol{v}\|^2$ $\boldsymbol{\tau}_U = \left\{\left(\frac{h_{RGN}}{2\|\boldsymbol{v}\|}\right)^{-2} + \left(\frac{\rho}{\alpha}\right)^{-2} + \left(\frac{\rho h_{RGN}^2}{4\mu}\right)^{-2}\right\}^{\frac{-1}{2}} \boldsymbol{I}$ $h_{RGN} = 2\left(\sum_{a=1}^{n_{en}} \|\boldsymbol{r}\cdot\nabla N_a\|\right)^{-1}, \quad \boldsymbol{r} = \frac{\nabla\|\boldsymbol{v}\|}{\|\nabla\|\boldsymbol{v}\|\|}$

Finally, the stabilization tensor in the VMS stabilization method is obtained from the same strategy shown in [85, 87-88, 90, 111] by using bubble functions as

$$\boldsymbol{\tau}_U = \left(b_1 \int b_2 \, d\Omega_e\right)\left[\begin{array}{l} \int b_2 \alpha b_1 \, d\Omega_e \boldsymbol{I} + \int b_2 \rho_f \boldsymbol{v} \cdot \nabla b_1 \, d\Omega_e \boldsymbol{I} \\ + \mu_f \int \nabla b_2 \cdot \nabla b_1 \, d\Omega_e \boldsymbol{I} + \mu_f \int \nabla b_2 \otimes \nabla b_1 \, d\Omega_e \end{array}\right]^{-1}. \qquad (2.3.15)$$

Where b_1 is the standard second order bubble function and b_2 is arbitrary asymmetric bubble function. See appendix A.

2.4. Newton-Raphson method

This section shows in detail how to solve the Brinkman-penalized Navier-Stokes equation (2.2.3) using the Newton-Raphson method. This fluid equation is a steady-state nonlinear equation and may be expressed in the residual form as

$$\tilde{\boldsymbol{R}}_U\left(\boldsymbol{\tau}_U\left(\boldsymbol{u}\right),\boldsymbol{u}\right)=\boldsymbol{0}\,. \tag{2.3.16}$$

where $\tilde{\boldsymbol{R}}_U$ is the residual or momentum equation including the stabilization terms $\left\langle \tilde{L}w,\tau L\phi\right\rangle_{\tilde{\Omega}}$, and $\boldsymbol{u}$ is the system response including velocity vector $\boldsymbol{v}$ and pressure p. Equation (2.3.16) is solved iteratively by the Newton-Raphson iteration method. If the current iterate $\boldsymbol{u}^{\mathrm{I}}$ is not a solution, i.e. if $\tilde{\boldsymbol{R}}_U\left(\boldsymbol{\tau}_U\left(\boldsymbol{u}^{\mathrm{I}}\right),\boldsymbol{u}^{\mathrm{I}}\right)\neq\boldsymbol{0}$, then the next iterate $\boldsymbol{u}^{\mathrm{I+1}}$ is computed by equating the first-order Taylor series expansion of $\tilde{\boldsymbol{R}}_U$ about $\boldsymbol{u}^{\mathrm{I}}$ to zero, i.e.

$$\begin{aligned}\tilde{\boldsymbol{R}}_U\left(\boldsymbol{\tau}_U\left(\boldsymbol{u}^{\mathrm{I+1}}\right),\boldsymbol{u}^{\mathrm{I+1}}\right)&=\tilde{\boldsymbol{R}}_U\left(\boldsymbol{\tau}_U\left(\boldsymbol{u}^{\mathrm{I+1}}+\delta\boldsymbol{u}\right),\boldsymbol{u}^{\mathrm{I+1}}+\delta\boldsymbol{u}\right)\\&\approx\tilde{\boldsymbol{R}}_U\left(\boldsymbol{\tau}_U\left(\boldsymbol{u}^{\mathrm{I}}\right),\boldsymbol{u}^{\mathrm{I}}\right)+\frac{D\tilde{\boldsymbol{R}}_U}{D\boldsymbol{u}}\delta\boldsymbol{u}=\boldsymbol{0}\end{aligned} \tag{2.3.17}$$

where $D\tilde{\boldsymbol{R}}_U/D\boldsymbol{u}$ is the tangent operator and $\delta\boldsymbol{u}$ is the incremental response which is determined from the following equation

$$\frac{D\tilde{\boldsymbol{R}}_U}{D\boldsymbol{u}}\delta\boldsymbol{u}=-\tilde{\boldsymbol{R}}_U\left(\boldsymbol{\tau}_U\left(\boldsymbol{u}^{\mathrm{I}}\right),\boldsymbol{u}^{\mathrm{I}}\right). \tag{2.3.18}$$

Upon evaluation of the incremental response $\delta \boldsymbol{u}$, the next iterate $\boldsymbol{u}^{\mathrm{I}+1}$ is updated form the sum

$$\boldsymbol{u}^{\mathrm{I}+1} = \boldsymbol{u}^{\mathrm{I}} + \delta \boldsymbol{u}. \tag{2.3.19}$$

The process of evaluating the residual $\tilde{\boldsymbol{R}}_U$ and updating the response $\boldsymbol{u}$ continues until the solution converges.

2.4.1. Reynolds-ramping initial guess for Newton-Raphson method

Selecting appropriate initial value $\boldsymbol{u}^0$ is very critical for using Newton-Raphson iterative method because this method may fail to converge if the initial value is too far from the true solution. Particularly, the solvability is very sensitive to the initial value when the governing equation is highly nonlinear. During the topology optimization progress, the complex structures make the Brinkman-penalized Navier-Stokes equation significantly nonlinear even if the Reynolds number is not high. Therefore, we need a very robust scheme to set up proper initial values to obtain the true solution without failure. In fluid dynamics problems, the nonlinear terms are approximately proportional to the Reynolds number; therefore, one can select appropriate initial value by iteratively solving less nonlinear problem as shown in Figure 2.4.1.

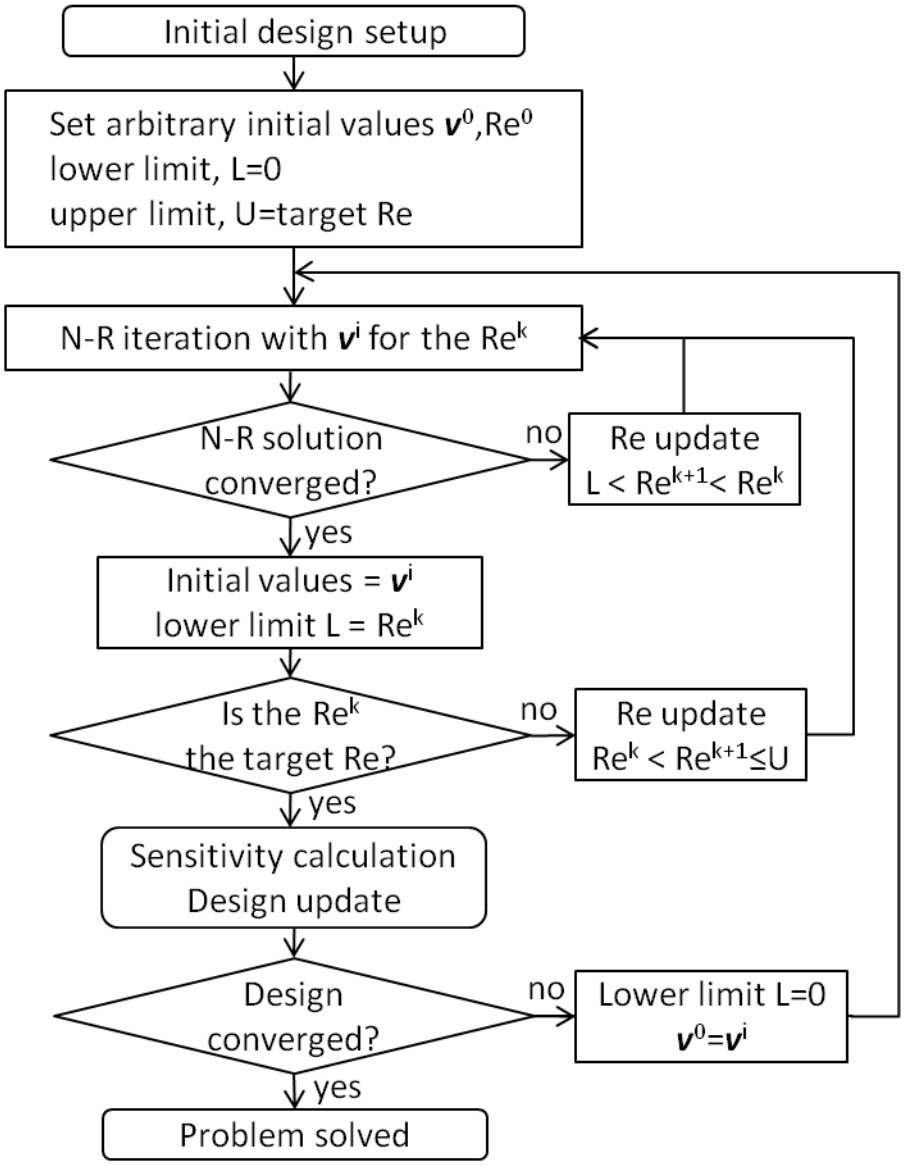

Figure 2.4.1. Flow chart of the Reynolds-ramping initial guess

1) Start fluid analysis for a low Reynolds number with arbitrary initial values

2) Get a converged solution for the Reynolds number.

3) If the solution does not converge, try to solve a lower Reynolds number flow.

4) If the solution converges, use that solution as the initial values for a bigger Reynolds number flow

Repeat 2), 3) and 4) until the full Reynolds number is reached.

2.4.2. Stabilization tensor update scheme

Two options can be considered regarding the update of the stabilization tensors during the Newton-Raphson iteration. First, the values of the stabilization tensors are not fixed and their variations are taken into account in calculating the Jacobian matrix in each Newton-Raphson iteration. With this scheme, the implicit derivative $D\boldsymbol{\tau}_U/D\boldsymbol{u}$ must be calculated as shown in equation (2.3.20).

$$\frac{D\tilde{\boldsymbol{R}}_U}{D\boldsymbol{u}} = \left[\frac{\partial \tilde{\boldsymbol{R}}_U}{\partial \boldsymbol{\tau}_U} \cdot \frac{D\boldsymbol{\tau}_U}{D\boldsymbol{u}} + \frac{\partial \tilde{\boldsymbol{R}}_U}{\partial \boldsymbol{u}} \right]_{\text{at } \boldsymbol{u}=\boldsymbol{u}^{\mathrm{I}}} \tag{2.3.20}$$

This process is referred to as “simultaneous update scheme”. Second, the value of the stabilization tensor is fixed based on the previous Newton-Raphson iteration result $\boldsymbol{u}^{\mathrm{I}}$ without taking its variation into account when calculating the Jacobian matrix. Then, the Jacobian matrix is determined as:

$$\frac{D\tilde{\boldsymbol{R}}_U}{D\boldsymbol{u}} = \left[\frac{\partial \tilde{\boldsymbol{R}}_U}{\partial \boldsymbol{u}} \right]_{\text{at } \boldsymbol{u}=\boldsymbol{u}^{\mathrm{I}}} . \tag{2.3.21}$$

This is referred to as "iteration-lagging update scheme".

Of the two update schemes, the former simultaneous update scheme is strongly recommended for the topology optimization. Analytically calculating the variation of the stabilization tensor is complex and requires more computational cost in each Newton-Raphson iteration. However, the Jacobian matrix $\frac{D\tilde{\boldsymbol{R}}_U}{D\boldsymbol{u}}$ becomes more accurate with the term $\frac{\partial \tilde{\boldsymbol{R}}_U}{\partial \boldsymbol{\tau}_U} \cdot \frac{D\boldsymbol{\tau}_U}{D\boldsymbol{u}}$ and, as a result, the first scheme requires fewer Newton-Raphson iterations than the second scheme.

To verify the analysis method described in this chapter, an example problem P2 is examined. As shown in Figure 2.4.2 and Table 2.4.1, immersed boundaries and a solid region are implemented instead of the no-slip boundary condition. The Reynolds number is 1000 and α_s is set to 10^8. (Darcy number in the solid region is 10^{-8}.) The Reynolds-ramping initial guess scheme is used to properly set the initial guess and get the true solution. Flow analyses for ReL=10, 100, 400 and 700 flows sequentially precede before the flow analysis at ReL=1000. Figure 2.4.3 shows the convergence history during the last three analyses for ReL=400, 700 and 1000 flow. There is no noticeable difference during the analyses for ReL=1 and 100 flow. In this case, the simultaneous update scheme is 28% faster than the iteration-lagging update scheme.

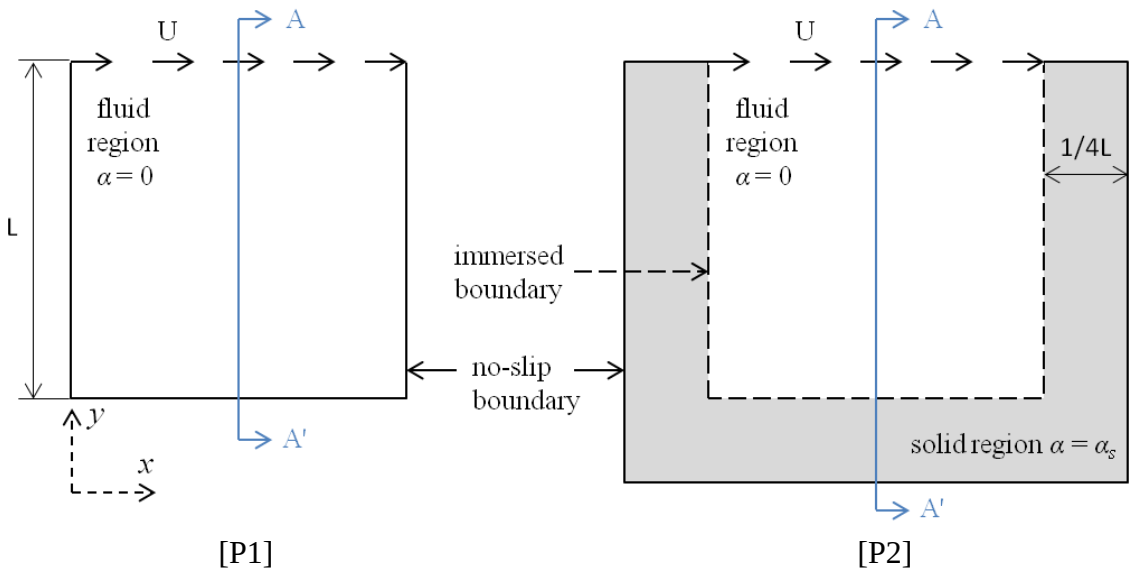

Figure 2.4.2. 2D lid-driven cavity problems [P1] with no-slip boundary [P2] with solid region and immersed boundary

Table 2.4.1 [P2] Analysis setup

Reynolds number	ReL=400, 1000
Domain size	L×L = 1×1 (1.5×1.25)
Mesh	48×40
Shape function ($\boldsymbol{v}$, p)	Q4Q4
Stabilization method	SUPG+PSPG, GLS, SGS
Brinkman penalization	α_s=10^4~10^{16}

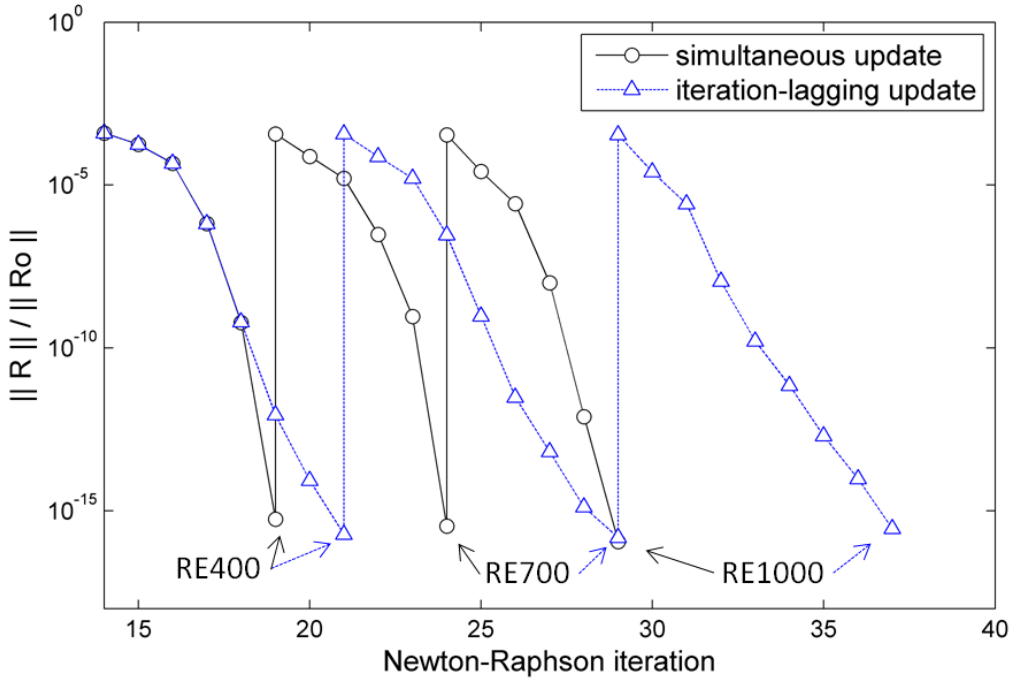

Figure 2.4.3. [P2] Convergence history according to different stabilizing tensor update schemes: simultaneous and iteration-lagging update schemes

Besides using the simultaneous update scheme is much more important in performing sensitivity analysis for the topology optimization. During the topology optimization, the physical properties in the stabilization tensor, such as ρ_f, μ_f and α, are assumed to be control parameters. Particularly, the Brinkman-penalization parameter α is a primary control parameter with significantly large values in the solid regions. Therefore, assuming constant stabilization tensors in each Newton-Raphson iteration without considering $\frac{D\boldsymbol{\tau}_U}{D\alpha}$ degrades the accuracy of the sensitivity analysis.

Whereas the simultaneous update scheme is viable in the SUPG, PSPG, GLS and SGS methods, it is difficult to apply for the VMS stabilization method in which its stabilization tensor is determined from the inverse of a matrix consisting of physical

properties and system response as shown in equation (2.3.15). Thus it is inefficient to calculate the derivatives of the stabilization tensor with respect to system response or physical properties, $D\boldsymbol{\tau}_U/D\boldsymbol{u}$ or $D\boldsymbol{\tau}_U/D\alpha$ respectively.

Furthermore, I discovered no significant advantage of using the VMS stabilization method with its complicated stabilization tensor calculation compared to using the SGS method with a relatively simple stabilization tensor. Consequently, I mainly tested the SUPG, PSPG, GLS and SGS stabilization methods for the topology optimization problem. Still there may, however, be a room for improvement in the VMS stabilization method based on the proper selection of the asymmetric bubble function b_2 in equation (2.3.15). Further rigorous study is needed to implement the VMS stabilization method.

2.5. Numerical issues

This section presents a guideline to pre-assign the Brinkman penalization parameter α_s, and discusses numerical instability at the free-fluid and solid interfaces. The pre-assigned value of α_s influences the accuracy of system analysis and further the design sensitivity calculation. The local instability does not degrade the overall solution in system analysis, but I mention here because the instability becomes problematic later in the sensitivity analysis at the design optimization level.

2.5.1. Lower limit of the Brinkman penalization parameter

To obtain accurate solution at the system analysis level is a primary issue because the accuracy of the design sensitivity mainly depends on the accuracy of the system analysis.

When solving the Brinkman-penalized Navier-Stokes equation, the error estimate of the velocity field in the H^1-norm over the whole domain is the order of $\mathcal{O}\left(\alpha_f + \alpha_s^{-1/4}\right)$, while the L^2-norm of the velocity inside the solid body is $\mathcal{O}\left(\alpha_s^{-3/4}\right)$ as proved in [43-44]. In theory, the higher α_s is set, the smaller the mathematical error is. In practice, too large of a value for α_s however makes the contribution from the convection and diffusion terms negligibly small compared to the Brinkman penalization term. This would destroy the conditioning of the Jacobian matrix. Furthermore, too large of a value for α_s would cause inaccurate sensitivity analysis because it would worsen the condition of the multiplication, $\left(\frac{\partial \tilde{\boldsymbol{R}}_U}{\partial \boldsymbol{u}}\right)^{-T} \frac{\partial \tilde{\boldsymbol{R}}_U}{\partial \alpha}$, Therefore, the value of α_s must be assigned within a proper range.

Several Brinkman penalization parameters, from 10^4 to 10^{16}, are tested for the 2D lid-driven cavity problem that includes a solid region as shown in Figure 2.4.2. Q4Q4 element with square mesh is used. The mesh size for problem P1 and P2 is 32×32 and 48×40, respectively to have the same element length scale. The Reynolds number is 400. Figure 2.5.1 shows different horizontal velocity results depending on the value of α_s. When α_s is greater than 10^6 (the Darcy number in the solid region is 10^{-6}), the solutions are well converged to the original solution calculated with no-slip boundary conditions.

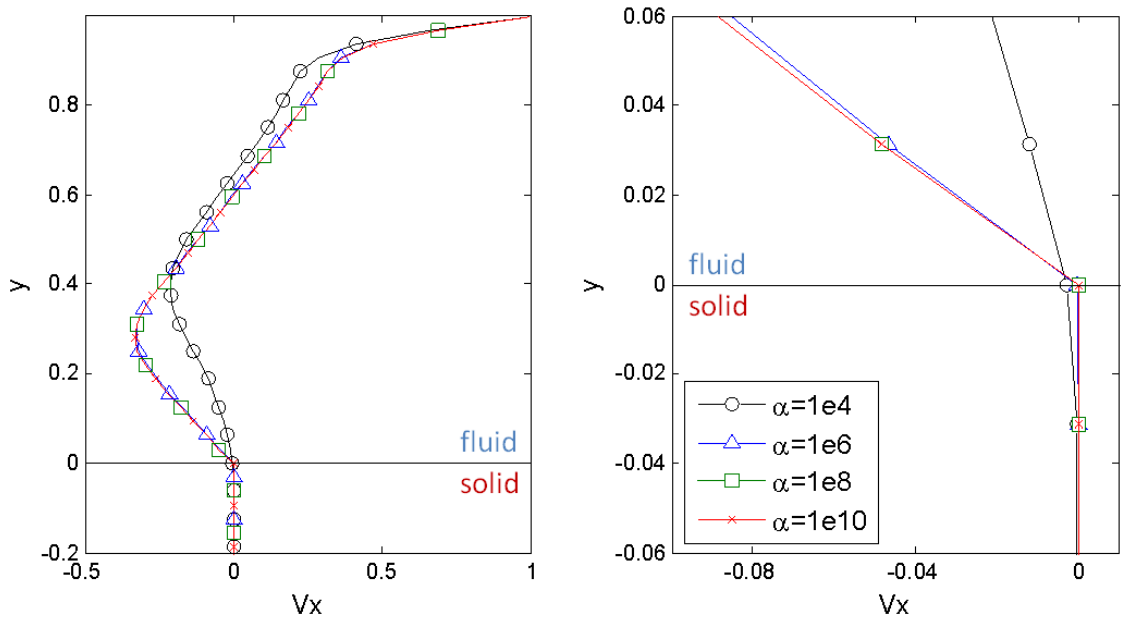

Figure 2.5.1. [P2] Horizontal velocity at section A-A′ according to α_s (ReL=400, SUPG+PSPG) (a) global velocity (b) local view at fluid-solid interface

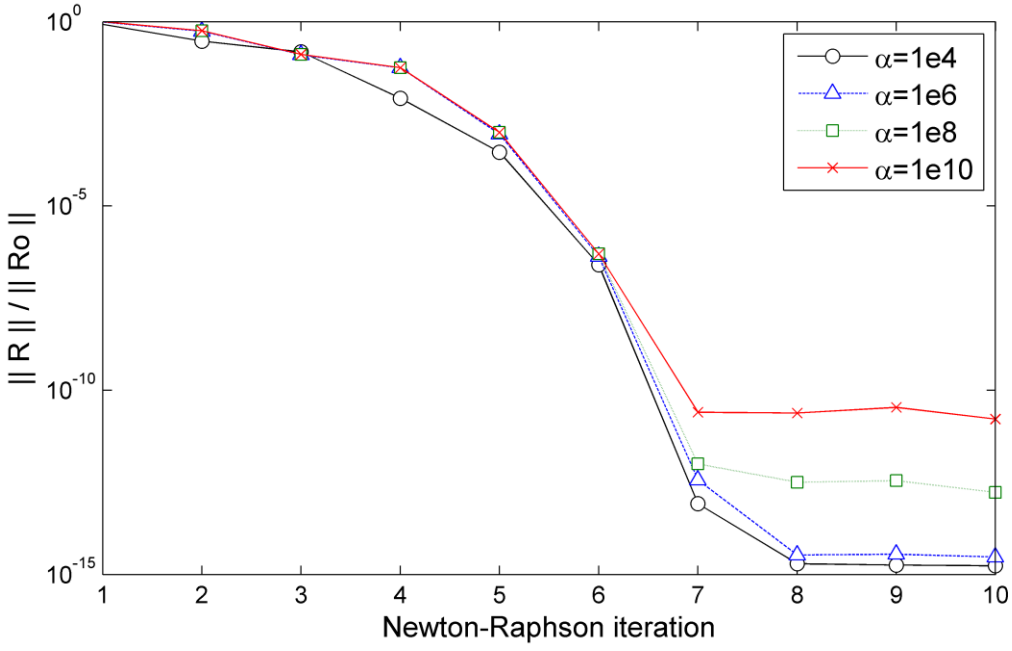

Figure 2.5.2. [P2] Convergence histories according to α_s (ReL=400, SUPG+PSPG)

In the same manner, 2D backward-facing step flow analysis is performed first with no-slip boundary conditions and second with immersed boundary conditions and solid region. α_s is set to from 10^2 to 10^{18}. Analysis domain and boundary conditions are described in Figure 2.5.3 and Table 2.5.1. Q4Q4 element with 300×40 or 600×80 square mesh is used for problems P4 and a equivalent-size mesh is used for problem P3. The Reynolds number ReH is set to 100. To verify the analysis method, COMSOL 3.5a is used to solve problem P3 while the solution of P4 is obtained by using my own codes; Figure 2.5.4 and Figure 2.5.5 show the two results. Again, when α_s is greater than 10^6, the solutions of P4 are well converged to the solution of P3 (with no-slip boundary condition).

Figure 2.5.1 and Figure 2.5.6 present that the zero-velocity condition inside the solid structure and no-slip boundary condition at the immersed boundary (fluid-solid interface) are reasonable realized as the value of the Brinkman penalization parameter increases. The convergence of Newton-Raphson iteration is slightly better when a smaller value of the Brinkman penalization parameter as shown in Figure 2.5.2 and Figure 2.5.7, yet overall they show good convergence histories. In conclusion, several tests in other configurations show $\alpha_s=10^6$ (the Darcy number in the solid region is 10^{-6}) is the proper lower limit for reasonable use of the Brinkman-penalization method.

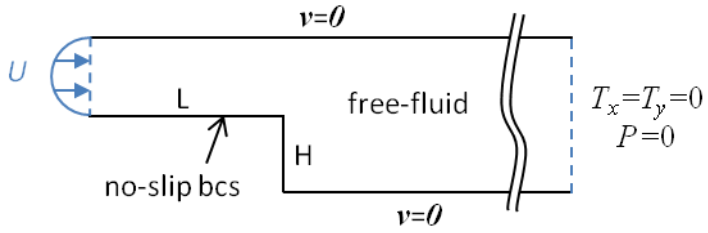

[P3]

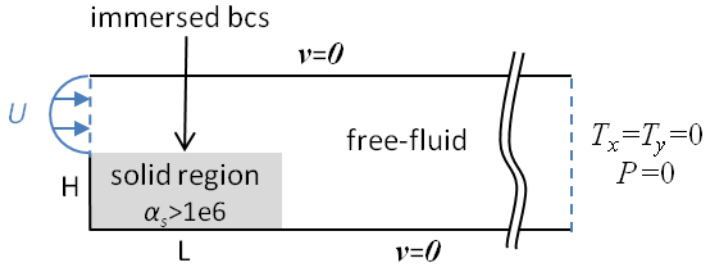

[P4]

Figure 2.5.3. 2D backward-facing step flow [P3] with no-slip boundary conditions [P4] with solid solid structure and immersed boundaries

Table 2.5.1 [P4] Analysis setup

Reynolds number	ReH=100
Domain size	30×2 (L×H=3×1)
Mesh	300×40, 600×80
Shape function (***v***, *p*)	Q4Q4
Stabilization method	SUPG+PSPG, GLS, SGS
Brinkman penalization	$\alpha_s=10^4$~10^{18}

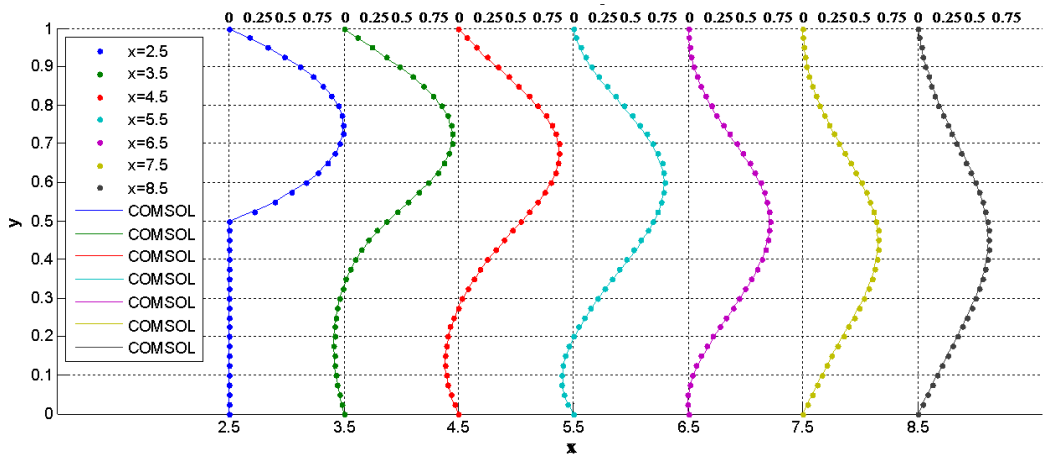

Figure 2.5.4. [P4] Horizontal velocity results of P3 and P4 (α_s=10^6)

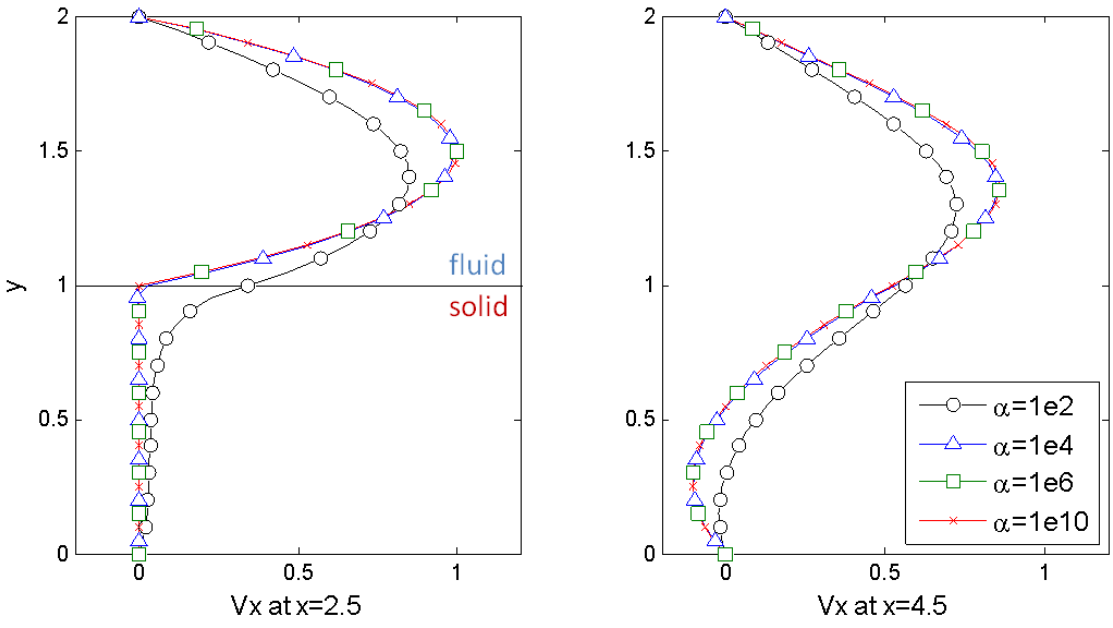

(a) (b)

Figure 2.5.5. [P4] Horizontal velocity at (a) x=2.5, (b) x=4.5 with various α_s (ReL=100, SUPG+PSPG)

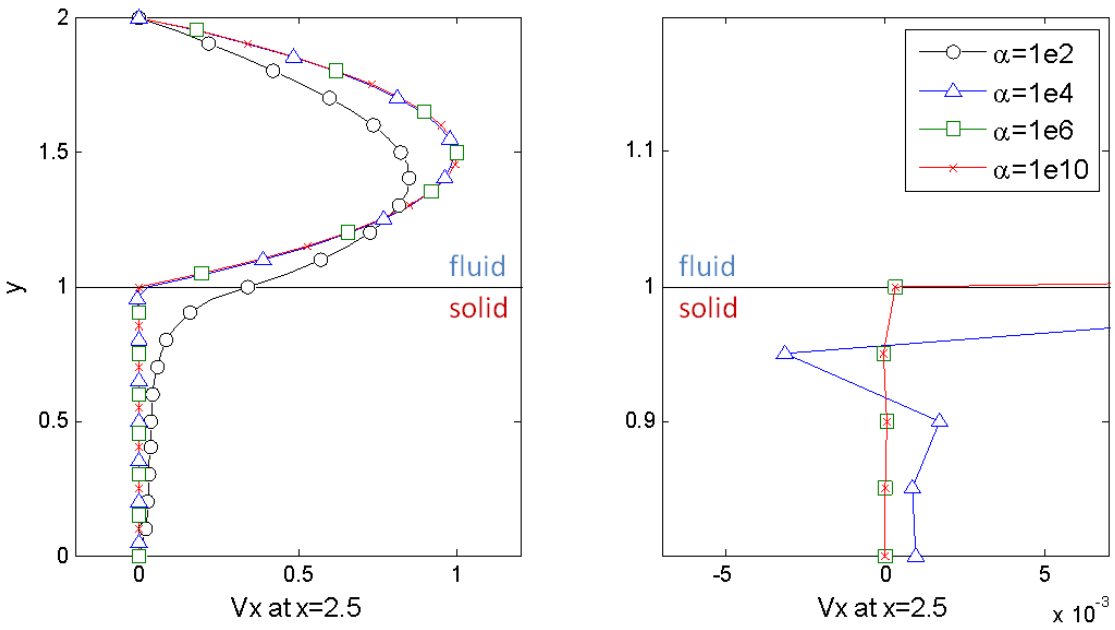

Figure 2.5.6. [P4] Horizontal velocity oscillation various α_s (ReL=100, SUPG+PSPG)
(a) global velocity (b) local view at fluid-solid interface

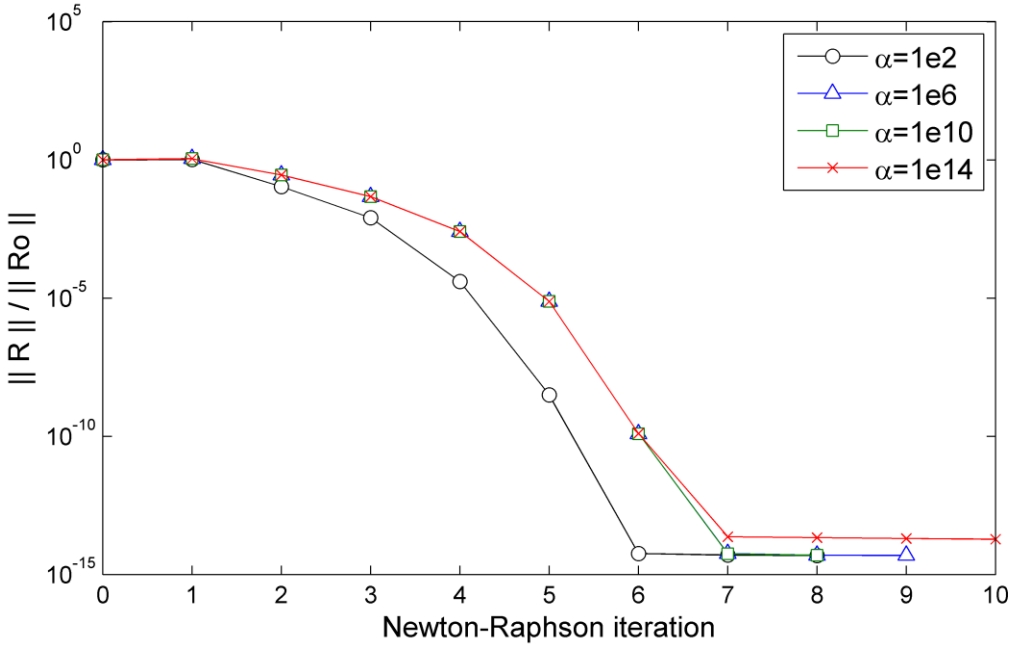

Figure 2.5.7. [P4] Convergence history according to different Brinkman penalization parameters

2.5.2. Numerical issues at fluid-solid interfaces (immersed boundaries)

Although the overall velocity profiles are consistent with the solutions obtained by using the traditional no-slip boundary conditions, there sometimes exist disturbances, such as oscillation and over-diffusion, at the immersed boundary. For example, if the velocity profile shown in Figure 2.5.6(a) is examined again after magnifying it near the immersed boundaries (solid-fluid interfaces), element-scale oscillations of velocity or pressure are observed, as shown in Figure 2.5.6(b). Figure 2.5.8 describes another example problem which shows the velocity oscillation at the immersed boundaries. A solid obstacle lies in the middle of the analysis domain, and uniform flow motion is applied to inlet and free-stream boundary conditions. The velocity solution obtained by using the Brinkman penalization method is presented in Figure 2.5.9. Consistent with the previous result of P2 and P4, the velocity profile shows good convergence when α_s is greater than 10^6, but the velocity oscillation at the fluid-solid interface is again discovered.

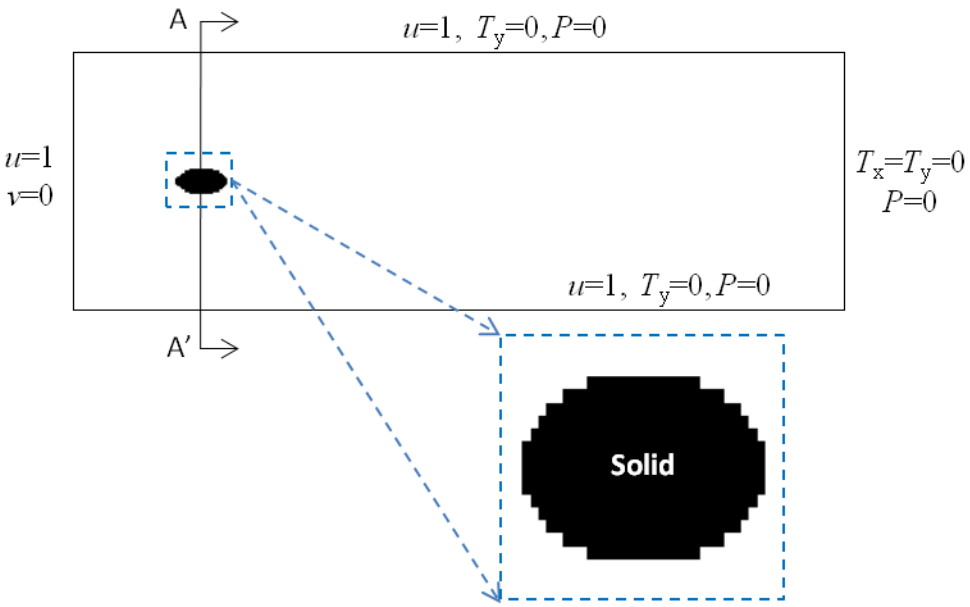

(a)

Reynolds number	ReL=100
Domain size	3×1
Mesh	300×100, 600×200
Shape function (***v***, *p*)	Q4Q4
Stabilization method	SUPG+PSPG, GLS, SGS
Brinkman penalization	$\alpha_s=10^4 \sim 10^{16}$

(b)

Figure 2.5.8. [P5] 2D flow problem around oval obstacle (a) design domain and bcs (b) analysis setup

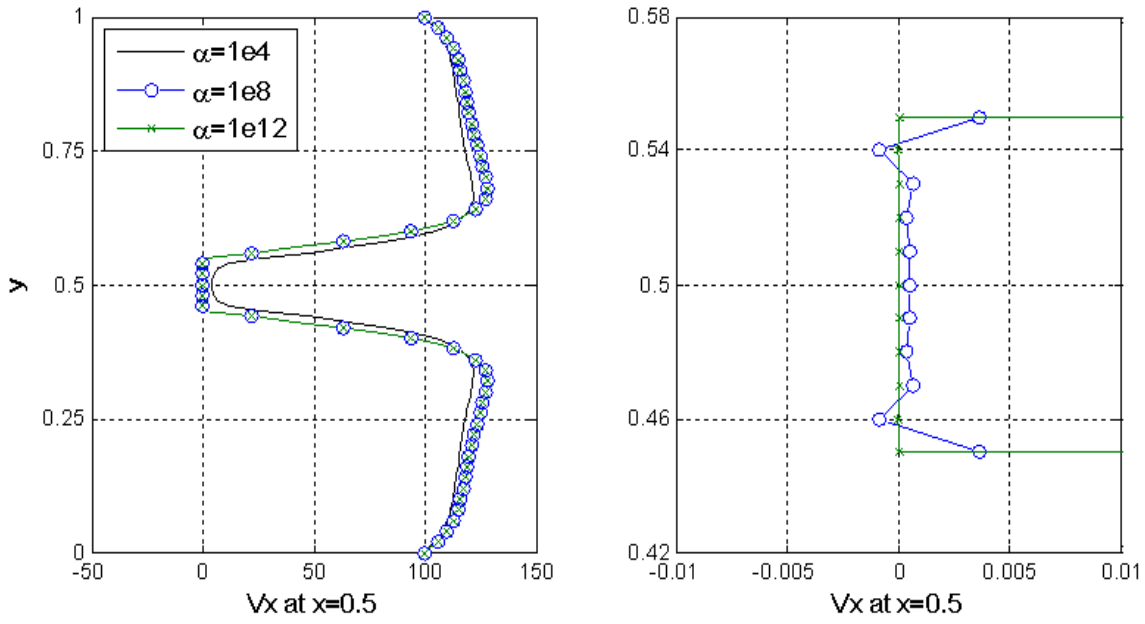

(a) (b)

Figure 2.5.9. [P5] Horizontal velocity results (section A-A′) accoring to the value of Brinkman penalization parameter (a) global velcoity (b) local velocity view

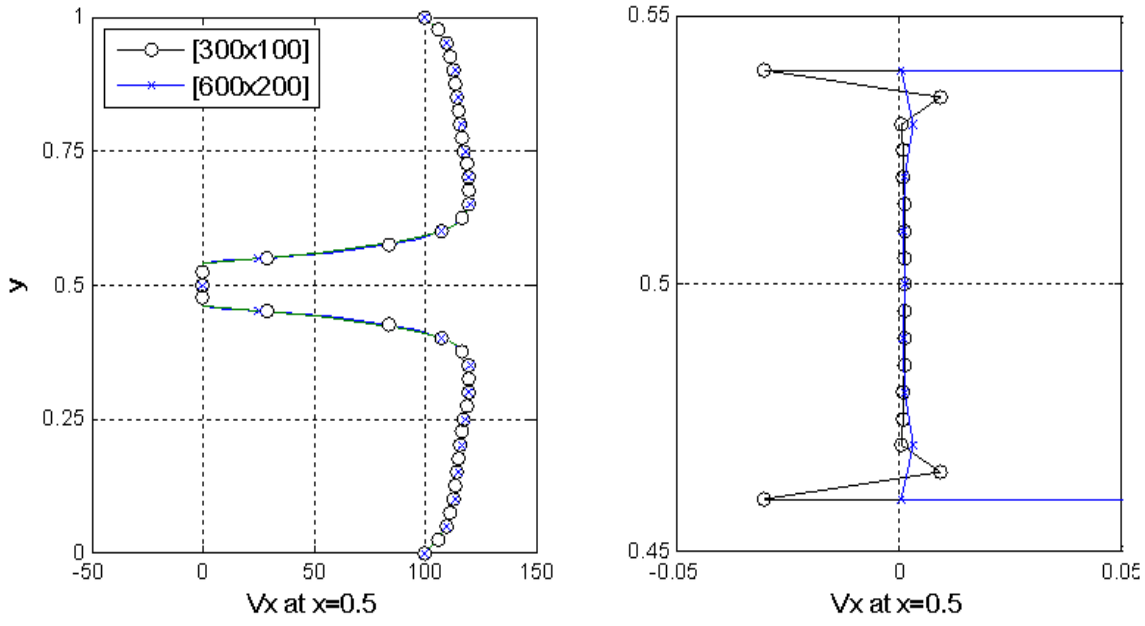

(a) (b)

Figure 2.5.10. [P5] Horizontal velocity results (section A-A′) accoring to different mesh sizes (a) global velcoity (b) local velocity view

In porous flow analysis, velocity oscillation at the interface between porous and solid regions is a well-known numerical phenomenon [112]. This is because the Darcy model inherits a conflict among the shear stress condition, mass flow rates and velocity continuity condition at the interface. Thus, the oscillation due to the Darcy model is not a mesh refinement problem. However, the oscillations in this study, which occur at the immersed boundary location, are a mesh refinement problem, although the Brinkman-penalized Navier-Stokes equation is derived based on similar porous flow physics. First, the velocity gradient changes too sharply at the immersed boundaries for the SUPG stabilization methods to correctly capture the velocity profile. Second, meshes used during topology optimization process are generally non body-conforming, as shown in Figure 2.5.8(a); therefore there are singular corner points that cause a pressure oscillation. Figure 2.5.10 shows that the amount of oscillation is reduced with mesh refinement.

Although a denser mesh at the fluid-solid interfaces can prevent or soothe the oscillation, it is almost impossible to apply a dense mesh for the topology optimization problem. During the topology optimization process, the shape of the solid structure constantly changes and accordingly, the location of the interfaces moves at each design step. We therefore must remesh at each design step to apply a sufficiently dense mesh at the local area, which negates all the advantages of using the fictitious domain approach and significantly increases the computational cost.

This study also examines the possibility of reducing the oscillation by applying different stabilization methods, such as the SUPG+PSPG, GLS and SGS stabilization methods. The analysis results obtained using different stabilization methods are presented from Figure 2.5.11 to Figure 2.5.16. At the global scale, the results do not differ

significantly from those obtained using the SUPG+PSPG, GLS and SGS stabilization methods. However, the magnified local velocity view at the solid-fluid interfaces reveals differences between the three solutions.

The GLS stabilization method generally results in the smaller oscillation than the SUPG+PSPG stabilization method, regardless of the value of the Brinkman penalization parameter α. This result seems to be contrary to the theory because the GLS stabilization magnifies the oscillation produced by the SUPG method when the 1D convection-diffusion-reaction (CDR) example is solved [75]. This is probably because there are two main differences between the CDR example and these problems P2, P4 and P5. First, the high reaction is not constantly positive in the direction of flow stream. Second, not only the high reaction term but also corner singularities result in the oscillation. The SGS stabilization method produces slightly over-diffused solutions preventing oscillated solutions in case P2. However, this cannot be generalized since, in other cases, the SGS produces more severe oscillations than the SUPG+PSPG stabilization method. For example, the velocity profile obtained by using the SGS stabilization method shows the worst oscillation at the immersed boundaries in cases P4 and P5.

The difference in solutions obtained by different stabilization tensors is not significant although the Newton-Raphson convergence ratios are slightly inconsistent. Also, the effect of the LSIC stabilization method is negligible because the Reynolds number tested is not sufficiently high. Also, it should be mentioned that the magnitude of oscillation depends on the value of the Brinkman penalization parameter. As α_s increases, the obtained solutions first show over-diffusion, then large oscillation and finally small oscillation.

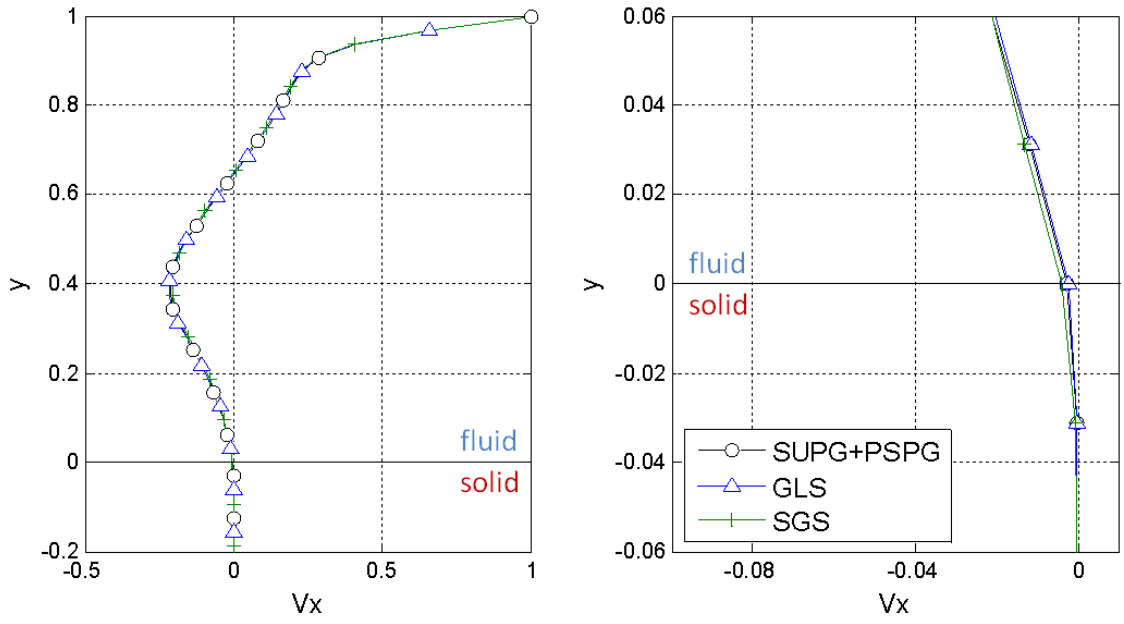

Figure 2.5.11. [P2] Horizontal velocity at section A-A′ with $\alpha_s=10^4$, ReL=400 using different stabilization methods (a) global velocity (b) local view

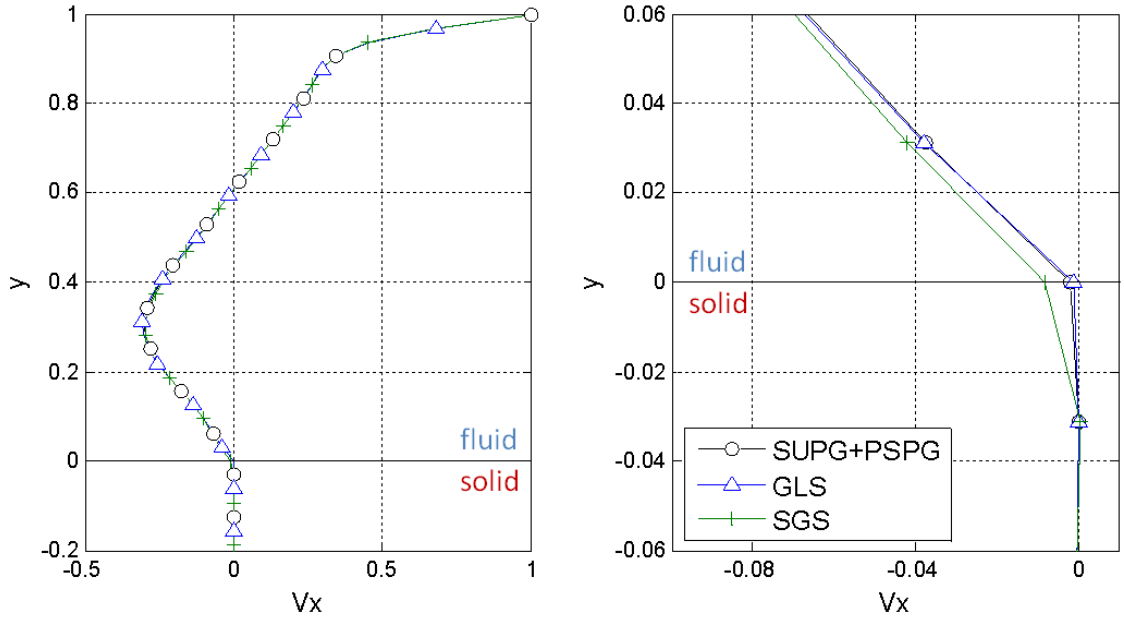

Figure 2.5.12. [P2] Horizontal velocity at section A-A′ with $\alpha_s=10^5$, ReL=400 using different stabilization methods (a) global velocity (b) local view

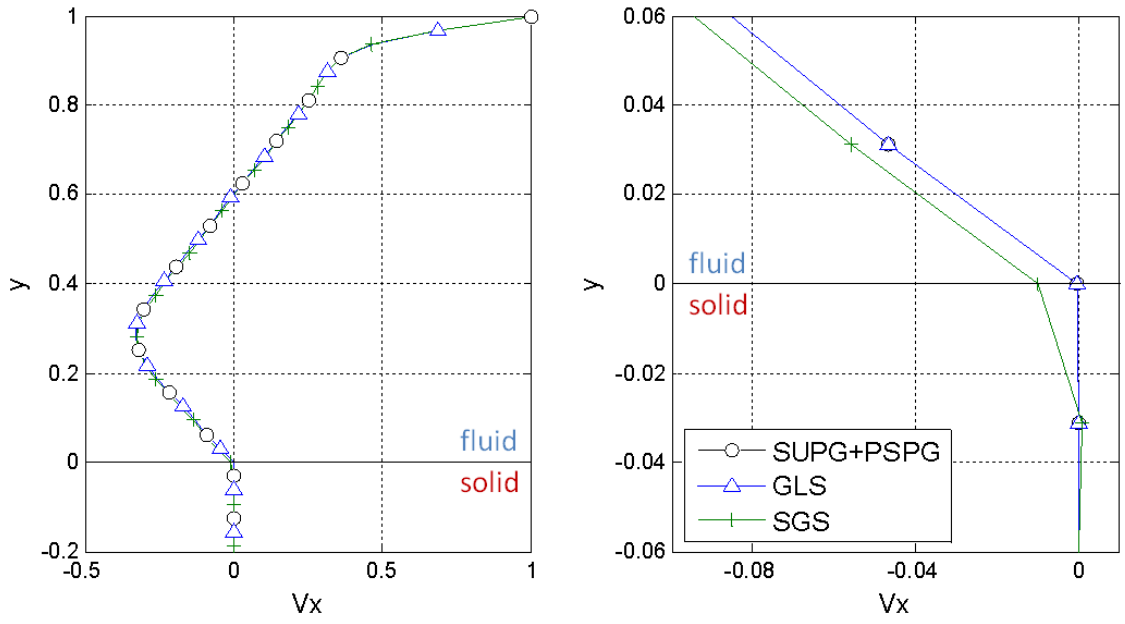

(a) (b)

Figure 2.5.13. [P2] Horizontal velocity at section A-A′ with α_s=10^6, ReL=400 using different stabilization methods (a) global velocity (b) local view

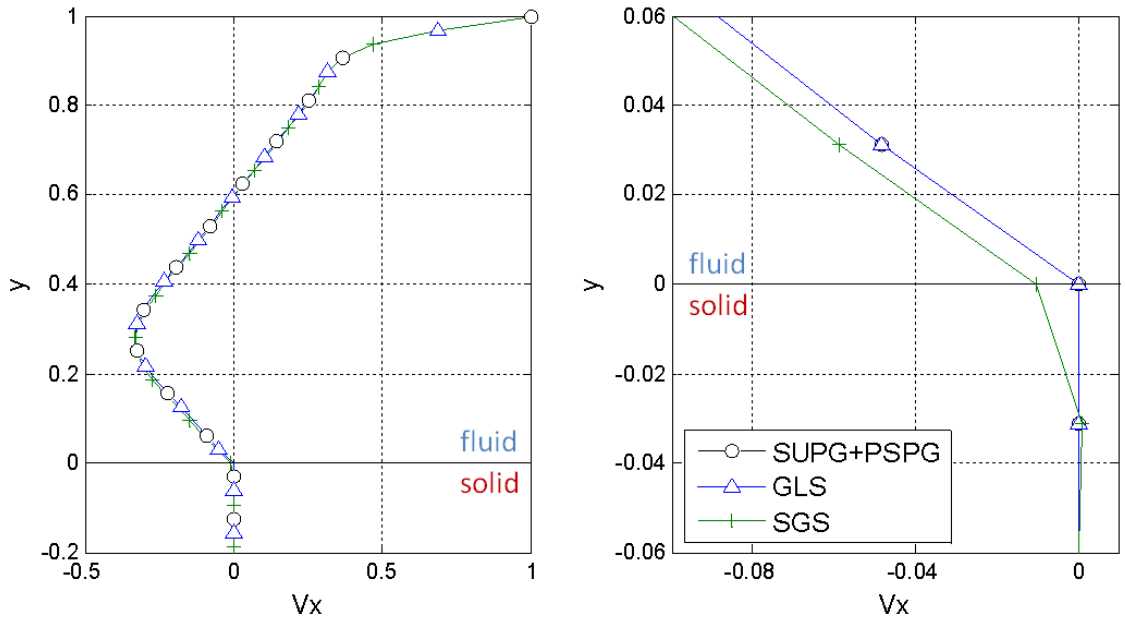

(a) (b)

Figure 2.5.14. [P2] Horizontal velocity at section A-A′ with α_s=10^{10}, ReL=400 using different stabilization methods (a) global velocity (b) local view

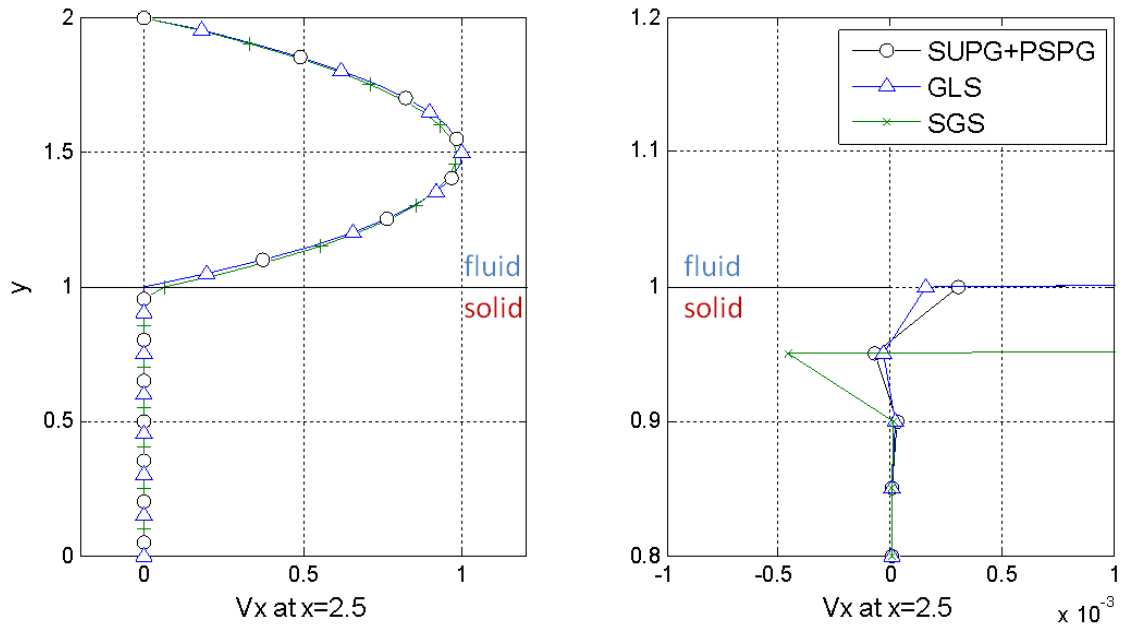

(a) (b)

Figure 2.5.15. [P4] Horizontal velocity oscillation according to stabilization methods (a) global velocity (b) local velocity view at fluid-solid interface

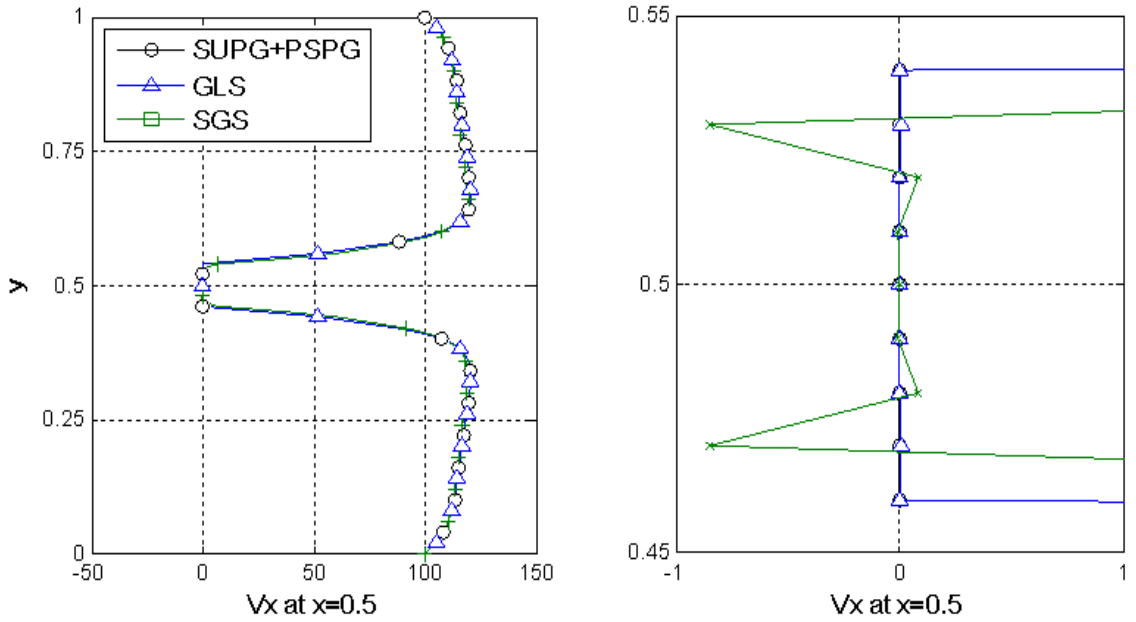

(a) (b)

Figure 2.5.16. [P5] Horizontal velocity results (section A-A′) accoring to different stabilization methods (a) global velcoity (b) local velocity view

Various analyses with different configurations indicate that the GLS stabilization method generally produces the best solution with the weakest oscillation. More mathematically rigorous study of how each stabilization method effects on the oscillation phenomenon is needed. Also, too small of a value for the Brinkman penalization parameter not only prevents a converged solution, but also increases the magnitude of oscillation. Mathematical verification of the relations is left for further research.

Finally, it should be noted that this local instability might later spoil the optimization solution. This instability does not degrade the overall solution at the level of system analysis. Brinkman penalization is mathematically justified from the viewpoint of system analysis [43-44]. The relation between the local oscillation and other numerical instabilities observed during the optimization process will be discussed in detail in section 3.3.3.

2.6. Summary

In this chapter, I revisited a fictitious design approach to analyze the physics in fluid and solid regions together with one equation by explaining the concept of the Brinkman-penalized Navier-Stokes equation and the homogenized thermal transport equation. SUPG, PSPG, GLS, VMS and LSIC stabilization methods and various schemes to calculate their stabilization tensors were briefly introduced and tested. The Newton-Raphson method for solving the nonlinear equation was described in detail. Reynolds-Ramping initial guess strategy and a simultaneous stabilization tensor update scheme

were presented, which are essential in obtaining robust and fast solutions for highly nonlinear topology optimization problems.

With example problems, a guideline to set a proper lower bound of the Brinkman penalization parameter was presented. When the Brinkman penalization parameter is greater than 10^6 ($Da=10^{-6}$), the zero-velocity condition in the solid regions and the no-slip boundary condition at solid boundaries are generally satisfied. Velocity and pressure oscillations at the fluid-solid interfaces were presented and investigated.

These numerical instabilities are a mesh-refinement problem unlike the oscillation occurring in porous flow analysis. This oscillation becomes stronger as the Reynolds number increases and a coarser mesh is used. Also, the magnitude of oscillation depends on the value of the Brinkman penalization parameter increases. As α_s increases, the obtained solutions show over-diffusion, large oscillation and small oscillation, sequentially.

Although the solutions obtained from different stabilization methods are overall very similar to each other, discrepancies are found near fluid-solid interfaces. The SUPG+PSPG and GLS stabilization methods produce the velocity and pressure oscillation, while the SGS stabilization method produces the strongest oscillation or an over-diffused solution. No notable difference is found due to the change of a stabilization tensor.

CHAPTER 3

TOPOLOGY OPTIMIZATION OF NAVIER-STOKES FLOW PROBLEMS

3.1. Introduction

This chapter investigates the topology optimization method of Navier-Stokes flow systems, extending previous studies concerning Stokes flow systems [45-46, 51, 100-102]. Topology optimization method involves a great number of discrete design variables; therefore a very efficient algorithm should be implemented to solve topology optimization problems. In order to use gradient-based optimization methods which are typically efficient in problems with many design variables, the discrete design variables are relaxed by using continuous interpolation functions [1, 113]. Then the derivatives of an objective function with respect to the design variables are calculated. The adjoint sensitivity method for a steady state nonlinear system [114] is applied to calculate the derivatives.

Numerical issues, such as element-scale cavities and boundary oscillation phenomenon, which deteriorate the convergence property, are presented and investigated. These numerical issues have not appeared or been discussed in previous topology

optimization studies of Stokes flow systems or low-Reynolds number flow systems [45-46, 51, 100-102]. Filtering methods [115-117], different stabilized finite element methods and a move-limit scheme are suggested and examined to overcome the numerical issues. Unlike the well-known checkerboard pattern in topology optimization [1, 113], filtering methods such as the density filter and the sensitivity filter do not completely suppress the cavities and boundary oscillations. Instead, these numerical instabilities are successfully circumvented with the easy implementation of a move-limit scheme. Finally, 2D and 3D design problems are presented and physically interpreted. The objective function is the minimization of kinetic energy dissipation or drag minimization.

The outline of Chapter 3 is as follows. Section 3.2 presents the sensitivity analysis with RAMP interpolation function and the adjoint sensitivity method. Section 3.3 investigates numerical instabilities and suggests how to resolve them. After presenting several 2D and 3D design problems in section 3.4, summaries and observations are given in section 3.5.

3.2. Sensitivities analysis for nonlinear problems

Topology optimization determines optimized distribution of two-phase material, such as solid and void (free-fluid), in a design domain. The material phase is determined by local material properties, which are controlled by a local design variable $\varphi(\boldsymbol{r})$ which is zero in free-fluid regions and unity in the solid regions. For example, if a local design variable is unity (φ=1), the local element or the local point $\boldsymbol{r}$ is in the solid region Ω_s having solid material properties. On the contrary, if a local design variable is zero (φ=0),

it is in the void or free-fluid region with void or fluid material properties. During the topology optimization process, the value of the local design variables (0 or 1) is set to satisfy given objectives and the structural topology evolves during the topology optimization process.

The topology optimization is fundamentally a 0-1 discrete optimization problem. There are many efficient algorithms to solve discrete optimization methods; however a gradient-based optimization method is generally preferred for topology optimization since the topology optimization method involves a great number of design variables. This section describes how to calculate the design sensibility in an efficient way by using relaxation scheme and adjoint sensitivity method.

3.2.1. Relaxation of variables for topology optimization

To efficiently obtain the design sensitivity, the most commonly used approach in topology optimization problems is to replace the discrete variables with continuous variables and then introduce some form of penalty that steers the solution to discrete values. RAMP (Rational Approximation of Material Properties) method is one of the interpolation methods, which has been mainly studied in the topology optimization of fluid mechanics problems. Following the pioneering work [39], this study also uses the RAMP interpolation method to interpolate the Brinkman penalization parameter $\alpha(\varphi)$ as

$$\alpha(\varphi) = \alpha_s - (\alpha_s - \alpha_f)\left(\frac{1-\varphi}{1-\varphi_{\min}}\right)\left(\frac{1-\varphi_{\min}+q_\alpha}{1-\varphi+q_\alpha}\right) \tag{3.1.1}$$

Here, $\varphi(\boldsymbol{r})=0$ or $\varphi_{\min}$ corresponds to $\alpha_f=0$ and $\varphi(\boldsymbol{r})=1$ corresponds to $\alpha_s \approx \infty$ at the location $\boldsymbol{r}$.

Then, the Brinkman-penalization term $\alpha_s \boldsymbol{v}$ is applied in the solid regions ($\varphi=1$) to enforce the zero velocity condition inside solid structures and the no-slip boundary conditions at solid boundaries. Meanwhile, the original Navier-Stokes equation is solved in the free-fluid regions ($\varphi=0$). The parameter q_α is a penalty parameter that is used to control the level of intermediates region during the optimization process [39]. The above formula (3.1.1) is commonly used in the literature [46, 50, 118-120]. The relations between the design variable and the physics in the free-fluid and solid regions becomes as shown in Table 3.2.1.

Table 3.2.1 Design variables and physical properties

	Fluid region	**Solid region**
Design variable	$\varphi(\boldsymbol{r}) = 0, \varphi_{\min}$	$\varphi(\boldsymbol{r}) = 1$
Brinkman penalization parameter	$\alpha(\varphi) = \alpha_f = 0$	$\alpha(\varphi) = \alpha_s \approx \infty$
Momentum equation	$\rho_f \boldsymbol{v} \cdot \nabla \boldsymbol{v} - \mu_f \nabla^2 \boldsymbol{v} + \nabla p = \boldsymbol{f}$	$-\mu_f \nabla^2 \boldsymbol{v} + \alpha \boldsymbol{v} + \nabla p = \boldsymbol{f}$ $\boldsymbol{v} \approx \boldsymbol{0}$

It is noted that the effective viscosity was sometimes applied instead of dynamic viscosity and implemented as an additional design property [46, 118] with RAMP interpolation or linear interpolation schemes given by

$$\mu_{eff}(\varphi) = \mu_s - (\mu_s - \mu_f)\left(\frac{1-\varphi}{1-\varphi_{\min}}\right)\left(\frac{1-\varphi_{\min}+q_\mu}{1-\varphi+q_\mu}\right) \tag{3.1.2}$$

$$\mu_{eff}(\varphi) = \frac{(1-\varphi)\mu_f + (\varphi-\varphi_{\min})\mu_s}{(1-\varphi)+(\varphi-\varphi_{\min})}. \tag{3.1.3}$$

However, this study only uses the Brinkman-penalization parameter as a design property because no significant advantage to using the additional design property is shown in my experience. Furthermore, one more control variable q_μ in equation (3.1.2) should be selected rather heuristically, which makes the optimization problem more complicated.

3.2.2. Adjoint sensitivities for steady-state nonlinear systems

The process of evaluating the residual $\tilde{\boldsymbol{R}}_U$ and updating the response $\boldsymbol{u}$ continues until the solution converges. In a sensitivity analysis, the residual $\tilde{\boldsymbol{R}}_U$ and the system response $\boldsymbol{u}$ are expressed as functions of the design variables vector $\boldsymbol{\varphi}$ as

$$\tilde{\boldsymbol{R}}_U\left(\boldsymbol{u}(\boldsymbol{\varphi}), \boldsymbol{\varphi}\right) = \boldsymbol{0}. \tag{3.1.4}$$

In an optimization problem, the objective function has to be minimized subject to certain design constraints. These objective functions and constraints can be represented by the general response function F as

$$F(\boldsymbol{\varphi}) = G\left(\boldsymbol{u}(\boldsymbol{\varphi}), \boldsymbol{\varphi}\right) \tag{3.1.5}$$

Notice that the dependence of the response function F on the design vector $\boldsymbol{\varphi}$ is rewritten using the function G so as to isolate its implicit dependence on $\boldsymbol{\varphi}$ through $\boldsymbol{u}(\boldsymbol{\varphi})$ from the explicit dependence on $\boldsymbol{\varphi}$.

Gradient-based optimization schemes require the derivatives of the response functions with respect to the design variable, which can be computed from (3.1.5) as

$$\frac{DF}{D\varphi_i} = \frac{\partial G}{\partial \boldsymbol{u}} \cdot \frac{D\boldsymbol{u}}{D\varphi_i} + \frac{\partial G}{\partial \varphi_i}. \tag{3.1.6}$$

In the above equation, the derivatives $\partial G/\partial \boldsymbol{u}$ and $\partial G/\partial \varphi_i$ are explicit quantities, whereas the derivative $D\boldsymbol{u}/D\varphi_i$ is an implicit quantity because the system response is implicitly defined through equation (3.1.4).

In the direct differentiation approach, the implicit derivative $D\boldsymbol{u}/D\varphi_i$ is evaluated and then the sensitivities are obtained from equation (3.1.6). This is accomplished by differentiating equation (3.1.4) with respect to the individual design parameters φ_i, which, after some rearranging, yields

$$\frac{\partial \tilde{\boldsymbol{R}}_U}{\partial \boldsymbol{u}} \frac{D\boldsymbol{u}}{D\varphi_i} = -\frac{\partial \tilde{\boldsymbol{R}}_U}{\partial \varphi_i}. \tag{3.1.7}$$

The above equation forms a pseudo-problem for the evaluation of the response sensitivity $D\boldsymbol{u}/D\varphi_i$ resulting from the pseudo-load $-D\tilde{\boldsymbol{R}}_U / D\varphi_i$, Note here that the

operator in the pseudo-problem is identical to the tangent operator in the Newton-Raphson analysis of the primal problem (2.3.18). In a finite element analysis, this reappearance of the tangent operator allows the decomposed tangent stiffness matrix resulting from the iterative solution of $\boldsymbol{u}$ to be used to solve equation (3.1.7) efficiently for the implicit response sensitivity $D\boldsymbol{u}/D\varphi_i$. Hence, the evaluation of the derivative $D\boldsymbol{u}/D\varphi_i$ requires only the formation of the pseudo-load vector $-\partial\tilde{\boldsymbol{R}}_U/\partial\varphi_i$.

Adjoint sensitivities are obtained via the Lagrange multiplier method, where the implicit response sensitivity $D\boldsymbol{u}/D\varphi_i$ is eliminated from equation (3.1.6). Equations (3.1.4) and (3.1.5) are combined to define the augmented functional

$$\hat{F}(\boldsymbol{\varphi}) \equiv G\left(\boldsymbol{u}(\boldsymbol{\varphi}),\boldsymbol{\varphi}\right) - \boldsymbol{\lambda}_U(\boldsymbol{\varphi}) \cdot \tilde{\boldsymbol{R}}_U\left(\boldsymbol{u}(\boldsymbol{\varphi}),\boldsymbol{\varphi}\right) \tag{3.1.8}$$

where $\boldsymbol{\lambda}_U(\boldsymbol{\varphi})$ is the Lagrange multiplier and $\boldsymbol{u}$ is a solution to equation(3.1.9). Note here that $\hat{F} = F$ since $\tilde{\boldsymbol{R}}_U = \boldsymbol{0}$ from equation (3.1.4). Differentiation of the above with respect to the individual design parameters φ_i yields

$$\frac{D\hat{F}}{D\varphi_i} = \frac{\partial G}{\partial \boldsymbol{u}} \cdot \frac{D\boldsymbol{u}}{D\varphi_i} + \frac{\partial G}{\partial \varphi_i} - \frac{D\boldsymbol{\lambda}_U}{D\varphi_i} \cdot \tilde{\boldsymbol{R}}_U - \boldsymbol{\lambda} \cdot \left(\frac{\partial \tilde{\boldsymbol{R}}_U}{\partial \boldsymbol{u}} \frac{D\boldsymbol{u}}{D\varphi_i} + \frac{\partial \tilde{\boldsymbol{R}}_U}{\partial \varphi_i} \right) \tag{3.1.10}$$

Here, I note again that $D\hat{F}/D\varphi_i = DF/D\varphi_i$ since again $\tilde{\boldsymbol{R}}_U = \boldsymbol{0}$.

To isolate the implicit response sensitivities, I separate equation (3.1.10) into two terms

$$\frac{D\hat{F}}{D\varphi_i} = \frac{D\hat{F}_E}{D\varphi_i} + \frac{D\hat{F}_I}{D\varphi_i} \tag{3.1.11}$$

where $D\hat{F}_E / D\varphi_i$ and $D\hat{F}_I / D\varphi_i$ are the explicit and implicit terms, respectively, defined as

$$\frac{D\hat{F}_E}{D\varphi_i} = \frac{\partial G}{\partial \varphi_i} - \boldsymbol{\lambda}_U \cdot \frac{\partial \tilde{\boldsymbol{R}}_U}{\partial \varphi_i} \tag{3.1.12}$$

$$\frac{D\hat{F}_I}{D\varphi_i} = \frac{D\boldsymbol{u}}{D\varphi_i} \cdot \left[\frac{\partial G}{\partial \boldsymbol{u}} - \left(\frac{\partial \tilde{\boldsymbol{R}}_U}{\partial \boldsymbol{u}} \right)^T \boldsymbol{\lambda}_U \right] \tag{3.1.13}$$

The implicit part $D\hat{F}_I / D\varphi_i$ is eliminated from the sensitivity expression by defining the Lagrange multiplier $\boldsymbol{\lambda}_U$, so that equation (3.1.13) equals zero. Once this $\boldsymbol{\lambda}_U$ is determined, the unknown derivative $D\boldsymbol{u}/D\varphi_i$ is eliminated from the sensitivity expression and the sensitivities are evaluated from the remaining explicit quantity (i.e. equation(3.1.12)). Annihilation of the implicit term in equation (3.1.13) yields the following adjoint problem for the adjoint response Lagrange multiplier $\boldsymbol{\lambda}_U$.

$$\left(\frac{\partial \tilde{\boldsymbol{R}}_U}{\partial \boldsymbol{u}} \right)^T \boldsymbol{\lambda}_U = \frac{\partial G}{\partial \boldsymbol{u}} \tag{3.1.14}$$

where $\partial G/\partial \boldsymbol{u}$ is deemed the adjoint load. Once the adjoint response $\boldsymbol{\lambda}_U$ is evaluated, the sensitivity expression reduces to

$$\frac{D\hat{F}}{D\varphi_i} = \frac{\partial G}{\partial \varphi_i} - \boldsymbol{\lambda}_U \cdot \frac{\partial \tilde{\boldsymbol{R}}_U}{\partial \varphi_i} . \tag{3.1.15}$$

Here, I note that the operator that appears in the adjoint problem is the transpose of the Newton-Raphson tangent operator used to obtain $\delta\boldsymbol{u}$.

The adjoint method requires the solution of one adjoint problem for each response function *F*, whereby the sensitivity is computed from equation (3.1.15). Therefore, it is very efficient when the number of response functions is small compared with the number of design parameters. If this ratio is reversed, the direct differentiation is generally preferred [114].

3.3. Numerical issues

This section presents a topology optimization example problem of Navier-Stokes flow systems and discusses numerical instabilities in the optimization process which are not presented in previous studies of topology optimization for Stokes flow systems [45-46, 51, 100-102]. To clarify the cause of these instabilities, adjoint sensitivities are first compared to finite difference sensitivities, and then the effect of numerical issues in the system analysis, which is discussed in section 2.5.2, is confirmed. To circumvent these numerical instabilities, filtering methods, such as the density filter and the sensitivity filter [35, 115-117], are evaluated and a move-limit approach is suggested.

3.3.1. Design examples

As an example problem, the minimization of kinetic energy dissipation is solved for a Navier-Stokes flow system with a volume constraint; these objective and constraint have been examined in previous topology optimization studies of Stokes flow system [50, 118-119]. The design domain and boundary conditions are shown in Figure 3.3.1. The inlet fluid velocity U is determined by pre-assigned Reynolds numbers ReH. Then, this optimization problem can be stated as

Minimize $$F_1(\varphi) = \frac{1}{2}\left(\nabla \boldsymbol{v}, \mu_f \nabla \boldsymbol{v}\right) + \left(\boldsymbol{v}, \alpha(\varphi)\boldsymbol{v}\right) \tag{3.2.1}$$

Subject to $$\rho_f \boldsymbol{v}\cdot\nabla\boldsymbol{v} - \mu_f \nabla^2 \boldsymbol{v} + \alpha(\varphi)\boldsymbol{v} + \nabla p = \boldsymbol{f} \tag{3.2.2}$$

$$\int_\Omega \varphi \, d\Omega - V_{\min} \geq 0 \tag{3.2.3}$$

$$\varphi_{\min} \leq \varphi \leq 1 \tag{3.2.4}$$

where F is the objective function and $V_{\min}$ is the minimum amount of solid volume in the design domain. Several values of α_s are tested from 10^4 to 10^{16}, and the value of $\varphi_{\min}$ is set to 0. The volume constraint is set at 10% solid volume in the design domain as

$$V_{\min} = 0.1 \times \int_\Omega 1 \, d\Omega . \tag{3.2.5}$$

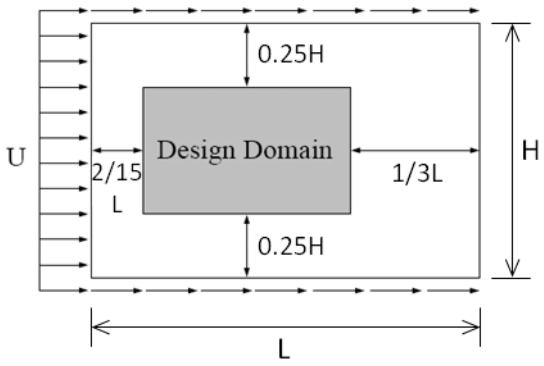

(a)

Reynolds number	ReH = 0.001, 10, 100, 1000
Domain size	L×H = 1.5×1
Mesh	240×160, 480×320
Shape function (***v***, *p*, *T*)	Q4Q4
Stabilization method	GLS
Brinkman penalization	$\alpha_s = 10^4$-10^{16}

(b)

Optimizer	SLP, MMA
Shape function (φ)	Q4, U1
Interpolation function	RAMP
Filtering method	density filter, sensitivity filter

(c)

Figure 3.3.1 [P6] 2D design example (a) design domain and boundary conditions (b) analysis setup (c) optimization setup

The optimization problem is solved by using the MMA and SLP algorithm. For the design sensitivity, the adjoint sensitivity method is used and verified with finite difference sensitivity. Figure 3.3.2 shows the sensitivity analysis result at the initial design condition, $\varphi = 0.1$. The two sensitivity analysis results are well matched with each other.

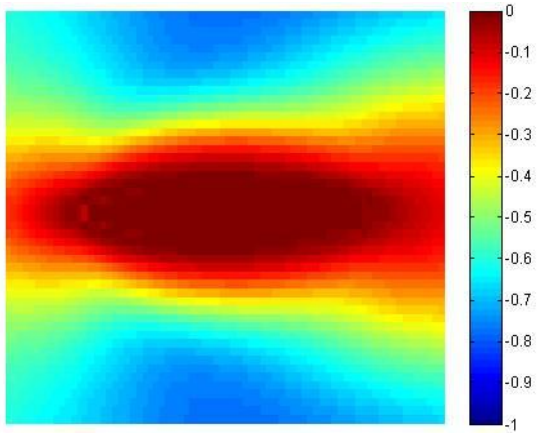

(a)

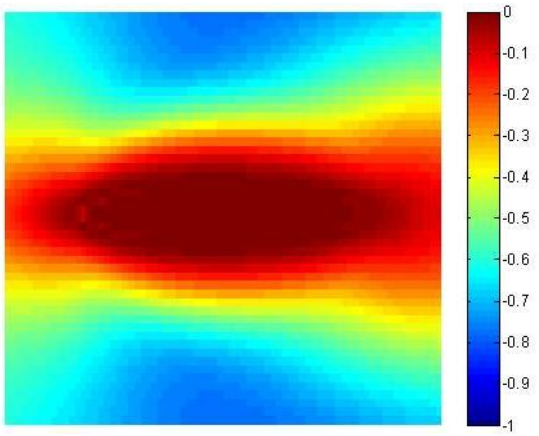

(b)

Figure 3.3.2 [P6] Design sensitivity result: (a) finite difference sensitivity
(b) adjoint sensitivity

3.3.2. Creeping flow, ReH=0.001

At first, to verify topology optimization method, the design result for creeping flow is first solved and compared to the analytical solution calculated by Pironneau [121] and previous topology optimization results obtained by Borrvall and Petersson [5]. The Reynolds number is set to 0.001 to simulate creeping flow. α_s and $\varphi_{\min}$ are set to 10^8 and zero, respectively. Figure 3.3.3 shows the optimization steps. According to Pironneau's analytical solution [121], the wedge of angle should be 90^o to minimize drag in the creeping flow. The shape of obstacle body obtained satisfies the analytical solution as shown in Figure 3.3.4, and also corresponds to the previous topology optimization result of a Stokes flow system [5]. In addition, Figure 3.3.5 and Figure 3.3.6 show that the objective and the design converge well to the optimized design. The functions C and S given by equation (3.2.6) and (3.2.7) show the 0-1 convergence and the convergence of design shape respectively.

$$C = \sum_i^N \left(\varphi_i - \varphi_{\min}\right) \times \left(\varphi_{\max} - \varphi_i\right) \Big/ N \tag{3.2.6}$$

$$S = \sum_i^N \left|\varphi_i^{I+1} - \varphi_i^I\right| \Big/ N \tag{3.2.7}$$

Here, N is total number of the design variables.

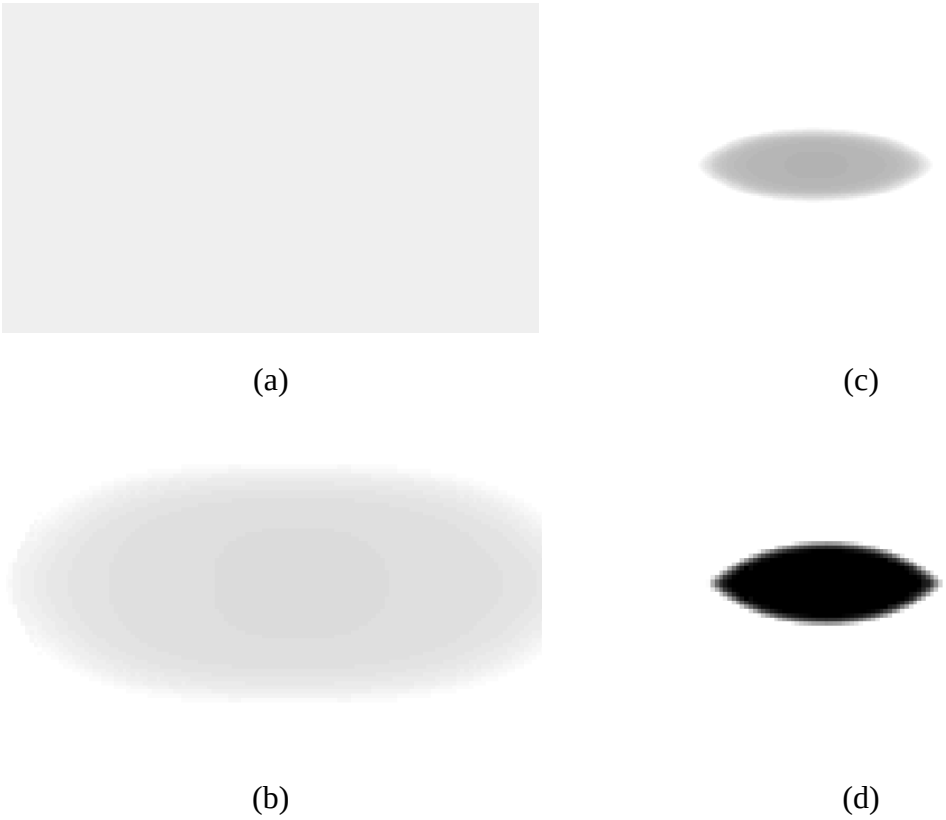

Figure 3.3.3 [P6] Design process, ReH=0.001 (a) initial design (b) 5st step (c) 10th step (d) 50th step

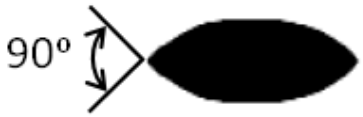

Figure 3.3.4 [P6] Optimization result, ReH=0.001

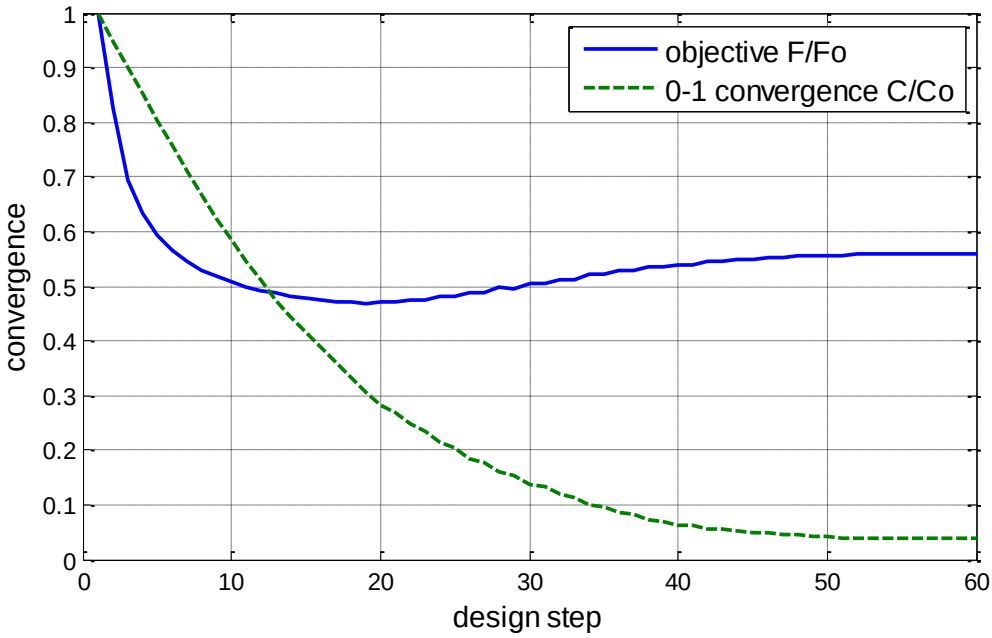

Figure 3.3.5 [P6] Convergence history, ReH=0.001

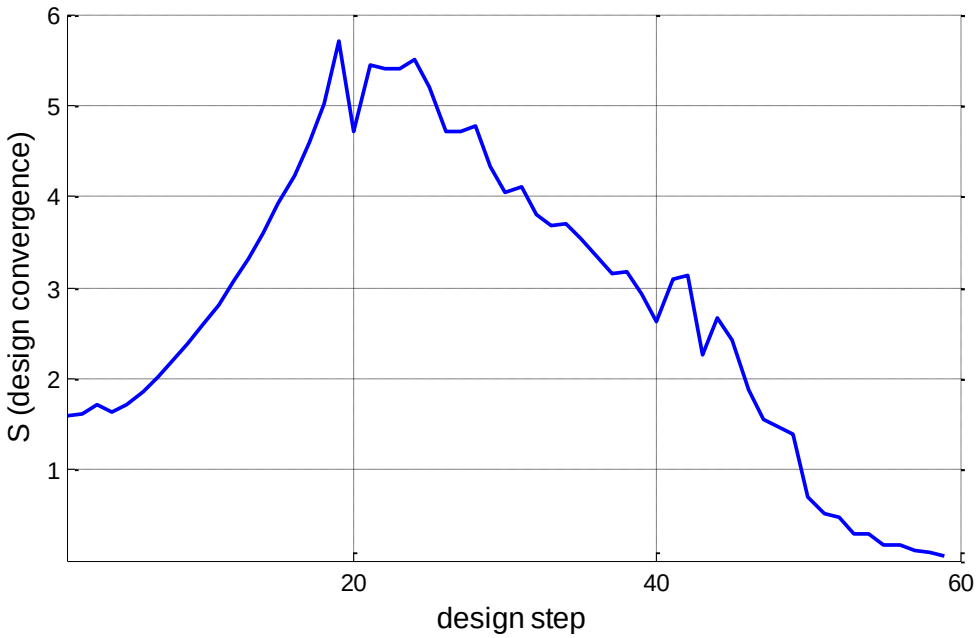

Figure 3.3.6 [P6] Design convergence history, ReH=0.001

3.3.3. Fluctuation at the boundaries

Now the same optimization problem shown in section 3.3.1 is tested with a higher Reynolds number. ReH is set to 100 with the same volume constraint 0.1. α_s and φ_{min} are again set to 10^6 and zero, respectively. Either MMA or SLP algorithm is used as an optimizer. Figure 3.3.7 shows the design history. At the initial stage, the design converges very well as shown in Figure 3.3.7(a)-(d) before solid elements and void (free-fluid) elements are first adjacent. From this point, the design starts fluctuating at the solid-fluid interfaces and generates element-scale cavities as shown in Figure 3.3.7(e)-(h). As a result, the design no longer converges as shown in Figure 3.3.8 and Figure 3.3.9. It is noted that this numerical instability typically occurs when a large penalization term is used or when a high Reynolds number flow is solved.

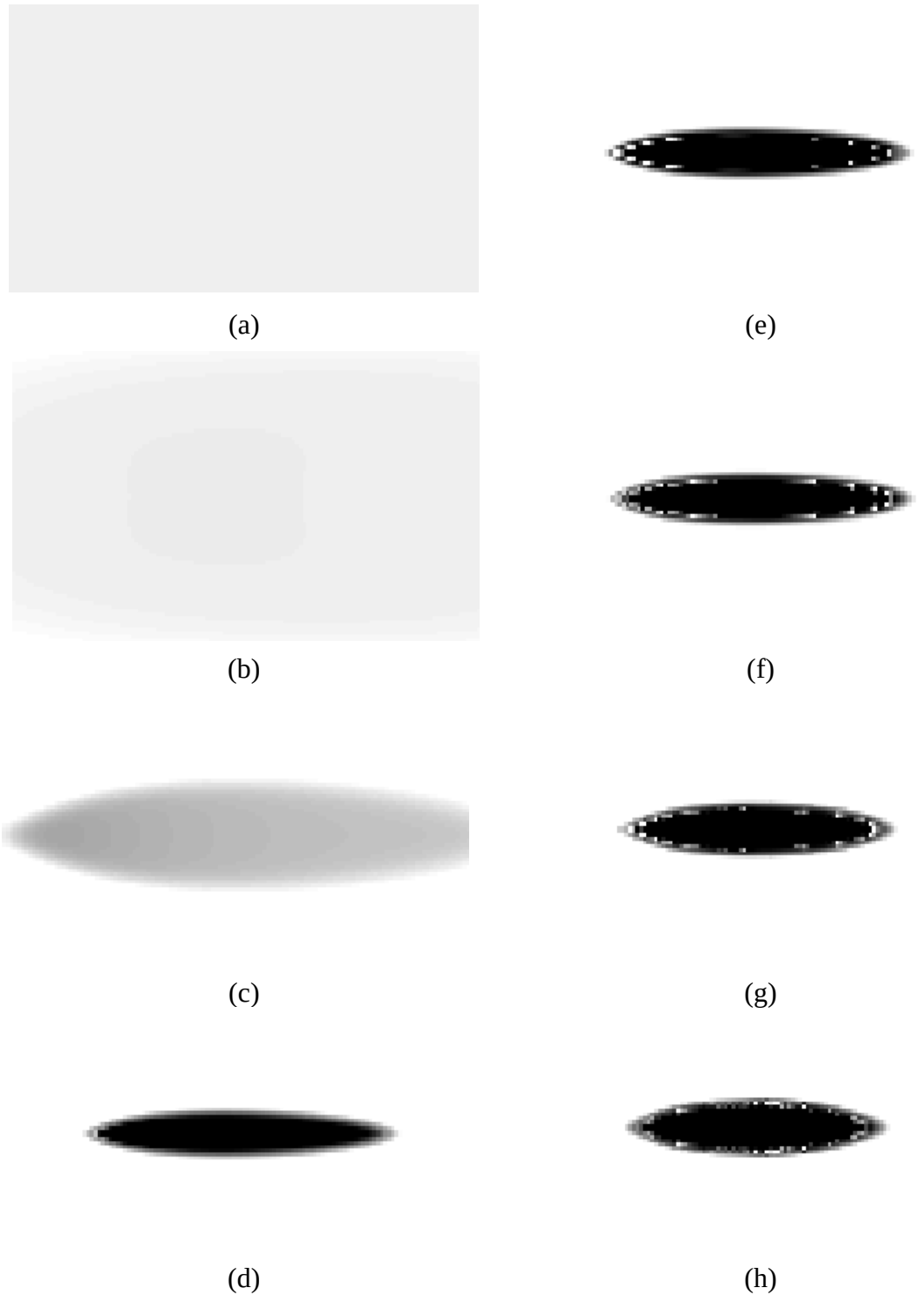

Figure 3.3.7 [P6] Design process, ReH=100 (a) initial design (b) 1st step (c) 10th step (d) 18th step (e) 19th step (f) 20th step (g) 25th step (h) 30th step

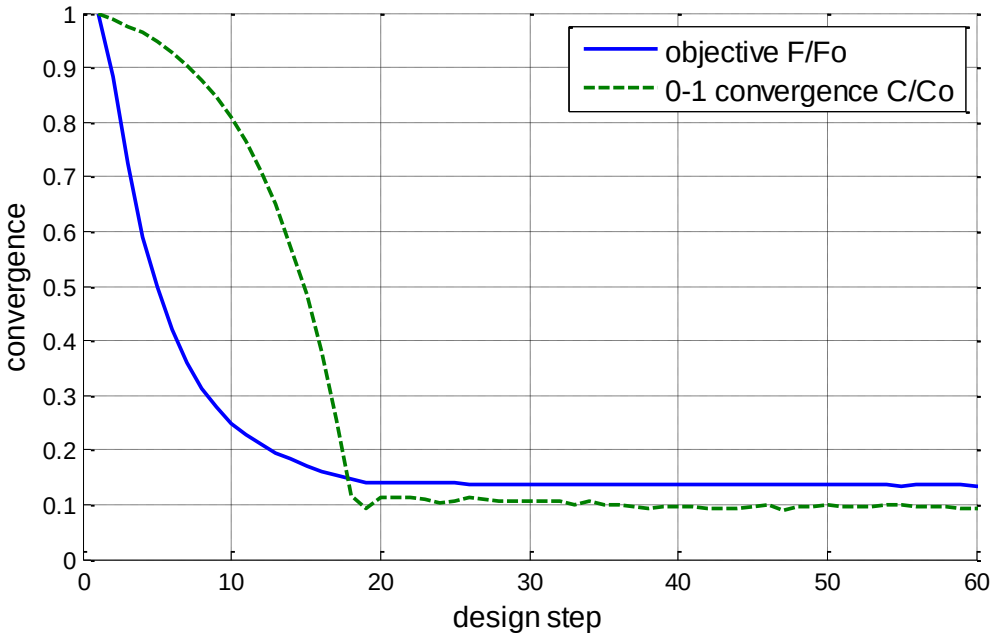

Figure 3.3.8 [P6] Convergence histories, ReH=100

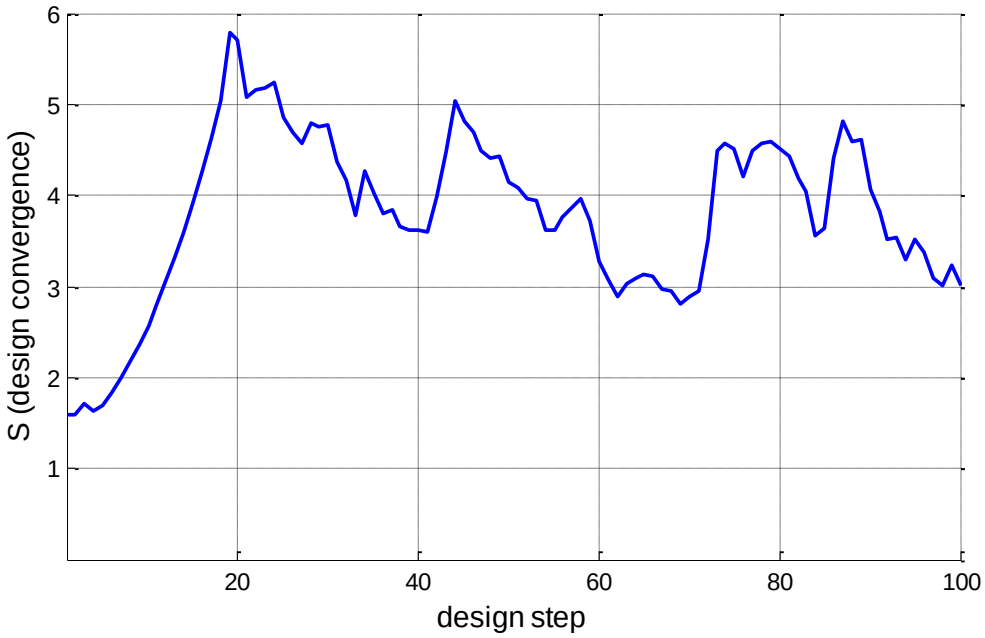

Figure 3.3.9 [P6] Design convergence history, ReH=100

Generally speaking, there are three possible problems that cause this numerical issue preventing design convergence: (1) errors in the sensitivity analysis, (2) errors in the optimizer and (3) errors in the system analysis. To clarify the reason for these boundary oscillations and cavities, the adjoint sensitivity values at the optimization step when design oscillation arises, and where cavities first appear, are first compared with the finite difference sensitivity values in order to verify the adjoint sensitivity calculation. Figure 3.3.10 shows that the two sensitivity results correspond to each other, which demonstrates that there is no error in the sensitivity analysis.

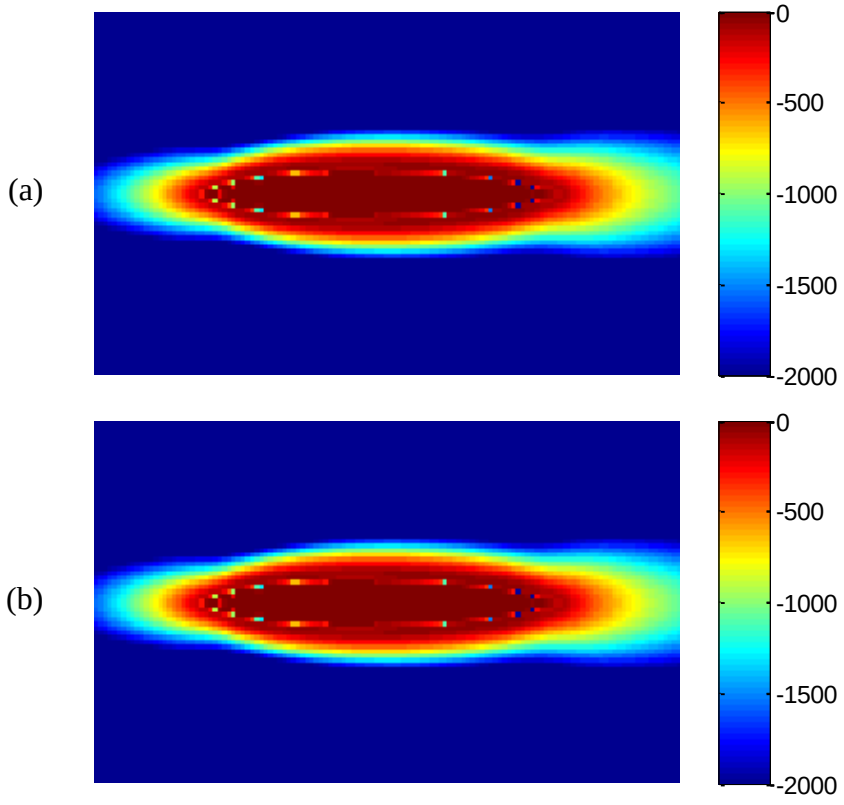

Figure 3.3.10 [P6] Design sensitivity results at 18th step, ReH=100 (a) adjoint sensitivity (b) finite difference sensitivity

Second, the correlation between the sensitivity result and the next design at the local area is investigated. Many negative sensitivity peaks shown in Figure 3.3.11, (blue dots in the 18th sensitivity graph), make the optimizer to decrease solid density at those points; therefore, the problematic element-scale cavities of the next 19th design are generated at the same points. This means that the design result corresponds with the sensitivity result and consequently, the SLP works properly.

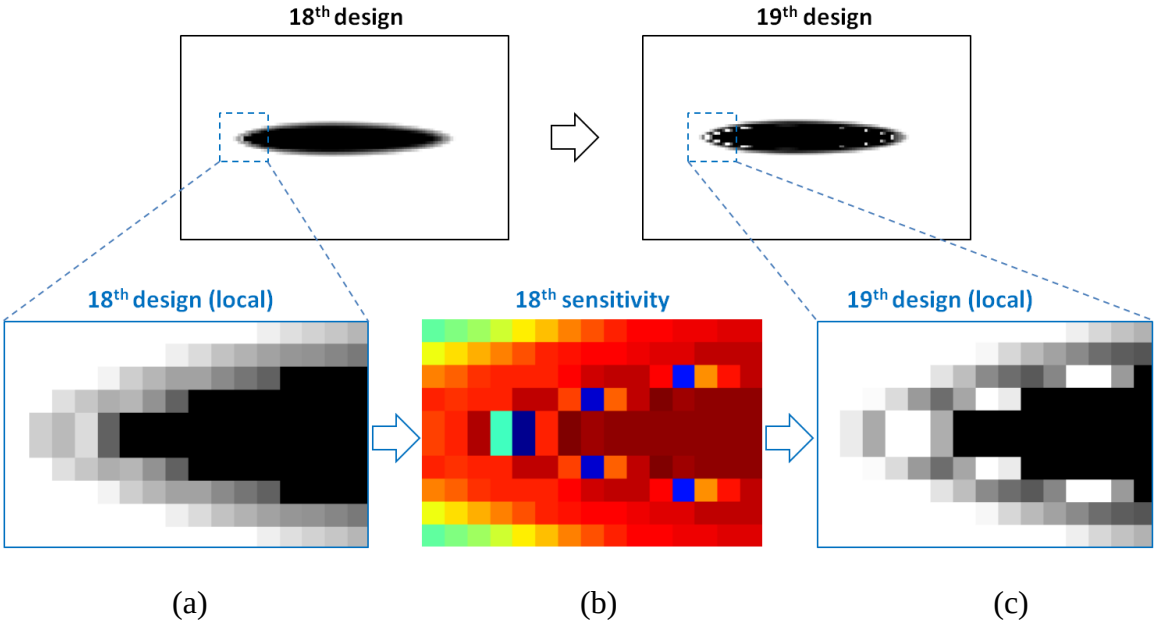

Figure 3.3.11 [P6] Local sensitivity result and design history, ReH=100 (a) 18th design (b) 18th sensitivity (c) 19th design

Finally the system analysis results are inspected once again. In section 2.5, oscillations in the numerical solution are observed near solid-fluid interfaces (immersed boundaries). Likewise, huge oscillations of velocity and pressure are found in the 18th analysis result, as shown in Figure 3.3.12. The oscillations arise mainly at corner points of pure-solid

regions (φ=1) because the finite element solution hardly capture the sharp gradient changes. As a result, huge back pressure and following forward pressure are produced throughout the element-scale areas. These back pressures increase the value of the objective function; therefore, the sensitivity results have negative values in order to remove the obstructing elements and consequently, to eliminate the back pressure. Figure 3.3.13 clearly shows the sensitivity oscillations.

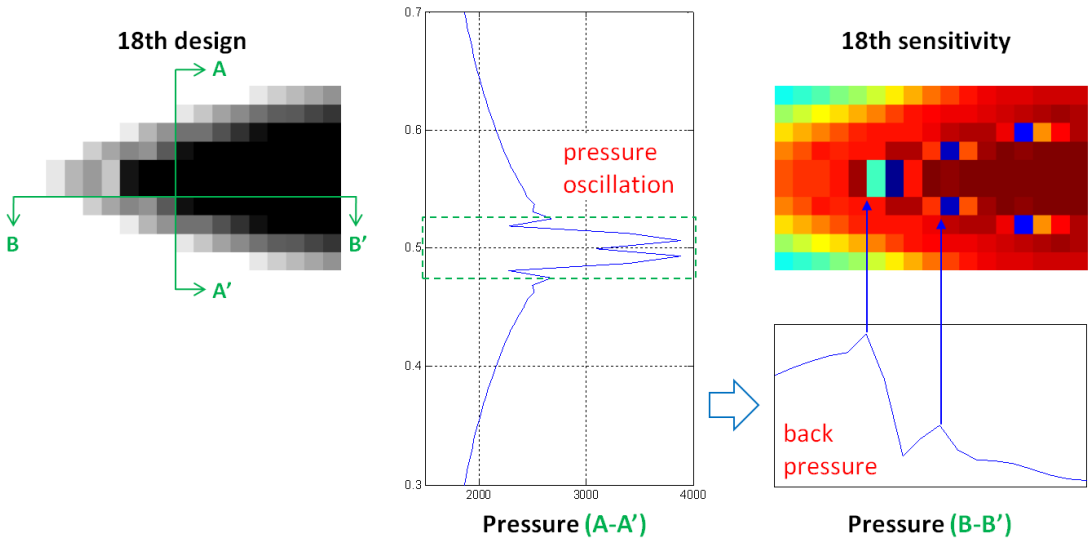

(a) (b) (c)

Figure 3.3.12 [P6] Local design and pressure oscillations, ReH=100 (a) 18th design (b) pressure oscillation at section A-A′ (c) back pressure gradients at section B-B′

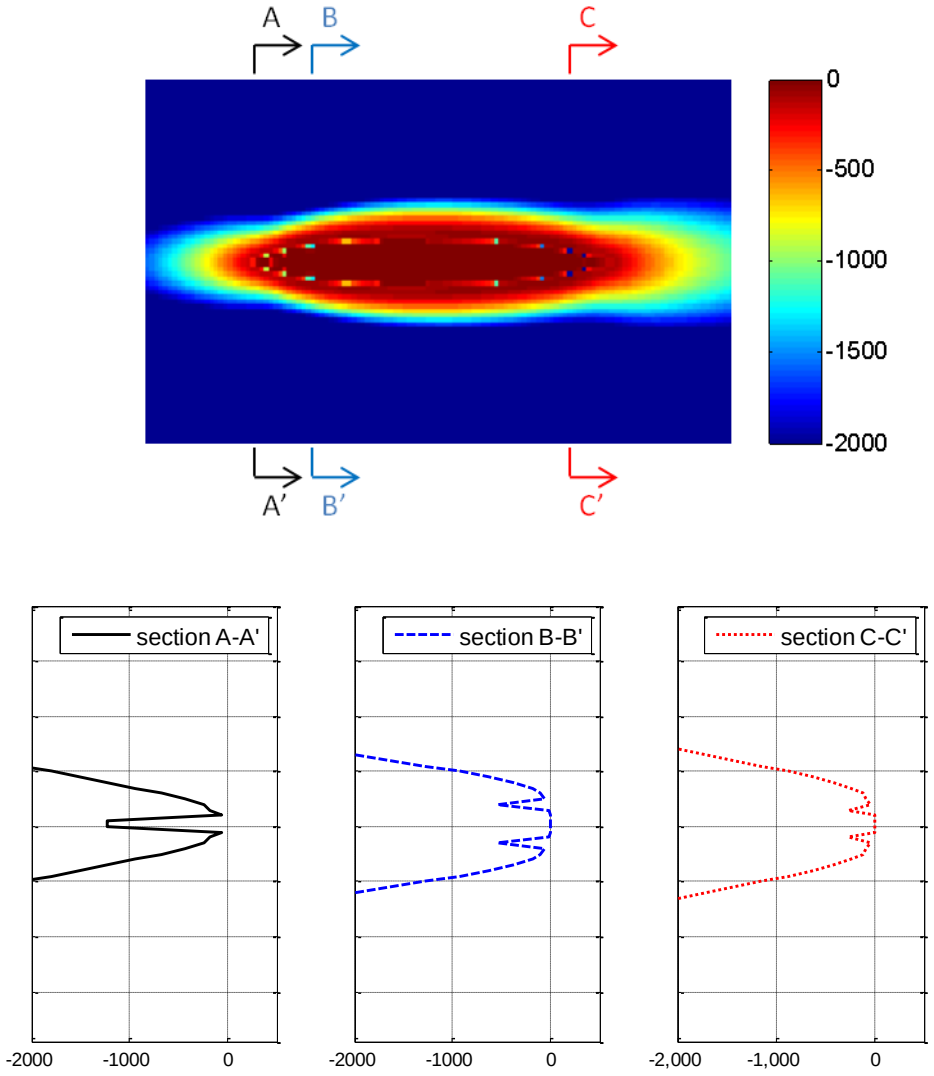

Figure 3.3.13 Sensitivity oscillations at (a) section A-A′ (b) section B-B′ (c) section C-C′

In conclusion, these numerical difficulties encountered during the topology optimization of Navier-Stokes flow systems are inherited from the numerical instabilities of the Brinkman penalization method. Although the instabilities are not problematic in the system analysis itself, they are amplified through the optimization process and

become a critical issue. As discussed in 2.5.2, these oscillations are not successfully suppressed at the level of system analysis – for example, by a change of stabilization method or mesh refinement. Therefore, different approaches are needed at the level of design optimization.

3.3.4. Filtering method approach

As a first approach, the effect of filtering methods, such as the density filter and the sensitivity filter, are tested to evaluate the possibility of suppressing this element-scale oscillation. These filtering methods, based on filtering techniques from image processing, were suggested by Sigmund to prevent the creation of element-scale checkerboards in numerical solutions to topology optimization problems [35]. Although these filtering methods are based on heuristics, their implementation, in many cases, effectively prevents checkerboard patterns and enables mesh-independent design. Furthermore, these filtering schemes are very easy to implement and they require no extra constraints in the optimization problem.

In the density filtering method, the element or node densities are modified by the following equation

$$\rho * K(\boldsymbol{r}) = \frac{1}{\langle K \rangle} \int_{\Omega} \rho\left(\boldsymbol{r} - \boldsymbol{r}'\right) K(\boldsymbol{r})\, d\Omega$$
$$K(\boldsymbol{r}) = \begin{cases} 1 - \dfrac{\| \boldsymbol{r} \|}{d_{filter}} & if \ \| \boldsymbol{r} \| \le d_{filter} \\ 0 & \text{otherwise} \end{cases} \tag{3.2.8}$$

where $\tilde{\rho}_e$ is the modified density and N_e is the set of neighboring density variables. As the density filter smoothes the density distribution, the density convergence is poor when coarse mesh is adapted. Therefore, reasonably fine mesh should be selected. In addition to the convergence problem, it should be mentioned that the material volume is not preserved after the filtering operation unless the periodic boundary condition is used.

In the sensitivity filtering method, the design sensitivities are modified by the following equation

$$\frac{\partial F^*}{\partial \rho_k} = \frac{1}{\rho_k \sum_{i=1}^{N} H_i} \sum_{i=1}^{N} H_i \rho_i \frac{\partial F}{\partial \rho_i} \qquad (3.2.9)$$
$$H_i = d_{filter} - \mathrm{dist}(k,i)$$

As stated in [122], this heuristic modification of the design sensitivity may be questioned due to the fact that the filtered sensitivities differ from the original design sensitivity of the objective function. Despite this argument, the sensitivity filtering method has succeeded in many applications. As suggested in [122], ρ_e in the denominator should be larger than a small value of ε (e.g., 10^{-3}). Otherwise, the sensitivity filtering method (e.g., $\varepsilon=10^{-6}$) will create large sensitivity at the low density region.

Figure 3.3.14 and Figure 3.3.15 show design histories when these filtering schemes are implemented to the topology optimization of the Navier-Stokes flow system. The density filter eliminates one-element cavities inside solid structures by smoothing the

values of sharp 0-1 interfaces and, as the result, the element-scale oscillations are suppressed as expected. However, this method does not completely resolve the overall convergence issue because larger-scale oscillations, although they are blurry, still occur during the optimization process disturbing convergence, as shown in Figure 3.3.14. Sensitivity filter does not prevent the element-scale oscillation; rather it aggravates the convergence problems, as shown in Figure 3.3.15. Figure 3.3.16 and Figure 3.3.17 show the design results are not converged.

Despite their successful performance in preventing the checkerboard issue, these filtering methods are not successful in preventing the boundary oscillation. This is mainly because there are two significant differences between the typical checkerboard patterns and the boundary oscillations. First, in the checkerboard patterns, the locations of void and solid elements do not move at the final stage of convergence whereas the locations of void elements (cavities in the solid structures) constantly move at each design step. Second, due to the large value of the penalization parameter, the gradient of sensitivity oscillation is generally much larger than the sensitivity gradients in checkerboard patterns. Therefore, it is more difficult to smooth out sensitivity peaks by using the same sensitivity filter method. In conclusion, the filtering methods are inappropriate to prevent this numerical issue although they assure mesh-independent design solutions.

Figure 3.3.14 Design history with the densitivy filter (a) 20th step (b) 43rd step (c) 44th step (d) 45th step

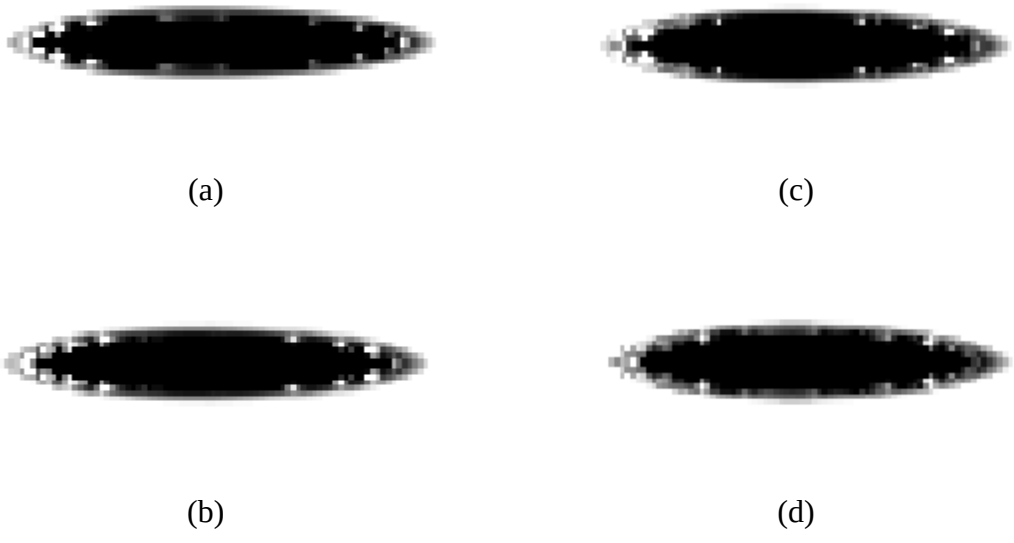

Figure 3.3.15 Design history with the sensitivity filter (a) 19th step (b) 20th step (c) 21st step (d) 22nd step

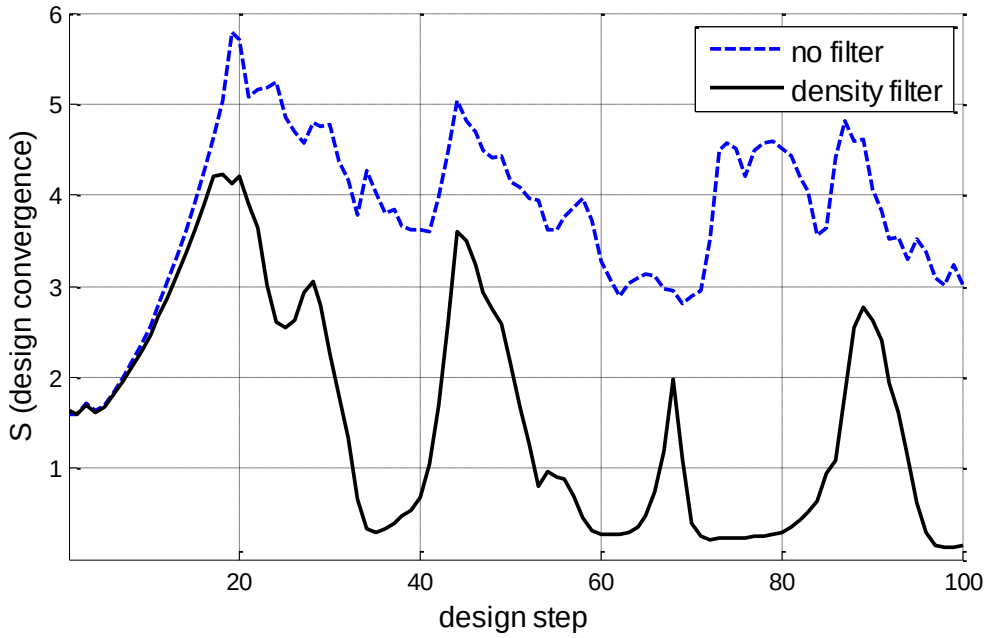

(a)

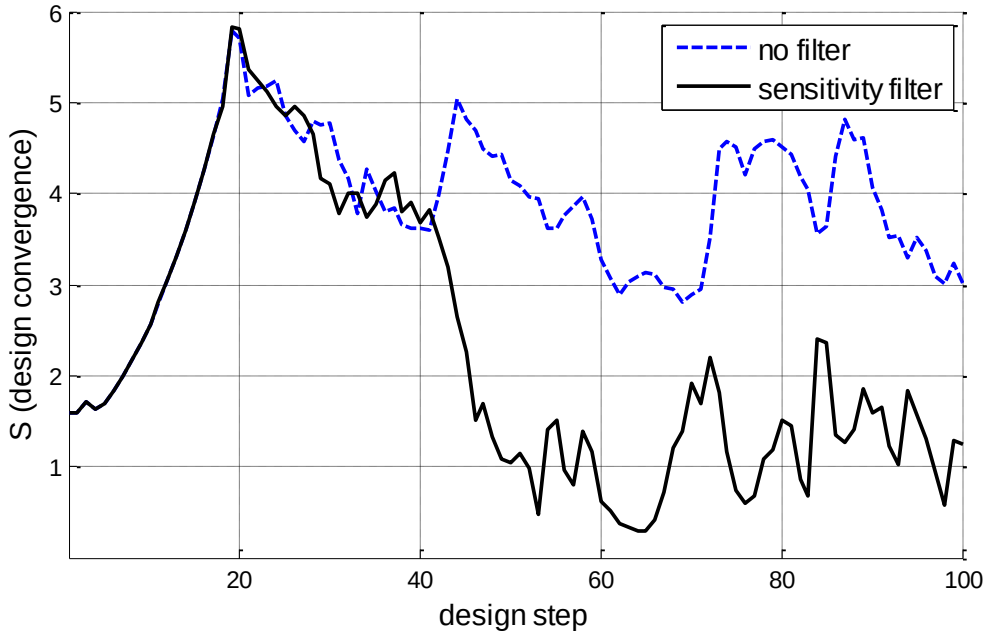

(b)

Figure 3.3.16 [P6] Design convergence histories with filters, ReH=100 (a) the density filter, (b) the sensitivity filter

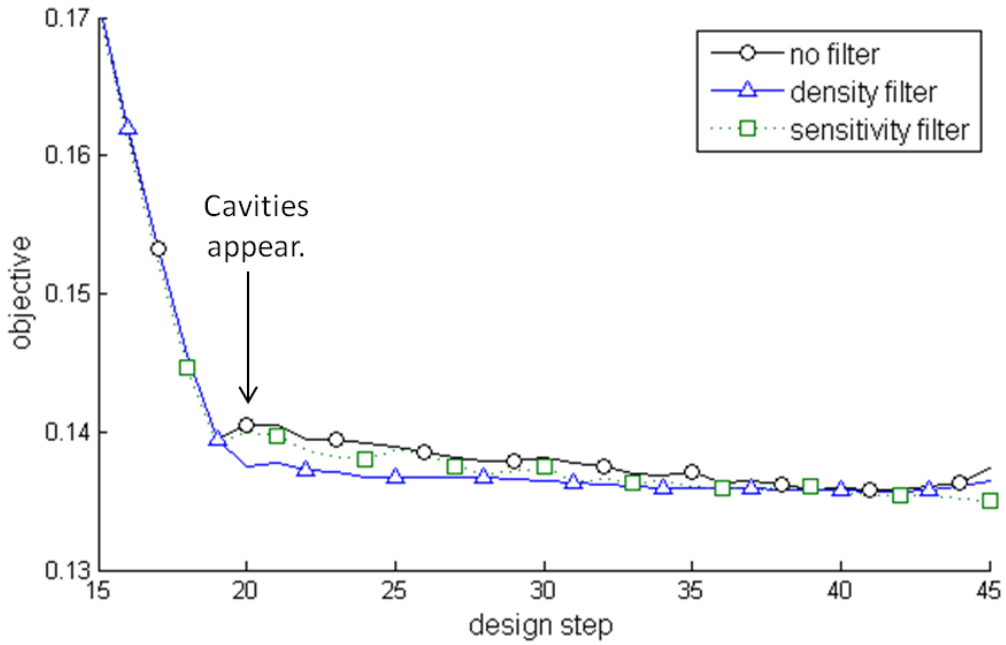

Figure 3.3.17 Objective convergence histories according to filtering schemes

3.3.5. Move-limit approach

My second approach to solve the numerical issues is to test the effect of move-limit on the boundary oscillations. Based on the fact that the void cavities near the solid-fluid interfaces are constantly appearing and disappearing at different locations, I set a maximum move-limit to the design variables to prevent such sudden changes. For the SLP optimizer, this move-limit is easily implemented with basic constraints. For the MMA optimizer, the move-limit can be implemented by a filter given by equation (3.2.10)

$$\varphi^{i+1} = \begin{cases} \max\left(\varphi_{\min},\, \varphi^i - c\right) & \text{if} \quad \varphi^{i+1} \le \varphi^i - c \\ \min\left(\varphi^i + c,\, 1\right) & \text{if} \quad \varphi^i + c \le \varphi^{i+1} \\ \varphi^{i+1} & \text{otherwise} \end{cases} \tag{3.2.10}$$

Figure 3.3.18 and Figure 3.3.19 show the design history without or with the move-limit constraint, respectively. A 5% move-limit is applied in the previous problem. The element-scale void-holes and resulting boundary oscillation is successfully suppressed with the move-limit and consequently, the design converges well although the objective does not change much, as shown in Figure 3.3.20 and Figure 3.3.21. Also, it should be mentioned that this move-limit scheme does not significantly decelerate the speed of the entire topology optimization of Navier-Stokes flow systems despite the need for more design steps. When solving the nonlinear Navier-Stokes equation for the J+1th design, the analysis result for the previous Jth design is generally used for the values of the initial guess. The more the two Jth and J+1th designs resemble each other, the easier it is to find a new solution. As a smaller move-limit is applied, the Jth design and J+1th design become more similar, and the number of required inner loop iterations for solving the nonlinear equation is reduced. Thus, although more outer loop design steps are needed, the fewer inner loop iterations needed for solving the nonlinear problem compensates for the time loss associated with the greater number of outer loop design step.

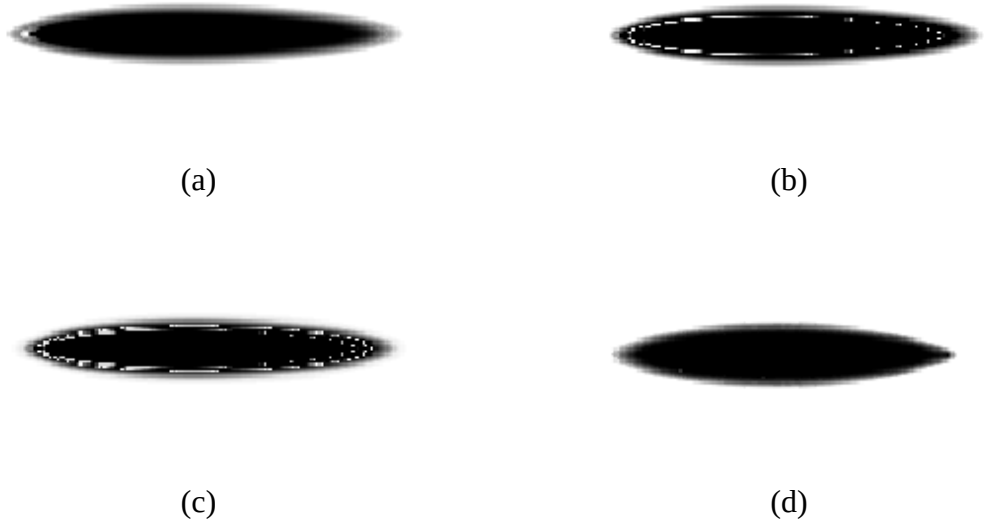

Figure 3.3.18 [P6] Design history without move-limit, ReH=100 (a) initial design (b) 1st step (c) 2nd step (d) 149th step

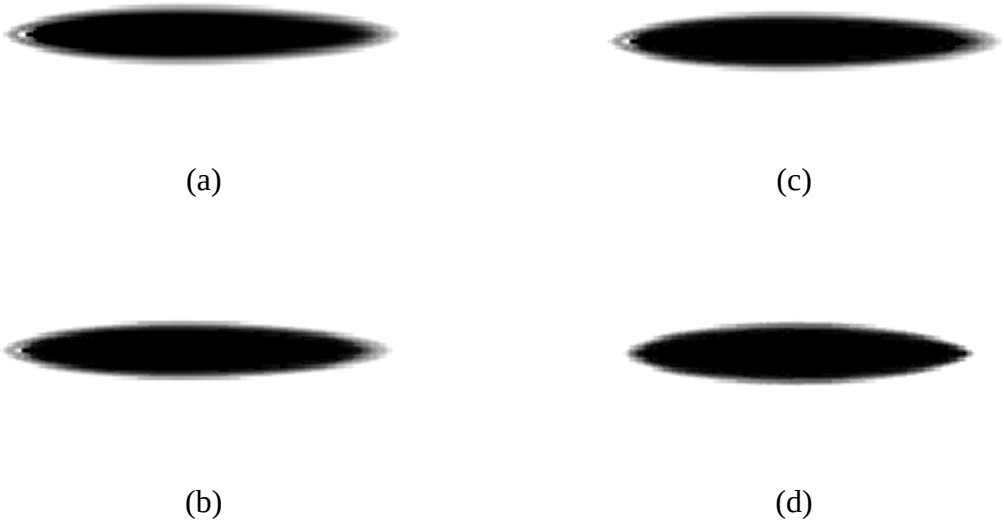

Figure 3.3.19 [P6] Design history with 5% move-limit, ReH=100 (a) initial design (b) 1st step (c) 2nd step (d) 31st step

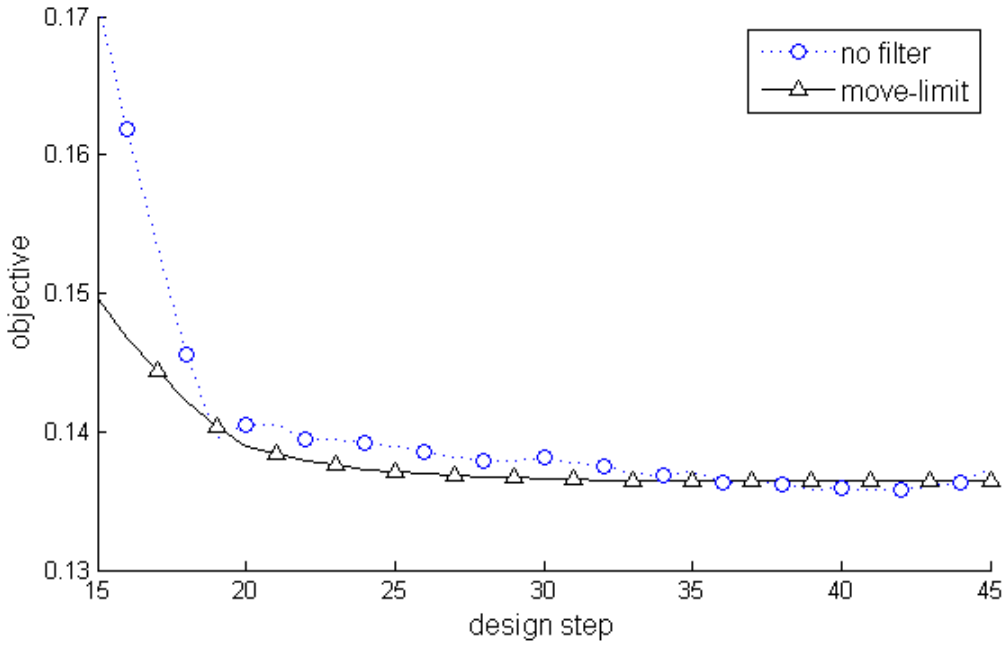

Figure 3.3.20 [P6] Objective convergence histories according to move-limit, ReH=100

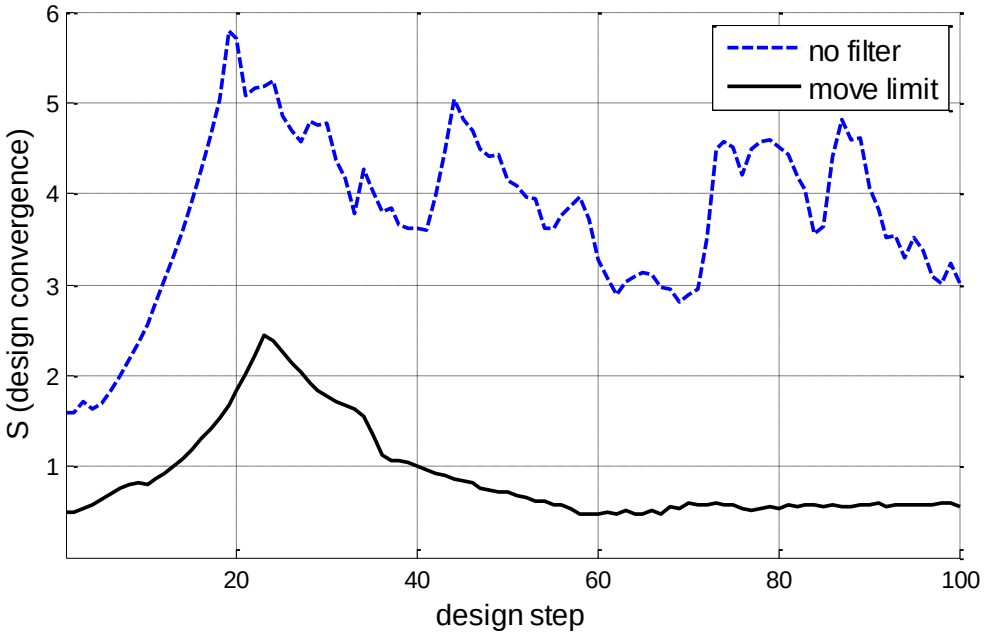

Figure 3.3.21 [P6] Design convergence history with 5% move limit, ReH=100

3.4. Design of Navier-Stokes flow systems

This section presents the topology optimization of Navier-Stokes flow systems. The objective function is the minimization of kinetic energy dissipation or drag force both with the volume constraint. 5% move limit is applied to prevent the boundary oscillations and consequent convergence issues. The density filter is also applied to obtain mesh-independent design solutions. Then, the effect of the Reynolds number change is discussed with the design results. The no-slip boundary condition at solid boundaries and the zero-velocity condition in solid structures are verified from the design results.

3.4.1. Minimization of kinetic energy dissipation

For the first design objective, the minimization of kinetic energy dissipation is solved for 2D and 3D Navier-Stokes flow systems with the volume constraint. The formal topology optimization problems can be given by

$$\text{Minimize} \qquad F_1(\varphi) = \frac{1}{2}\left(\nabla \mathbf{v}, \mu_f \nabla \mathbf{v}\right) + \left(\mathbf{v}, \alpha(\varphi)\mathbf{v}\right) \tag{3.3.1}$$

$$\text{Subject to} \qquad \rho_f \mathbf{v}\cdot\nabla\mathbf{v} - \mu_f \nabla^2 \mathbf{v} + \alpha(\varphi)\mathbf{v} + \nabla p = \boldsymbol{f} \tag{3.3.2}$$

$$\int_\Omega \varphi \, d\Omega - V_{\min} \geq 0 \tag{3.3.3}$$

$$\varphi_{\min} \leq \varphi \leq 1 \tag{3.3.4}$$

where F is the objective function.

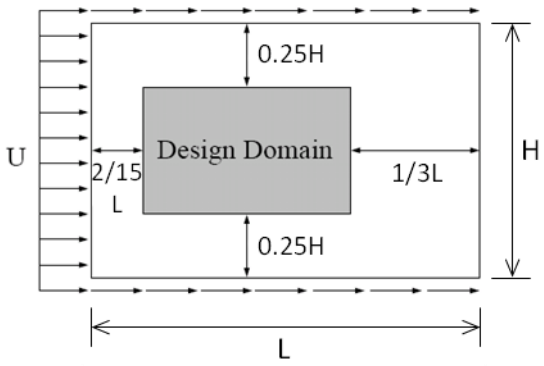

(a)

Reynolds number	ReH = 0.001, 10, 100, 1000
Domain size	L×H = 1.5×1
Mesh	240×160 480×320
Shape function (***v***, *p*, *T*)	Q4Q4
Stabilization method	GLS, SUPG+PSPG, SGS
Brinkman penalization	$\alpha_s = 10^6$

(b)

Optimizer	SLP, MMA
Shape function (φ)	Q4, U1
Interpolation function	RAMP
Filtering method	density filter, sensitivity filter
Additional constraint	move limit 5%

(c)

Figure 3.4.1 [P7] 2D design example (a) design domain and boundary conditions (b) analysis setup (c) optimization setup

(a)

(b)

(c)

Figure 3.4.2 [P7] Design results minimizing kinetic energy dissipation with GLS stabilization method a) ReH=10 b) ReH=100 c) ReH=1000

(a)

(b)

(c)

Figure 3.4.3 [P7] Design results minimizing kinetic energy dissipation at ReH=1000 with a) GLS stabilization method b) SUPG+PSPG stabilization method c) SGS stabilization method

Figure 3.4.1 shows a design domain and boundary conditions for a 2D Navier-Stokes flow system. To approximate the free-stream boundary condition with a higher Reynolds number flow along the right-side outflow boundary, a larger design domain is used than the one used for the creeping flow system in section 3.3. In the analysis, Q4Q4 elements with 240×160 square mesh are used; α_s is set to 10^6. In the optimization, the volume constraint V_{min} is set at 10% solid volume in the design domain; the value of φ_{min} is set to 0 and the SLP algorithm is used as an optimizer.

This optimization problem is solved with various flows of different Reynolds numbers. When the Reynolds number is small, as shown in Figure 3.4.2(a), the design solution is almost identical to the design solution of the creeping flow as shown in Figure 3.3.18(b). On the other hand, the optimized obstacle shape becomes thinner as the ReH increases, as shown in Figure 3.4.2(b), (c). With a faster flow stream, the flow resistance from a blunt obstacle body is more dominant than the flow resistance caused by skin friction; therefore, the obstacle body becomes thinner and more stream-lined to minimize total flow resistance and consequently, to minimize kinetic energy dissipation. In conclusion, these design results, shown in Figure 3.4.2, follow the general principle of fluid dynamics. There exists no significant difference when different stabilization methods are used as shown in Figure 3.4.3. The no-slip condition along the solid boundary and the zero-velocity condition inside the solid structure are satisfied, as shown in the velocity field graph Figure 3.4.4.

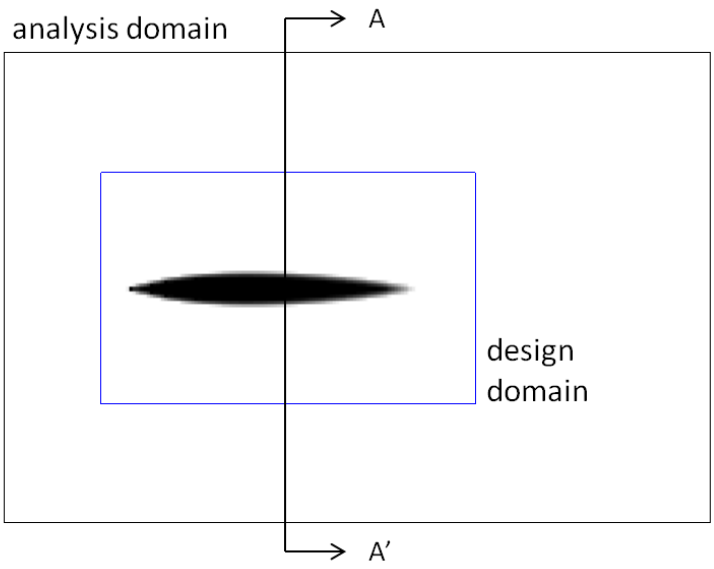

(a)

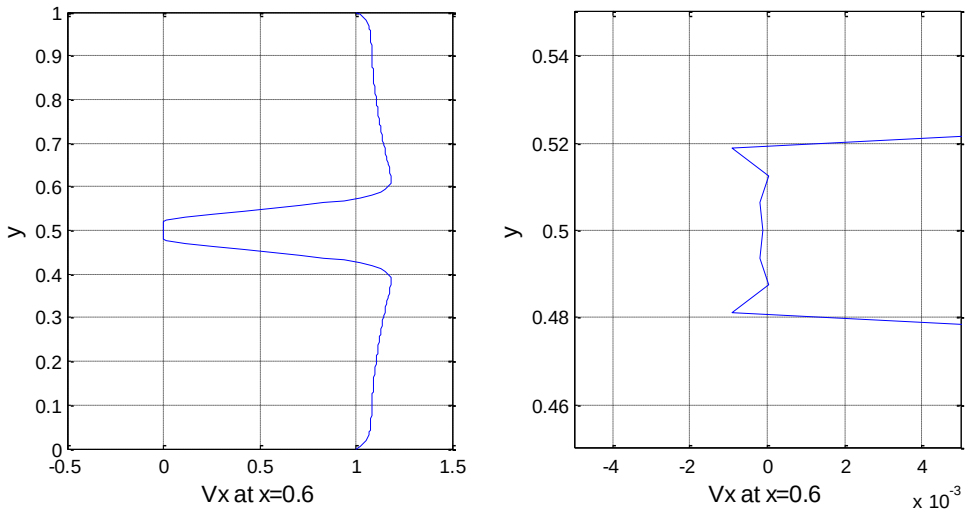

(b) (c)

Figure 3.4.4 [P7] Design result and velotiy profiles at ReH=1000 (a) design result (b) global velocity at section A-A' (c) local velocity view

Finally, a 3D flow channel is designed following Aage's study [51]. The design domain and boundary conditions are shown in Figure 3.4.5. The Reynolds number is 100. In the analysis, H8H8 elements with 40×40×40 cubic mesh are used with the GLS stabilization method. In the optimization, the volume constraint $V_{\min}$ is set at 50% solid volume in the design domain. Figure 3.4.6 shows that the topology optimization method creates a clear flow path inside the design domain, connecting one inlet with two outlets. Figure 3.4.7 presents the objective and constraint converges very well.

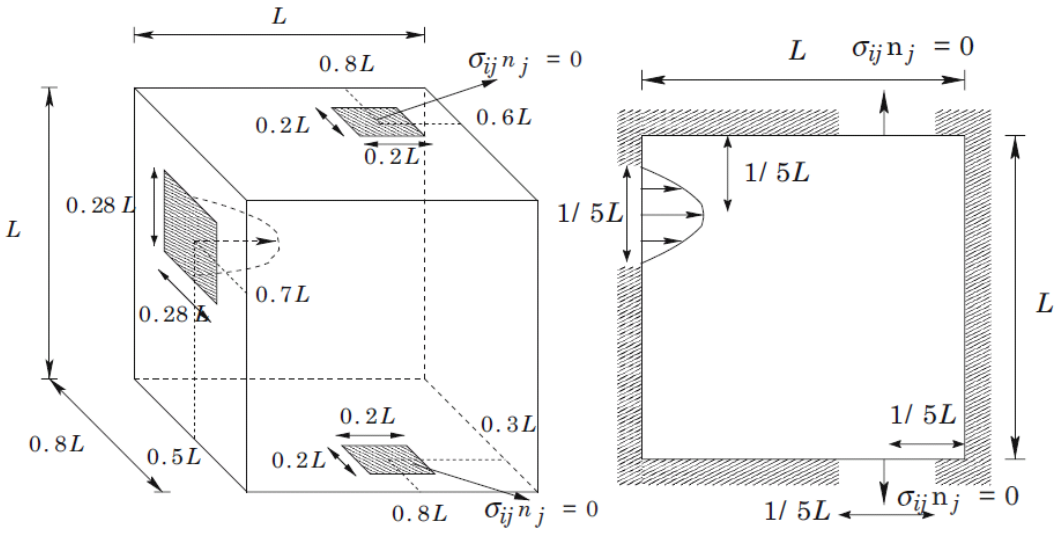

(a)

Reynolds number	ReL=100
Domain size	1×1×1
Mesh	40×40×40
Shape function (***v***, *p*)	H8H8
Stabilization method	SUPG+PSPG
Brinkman penalization	$\alpha_s=10^6$

(b)

Optimizer	MMA
Shape function (φ)	U1
Interpolation function	RAMP
Filtering method	Sensitivity filter
Additional constraint	5% move limit

(c)

Figure 3.4.5 [P8] 3D design example (a) design domain and boundary conditions (b) analysis setup (c) optimization setup

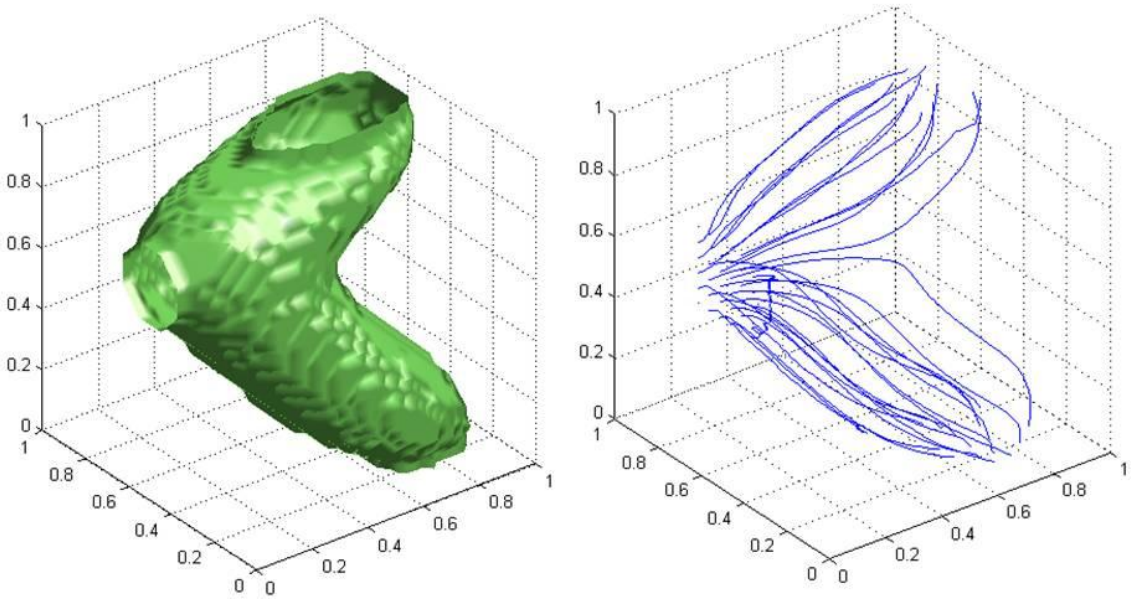

(a) (b)

Figure 3.4.6 [P8] Optimization results: (a) design result, (b) stream line graph

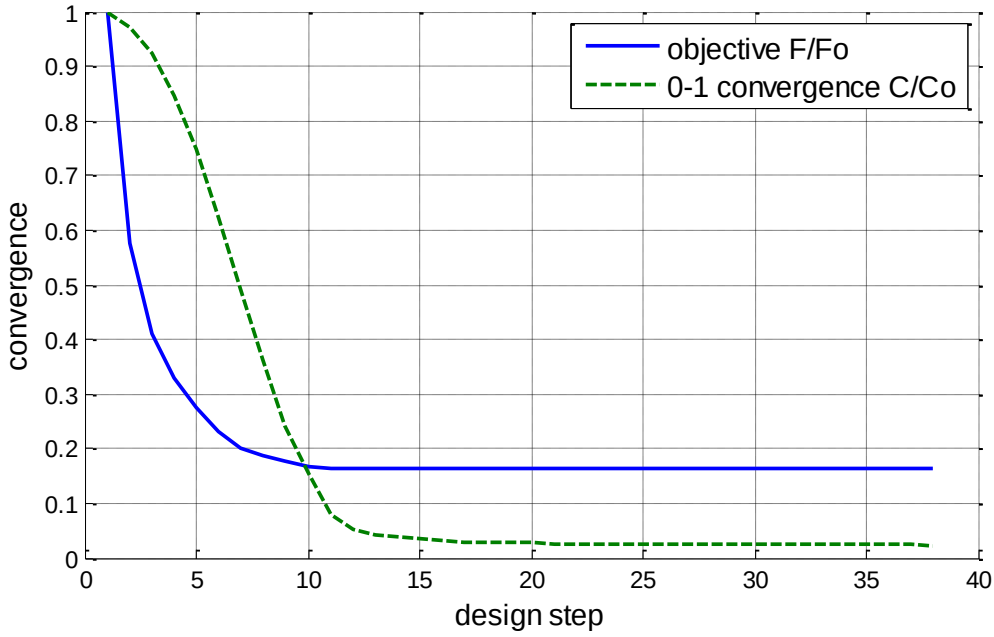

Figure 3.4.7 [P8] Convergence histories

3.5. Summary

In this chapter, the topology optimization of Navier-Stokes flow systems was formulated. Relaxation schemes of discrete physical parameters such as the Brinkman penalization parameter and the effective viscosity were revisited, and the adjoint sensitivity method for a steady-state nonlinear system was described in detail. After verifying the adjoint sensitivity method by comparing it with the finite difference sensitivity, this topology optimization method was verified by comparing the results with the previous topology optimization solutions of Stokes flow systems and the Pironneau's analytical solution [121].

I found numerical instabilities, such as element-scale cavities and boundary oscillations, which prevent the design from converging. These numerical instabilities do not result from an error in the sensitivity calculation or optimizer algorithms. Rather, they are caused by the numerical instabilities at the system analysis level, which are discussed in Section 2.5.2. Since the velocity and pressure oscillation becomes stronger as the Reynolds number increases, these numerical instabilities at the optimization level become more problematic with high Reynolds number flows.

Unlike the checkerboard problems of topology optimization, these numerical instabilities, developed from element-scale cavities, are not successfully suppressed by filtering schemes such as the density and sensitivity filter. This is mainly because the locations of the cavities are not fixed through the design steps. The most effective and easiest approach to prevent the instabilities is to apply a move limit. This constraint

successfully prevents the element-scale cavities and consequently suppresses boundary oscillations without a significant increase in computational cost.

Finally, 2D and 3D flow channels were designed. The objective function was to minimize kinetic power dissipation. The design solutions minimize skin friction with a low Reynolds number flow while they minimize pressure drag, creating a thin streamlined shape with a high Reynolds number flow.

CHAPTER 4

TOPOLOGY OPTIMIZATION OF CONVECTIVE COOLING SYSTEMS

4.1. Introduction

In accordance with the success of the topology optimization for Navier-Stokes flow systems (chapter 3), the topology optimization method is also applied to convective heat transfer problems in this chapter. For this multiphysics optimization, I analyze not only heat transfers, but also flow motion without using the approximated side convection coefficient 'h.' Therefore, this study extends previous topology optimization studies considered single physics pure heat conduction problems [63-67] or quasi-multiphysics heat transfer problems that use the side convection coefficient [68-70].

As explained in section 3.2, the discrete design variables are relaxed with continuous interpolation functions, and then the adjoint sensitivities [114] are calculated. There are two main differences between single physics fluid problems and these multiphysics problems. First, an additional physical property is introduced to distinguish heat transfer physics in free-fluid regions from those in solid regions. Second, the calculation of the adjoint sensitivity for nonlinear multiphysics systems is much more complicated [114].

After presenting the procedure for calculating design sensitivity, additional numerical instabilities, such as blocking wall designs resulting from unsuccessful Brinkman penalization, are discovered and investigated. Several strategies are suggested for preventing the blocking wall designs. Then, to validate the possibilities of the topology optimization method in convective-cooling device designs, 2D and 3D design problems with different Reynolds numbers and Prandtl numbers are presented and physically interpreted.

The outline of this chapter is as follows. Section 4.2 presents the topology optimization problems in convective heat transfer. Section 4.3 discusses numerical issues and possible remedies. 2D and 3D design problems are presenting in section 4.4. Section 4.5 summarizes this chapter.

4.2. Sensitivity analysis for multiphysics problems

As indicated in section 3.2, the discrete design variables should be relaxed with continuous interpolation functions, and the adjoint sensitivities should be calculated to efficiently solve topology optimization problems. This section presents interpolation functions used to relax the discrete design variables and explains how to calculate the adjoint sensitivities for steady-state nonlinear multiphysics systems.

4.2.1. Relaxation of variables for topology optimization

In the topology optimization of Navier-Stokes flow systems discussed in chapter 3, the Brinkman-penalization parameter α was controlled by design variables to distinguish the flow motion inside solid structures from those in free-fluid regions. In the same manner, additional material properties are needed to characterize the heat transfer physics inside solid structures or in free-fluid regions. Since this study conducts a full flow motion analysis, the control of heat conduction properties k is sufficient to distinguish the two different heat transfer physics as discussed in section 2.2.2.

The thermal conductivity k can be interpolated by using the RAMP interpolation function as

$$k(\varphi) = k_{\mathrm{s}} - (k_{\mathrm{s}} - k_{\mathrm{f}})\left(\frac{1-\varphi}{1-\varphi_{\min}}\right)\left(\frac{1-\varphi_{\min}+q_k}{1-\varphi+q_k}\right). \tag{4.2.1}$$

Here, $\varphi(\boldsymbol{r}) = 0$ or $\varphi_{\min}$ corresponds to k_{f}, the thermal conductivity of fluid, whereas $\varphi(\boldsymbol{r}) = 1$ corresponds to k_{s}, the thermal conductivity of solid material, at the location $\boldsymbol{r}$. Also a linear interpolation scheme (4.2.2) can be used following Li's work [123].

$$k(\varphi) = \frac{(1-\varphi)k_{\mathrm{f}} + (\varphi-\varphi_{\min})k_{\mathrm{s}}}{(1-\varphi)+(\varphi-\varphi_{\min})} \tag{4.2.2}$$

This linear interpolation for k introduces no penalty that steers the solution to discrete values. Yet, the 0-1 convergence of this interpolation is not notably inferior compared

with that of RAMP interpolation probably because the RAMP interpolation for α already has sufficient penalty effect. The relations between the design variable and the physics in the free-fluid and solid regions becomes as shown in Table 4.2.1.

Table 4.2.1 Design variables and physical properties

	Fluid region	**Solid region**
Design variable	$\varphi(\boldsymbol{r}) = 0, \varphi_{\min}$	$\varphi(\boldsymbol{r}) = 1$
Brinkman penalization parameter	$\alpha = \alpha_f \approx 0$	$\alpha = \alpha_s \approx \infty$
Heat conduction coefficient	$k(\varphi) = k_f$	$k(\varphi) = k_s$
Momentum equation	$\rho_f \boldsymbol{v} \cdot \nabla \boldsymbol{v} - \mu_f \nabla^2 \boldsymbol{v} + \nabla p = \boldsymbol{f}$	$-\mu_f \nabla^2 \boldsymbol{v} + \alpha \boldsymbol{v} + \nabla p = \boldsymbol{f}$ $\boldsymbol{v} \approx \boldsymbol{0}$
Energy equation	$\rho_f C_p \boldsymbol{v} \cdot \nabla T - \nabla \cdot \left(k_f \nabla T \right) = 0$	$-\nabla \cdot \left(k_s \nabla T \right) = 0$

Also, it should be noted that the RAMP interpolation scheme requires one more heuristic control parameter q_k, which makes it more difficult to control the already complicated multiphysics optimization problem. Therefore, to simplify the optimization problems, this study uses the same value for the control parameters q_α and q_k when RAMP interpolation scheme is used to interpolate both the Brinkman penalization parameter and the thermal conductivity.

4.2.2. Sensitivity analysis for multiphysics problems

Weakly coupled thermal-fluid equations (2.2.1) and (2.2.6) can be expressed in residual form as

$$\tilde{\boldsymbol{R}}_U\left(\boldsymbol{u}(\boldsymbol{\varphi}),\boldsymbol{\varphi}\right)=\boldsymbol{0} \tag{4.2.3}$$

$$\tilde{\boldsymbol{R}}_T\left(\boldsymbol{T}\left(\boldsymbol{u},\boldsymbol{\varphi}\right),\boldsymbol{u}(\boldsymbol{\varphi}),\boldsymbol{\varphi}\right)=\boldsymbol{0}\,. \tag{4.2.4}$$

Here, $\tilde{\boldsymbol{R}}_U$ and $\tilde{\boldsymbol{R}}_T$ is the residual form of the Brinkman-penalized Navier-Stokes equation and homogenized heat transfer equation, respectively; both residual forms include the stabilization terms. $\boldsymbol{u}$ is the fluid system response including velocity $\boldsymbol{v}$ and pressure p while $\boldsymbol{T}$ is the heat transfer system response, temperature. Also cost functions and constraints can be represented by the general response function F as

$$F\left(\boldsymbol{\varphi}\right)\equiv G\left(\boldsymbol{T}\left(\boldsymbol{u},\boldsymbol{\varphi}\right),\boldsymbol{u}(\boldsymbol{\varphi}),\boldsymbol{\varphi}\right). \tag{4.2.5}$$

Similarly to section 3.2.2, the dependence of the cost function F on the design vector $\boldsymbol{\varphi}$ has been rewritten using the function G so as to isolate its implicit dependence on $\boldsymbol{\varphi}$ through $\boldsymbol{u}(\boldsymbol{\varphi})$ and $\boldsymbol{T}(\boldsymbol{u}, \boldsymbol{\varphi})$ from the explicit dependence on $\boldsymbol{\varphi}$. Then the derivatives of the response function with respect to the design variable becomes

$$\frac{DF}{D\varphi_i}=\frac{\partial G}{\partial \boldsymbol{T}}\cdot\frac{D\boldsymbol{T}}{D\varphi_i}+\frac{\partial G}{\partial \boldsymbol{u}}\cdot\frac{D\boldsymbol{u}}{D\varphi_i}+\frac{\partial G}{\partial \varphi_i} \tag{4.2.6}$$

The derivative $D\boldsymbol{T}/D\varphi_i$ is an implicit quantity because the system response is implicitly defined through equation (4.2.4).

$$\frac{\partial \tilde{\boldsymbol{R}}_T}{\partial \boldsymbol{T}} \frac{D\boldsymbol{T}}{D\varphi_i} + \frac{\partial \tilde{\boldsymbol{R}}_T}{\partial \boldsymbol{u}} \frac{D\boldsymbol{u}}{D\varphi_i} = -\frac{\partial \tilde{\boldsymbol{R}}_T}{\partial \varphi_i}. \tag{4.2.7}$$

Then, by employing equation (3.1.7), $D\boldsymbol{T}/D\varphi_i$ can be obtained as

$$\frac{\partial \tilde{\boldsymbol{R}}_T}{\partial \boldsymbol{T}} \frac{D\boldsymbol{T}}{D\varphi_i} = \frac{\partial \tilde{\boldsymbol{R}}_T}{\partial \boldsymbol{u}} \left[\frac{\partial \tilde{\boldsymbol{R}}_U}{\partial \boldsymbol{u}} \right]^{-1} \frac{\partial \tilde{\boldsymbol{R}}_U}{\partial \varphi_i} - \frac{\partial \tilde{\boldsymbol{R}}_T}{\partial \varphi_i}. \tag{4.2.8}$$

The direct differentiation sensitivities is calculated by

$$\begin{aligned} \frac{DF}{D\varphi_i} = \frac{\partial G}{\partial \varphi_i} - \frac{\partial G}{\partial \boldsymbol{T}} \cdot \left(\frac{\partial \tilde{\boldsymbol{R}}_T}{\partial \boldsymbol{T}} \right)^{-1} \frac{\partial \tilde{\boldsymbol{R}}_T}{\partial \varphi_i} \\ - \left[- \frac{\partial G}{\partial \boldsymbol{T}} \cdot \left(\frac{\partial \tilde{\boldsymbol{R}}_T}{\partial \boldsymbol{T}} \right)^{-1} \frac{\partial \tilde{\boldsymbol{R}}_T}{\partial \boldsymbol{u}} \left(\frac{\partial \tilde{\boldsymbol{R}}_U}{\partial \boldsymbol{u}} \right)^{-1} + \frac{\partial G}{\partial \boldsymbol{u}} \cdot \left(\frac{\partial \tilde{\boldsymbol{R}}_U}{\partial \boldsymbol{u}} \right)^{-1} \right] \frac{\partial \tilde{\boldsymbol{R}}_U}{\partial \varphi_i}. \end{aligned} \tag{4.2.9}$$

However, topology optimization problems generally have much more design variables φ_i than response functions G, thus, this direct differentiation method is less efficient than the adjoint sensitivity method as discussed in section 3.2.2.

To obtain adjoint sensitivity, an augmented functional is first defined as the combination of equation (4.2.3), (4.2.4) and (4.2.5), given by

$$\hat{F}(\boldsymbol{\varphi}) \equiv G\left(\boldsymbol{T}(\boldsymbol{u},\boldsymbol{\varphi}),\boldsymbol{u}(\boldsymbol{\varphi}),\boldsymbol{\varphi}\right) - \boldsymbol{\lambda}_U(\boldsymbol{\varphi})\cdot\tilde{\boldsymbol{R}}_U\left(\boldsymbol{u}(\boldsymbol{\varphi}),\boldsymbol{\varphi}\right) - \boldsymbol{\lambda}_T(\boldsymbol{\varphi})\cdot\tilde{\boldsymbol{R}}_T\left(\boldsymbol{T}(\boldsymbol{u},\boldsymbol{\varphi}),\boldsymbol{u}(\boldsymbol{\varphi}),\boldsymbol{\varphi}\right) \quad . \tag{4.2.10}$$

Here, $\boldsymbol{\lambda}_U(\boldsymbol{\varphi})$ and $\boldsymbol{\lambda}_T(\boldsymbol{\varphi})$ are the Lagrange multipliers. Note that $\hat{F} = F$ since $\tilde{\boldsymbol{R}}_U$ and $\tilde{\boldsymbol{R}}_T$ are zero vectors. Differentiation of the above with respect to the individual design parameters φ_i yields

$$\frac{D\hat{F}}{D\varphi_i} = \frac{\partial G}{\partial \varphi_i} + \frac{\partial G}{\partial \boldsymbol{u}}\cdot\frac{D\boldsymbol{u}}{D\varphi_i} + \frac{\partial G}{\partial \boldsymbol{T}}\cdot\frac{D\boldsymbol{T}}{D\varphi_i} - \boldsymbol{\lambda}_U\cdot\left(\frac{\partial\tilde{\boldsymbol{R}}_U}{\partial\boldsymbol{u}}\frac{D\boldsymbol{u}}{D\varphi_i} + \frac{\partial\tilde{\boldsymbol{R}}_U}{\partial\varphi_i}\right) - \boldsymbol{\lambda}_T\cdot\left(\frac{\partial\tilde{\boldsymbol{R}}_T}{\partial\boldsymbol{u}}\frac{D\boldsymbol{u}}{D\varphi_i} + \frac{\partial\tilde{\boldsymbol{R}}_T}{\partial\boldsymbol{T}}\frac{D\boldsymbol{T}}{D\varphi_i} + \frac{\partial\tilde{\boldsymbol{R}}_T}{\partial\varphi_i}\right) \quad . \tag{4.2.11}$$

To isolate the implicit response sensitivities, I separate equation (4.2.11) into three terms

$$\frac{D\hat{F}}{D\varphi_i} = \frac{D\hat{F}_E}{D\varphi_i} + \frac{D\hat{F}_{I_1}}{D\varphi_i} + \frac{D\hat{F}_{I_2}}{D\varphi_i} \tag{4.2.12}$$

where $D\hat{F}_E/D\varphi_i$ is a explicit term and $D\hat{F}_{I_1}/D\varphi_i$ and $D\hat{F}_{I_2}/D\varphi_i$ are implicit terms, respectively, defined as

$$\frac{D\hat{F}_E}{D\varphi_i} = \frac{\partial G}{\partial\varphi_i} - \boldsymbol{\lambda}_U^T\cdot\frac{\partial\tilde{\boldsymbol{R}}_U}{\partial\varphi_i} - \boldsymbol{\lambda}_T^T\cdot\frac{\partial\tilde{\boldsymbol{R}}_T}{\partial\varphi_i} \tag{4.2.13}$$

$$\frac{D\hat{F}_{I_1}}{D\varphi_i} = \frac{D\boldsymbol{u}}{D\varphi_i} \cdot \left[\frac{\partial G}{\partial \boldsymbol{u}} - \left(\frac{\partial \tilde{\boldsymbol{R}}_U}{\partial \boldsymbol{u}} \right)^T \boldsymbol{\lambda}_U - \left(\frac{\partial \tilde{\boldsymbol{R}}_T}{\partial \boldsymbol{u}} \right)^T \boldsymbol{\lambda}_T \right] \tag{4.2.14}$$

$$\frac{D\hat{F}_{I_2}}{D\varphi_i} = \frac{D\boldsymbol{T}}{D\varphi_i} \cdot \left[\frac{\partial G}{\partial \boldsymbol{T}} - \left(\frac{\partial \tilde{\boldsymbol{R}}_T}{\partial \boldsymbol{T}} \right)^T \boldsymbol{\lambda}_T \right] \tag{4.2.15}$$

The implicit parts are eliminated from the sensitivity expression by defining the Lagrange multipliers $\boldsymbol{\lambda}_U$ and $\boldsymbol{\lambda}_T$ so that equation (4.2.14) and equation (4.2.15) equal zero as following

$$\boldsymbol{\lambda}_T = \left(\frac{\partial \tilde{\boldsymbol{R}}_T}{\partial \boldsymbol{T}} \right)^{-T} \frac{\partial G}{\partial \boldsymbol{T}} \tag{4.2.16}$$

$$\boldsymbol{\lambda}_U = \left(\frac{\partial \tilde{\boldsymbol{R}}_U}{\partial \boldsymbol{u}} \right)^{-T} \left\{ -\left(\frac{\partial \tilde{\boldsymbol{R}}_T}{\partial \boldsymbol{u}} \right)^T \boldsymbol{\lambda}_T + \frac{\partial G}{\partial \boldsymbol{u}} \right\}. \tag{4.2.17}$$

Then, sensitivity expression reduces to the explicit terms of sensitivities as

$$\frac{D\hat{F}_E}{D\varphi_i} = \frac{\partial G}{\partial \varphi_i} - \boldsymbol{\lambda}_U^T \cdot \frac{\partial \tilde{\boldsymbol{R}}_U}{\partial \varphi_i} - \boldsymbol{\lambda}_T^T \cdot \frac{\partial \tilde{\boldsymbol{R}}_T}{\partial \varphi_i} \tag{4.2.18}$$

This adjoint sensitivities equation is basically the same as the direct differentiation sensitivities equation (4.2.9). However, the number of response functional is generally much small compared with the number of design parameters in topology optimization problems. Therefore, it is more efficient to use the adjoint sensitivities than to use the direct differentiation sensitivities [114].

4.3. Numerical issues

This section presents a topology optimization example problem of thermal-fluid systems and discusses numerical difficulties in the optimization process. Despite the successful implementation of the topology optimization of Navier-Stokes flow systems, the Brinkman-penalization does not work properly during the topology optimization of multiphysics thermal-fluid systems, creating physically unacceptable design solutions. This section discusses the reason for the numerical difficulties with numerical examples and suggests possible solutions to circumvent the issues.

4.3.1. Unsuccessful Brinkman penalization and blocking wall designs

To clarify the numerical issue, this section considers an optimization problem of a 2D cooling channel depicted in Figure 4.3.1. The design goal is set to minimize mean temperature in the design domain. Parabolic flow profile with maximum flow velocity $U_{\max}$ and uniform temperature T_0 are given at the inlet boundary Γ_{in}. Zero pressure is assumed at the outlet boundary Γ_{out}, without loss of generality. A uniform heat influx 'h' is applied at the heating boundary Γ_{q}. At the remaining wall boundary Γ_{wall}, no-slip adiabatic boundary conditions are assumed. The material properties of antifreeze (50%) and aluminum are used for the fluid material and the solid structure respectively. The Reynolds number is first set to 10 and increased for later design, and the Prandtl number of the fluid is 7.2.

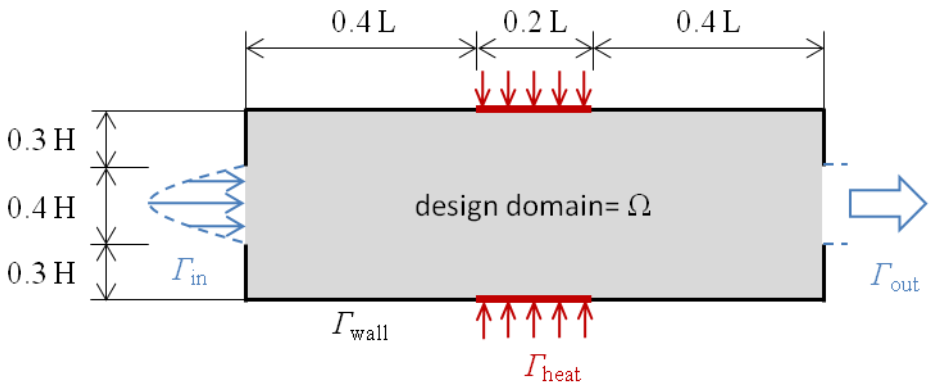

(a)

Material	Aluminum, Antifreeze (50%)
Reynolds number	ReH = 10, 100, 1000
Prandtl number	Pr = 7.2
Domain size	L×H = 3 × 1
Mesh	180×60, 360×120
Shape function (***v***, *p*, *T*)	Q4Q4-Q4
Stabilization method	GLS
Brinkman penalization	$\alpha_s = 10^6$

(b)

Optimizer	SLP, MMA
Shape function (φ)	Q4, U1
Interpolation function	RAMP
Filtering method	density filter
Additional constraint	move limit 5%

(c)

Figure 4.3.1. [P9] 2D cooling channel design (a) design domain and boundary conditions (b) analysis setup (c) optimization setup

The objective function and constraint function on the integral form are then defined respectively as

Minimize $$F_2(\varphi) = \frac{\int_\Omega T(\varphi) - T_0 \, d\Omega}{\int_\Omega 1 d\Omega} \tag{4.3.1}$$

Subject to $$\rho_f \boldsymbol{v} \cdot \nabla \boldsymbol{v} - \mu_f \nabla^2 \boldsymbol{v} + \alpha(\varphi)\boldsymbol{v} + \nabla p = \boldsymbol{f} \tag{4.3.2}$$

$$\rho_f C_p \boldsymbol{v} \cdot \nabla T - \nabla \cdot (k \nabla T) = 0 \tag{4.3.3}$$

$$\int_\Omega \varphi \, d\Omega = V^* \tag{4.3.4}$$

$$0 \le \varphi \le 1 \tag{4.3.5}$$

The solid volume fraction V^* is set to 0.2. The design variables are initially set to the same value as the solid volume fraction V^*.

Figure 4.3.2 shows the design result in case of Reh=10 and Reh=100, respectively. With this design, the structure blocks flow path, and therefore no fluid can run through the design domain in the real situation. However, this design results conflicts with the continuity equation and the given boundary condition, and therefore the coolant penetrates through the solid structures as shown in the streamline graph in Figure 4.3.2(c) and Figure 4.3.2(e). Since the continuity equation and boundary conditions overrode Brinkman penalization, the velocity was not penalized during FEM analysis and huge computational error was observed. For example, when ReH = 100, the final objective value F_o is only 13.3 according to the optimization result. However, if I cancel out the impossible flow motion and consequent convective heat transfer inside the solid structure,

the correct mean temperature in the system becomes over 154. Figure 4.3.3 illustrates the different temperature results. Since the Brinkman penalization did not enforce the zero fluid velocity condition inside the solid structure, creating solid-penetrating coolant flow, the temperature result, as shown Figure 4.3.3(d), becomes much better than the physically correct temperature profile shown in Figure 4.3.3(c).

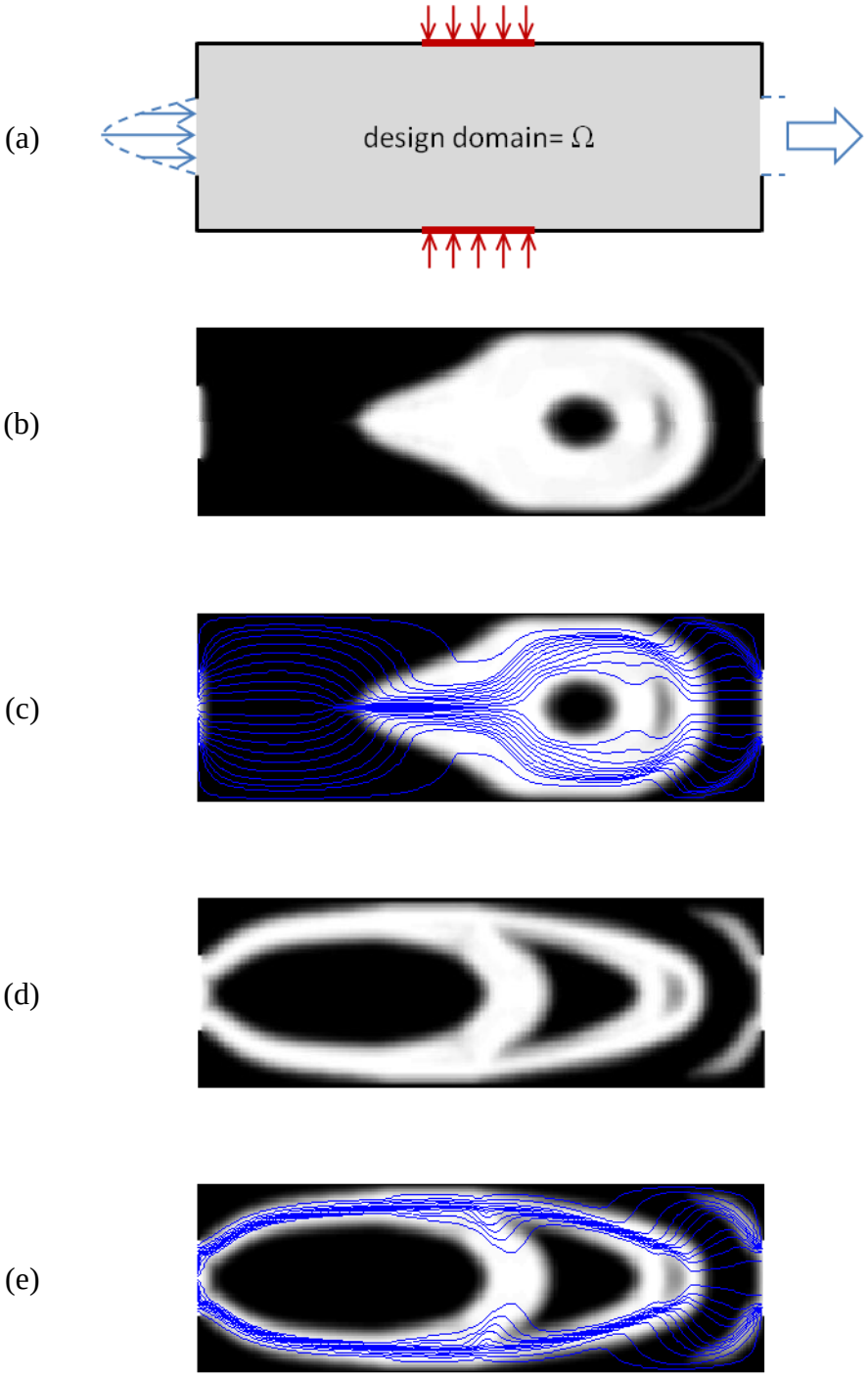

Figure 4.3.2. [P9] Design result of 2D cooling channel problems (a) design domain (b) cooling channel design, ReH=10 (c) streamline graph, ReH=10 (d) cooling channel design, ReH=100 (e) streamline graph, ReH=100

(a)

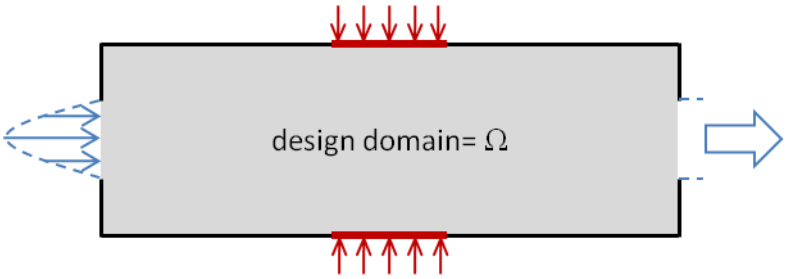

Design result

(b)

Correct temperature

(c)

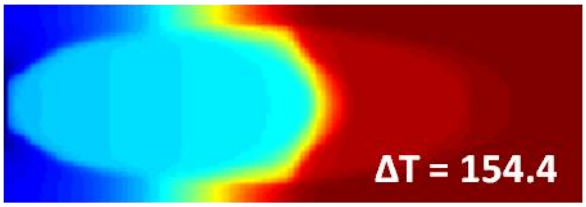

Calculated temperature with false-flow

(d)

Figure 4.3.3. [P9] Design and temperature results of 2D cooling channel problems at Reh=100 (a) design domain (b) design result (c) correct temperature profile (d) calculated temperature profile with solid-penetrating flow motion

Figure 4.3.4 and Figure 4.3.5 clearly illustrate the reason that the optimizer creates physically incorrect design solutions, like Figure 4.3.3(b) and (d). Both cases satisfy the design constraint, but the second design is unable to satisfy given boundary conditions in reality. Therefore, the zero fluid velocity condition cannot be satisfied with the Brinkman penalization scheme, creating only mathematically possible false-flow. As a result, the mathematically calculated temperature from the second case becomes much better not only than the physically correct temperature, but also than the temperature of the first design. Moreover, both conductive heat transfer and convective heat transfer occur in the blocking solid structure, improving the cooling effect. The optimizer tries to block the coolant flow and to create false-flow because the cooling effect from convective heat transfer is then added. This situation occurs frequently because optimizers, from my experience, try to take advantage of discrepancies in modeling.

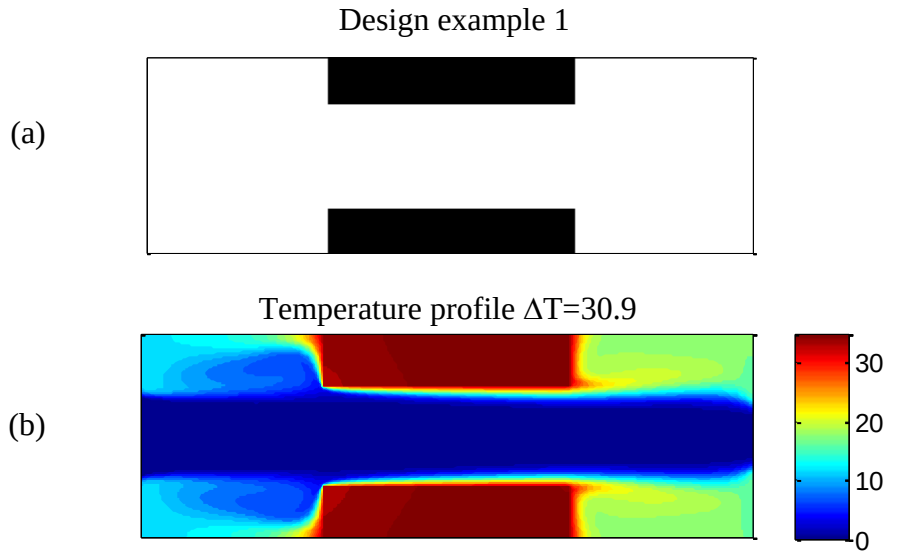

Figure 4.3.4. [P9] Case 1: design and temperature results (a) design (b) temperature

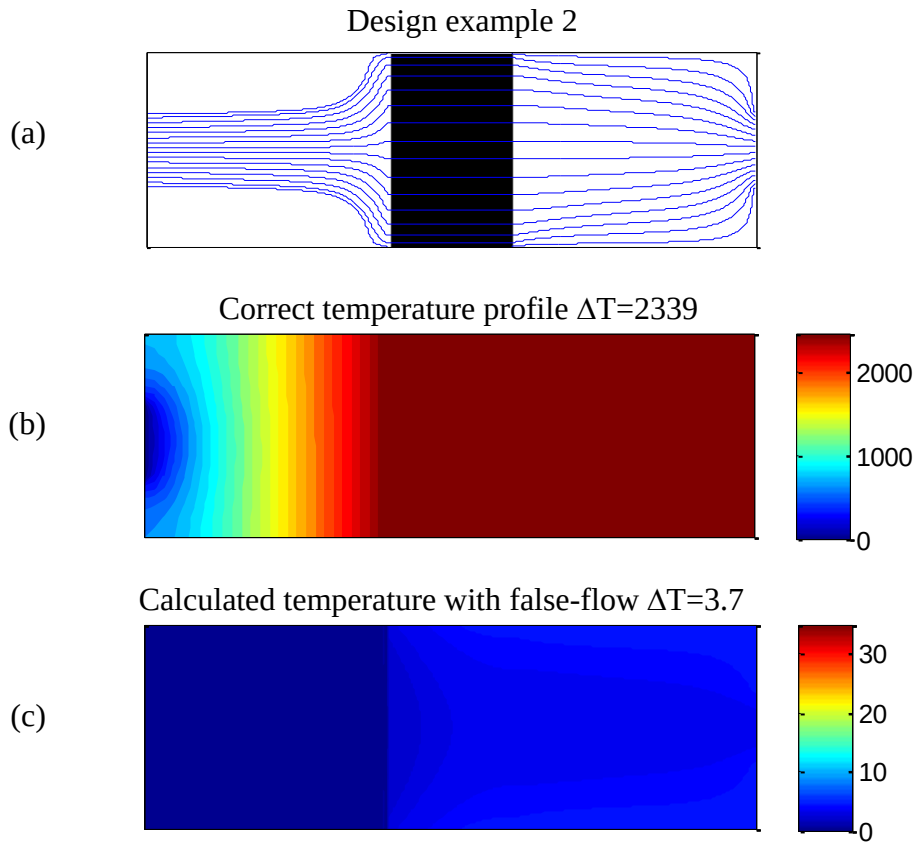

Figure 4.3.5. [P9] Case 2: design and temperature results (a) design (b) correct temperature (c) calculated temperature profile with solid-penetrating flow motion

4.3.2. Providing flow path

The first insight into resolving this numerical error was to increase the value of α_s, the Brinkman penalization parameter of the solid region, because a sufficiently large parameter usually enforces the Brinkman penalization and consequent zero velocity condition in the solid region. However the numerical error still occurred although the penalization parameter was increased from 1000 to 10^9. Moreover, when the value of α_s is too large, it degrades the condition number of the matrices and thus the accuracy of the performance and sensitivity analyses lessens.

The second insight is to provide a flow path inside the analysis domain. If there is a possible flow path from inlets to outlets, the flow motion obtained through the finite element method does not penetrate the solid region where the Brinkman penalization $-\alpha_s \boldsymbol{u}$ is applied to minimize the weighted residual. Figure 4.3.6 presents (a) a modified design domain having fixed flow path and new design results and streamline graphs with (b) ReH=10 and (c) ReH=100. Therefore, a provision of a flow path provided can prevent the blocking wall design and solid-penetrating flow motions.

However, it should be noted that the flow path inside the design domain should be carefully selected because an arbitrarily selected flow path will make it difficult to obtain an optimal design solution; heuristic approaches to obtaining an optimized design might be needed. On the other hand, if there is a pre-fixed bypass flow line outside the design domain as shown in Figure 4.3.7, an optimal design solution can be obtained analytically

by including the bypass line. Yet the additional analysis for a bypass flow motion requires more computation cost during system analysis.

(a)

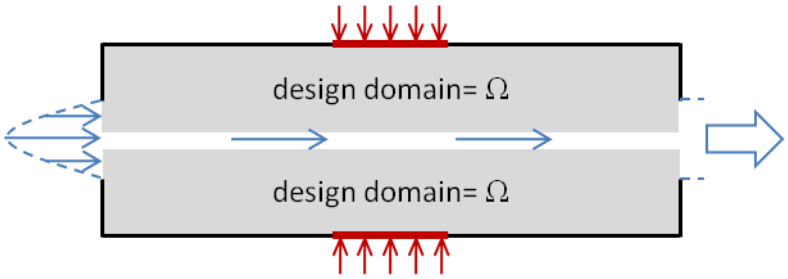

Design result ReH=10

(b)

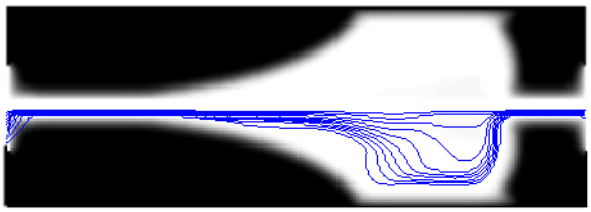

Design result ReH=100

(c)

Figure 4.3.6. [P10] Modified design domain of P9 and the design result
(a) modified design domain (b) design result and streamline graph at ReH=10
(c) design result and streamline graph at ReH=100

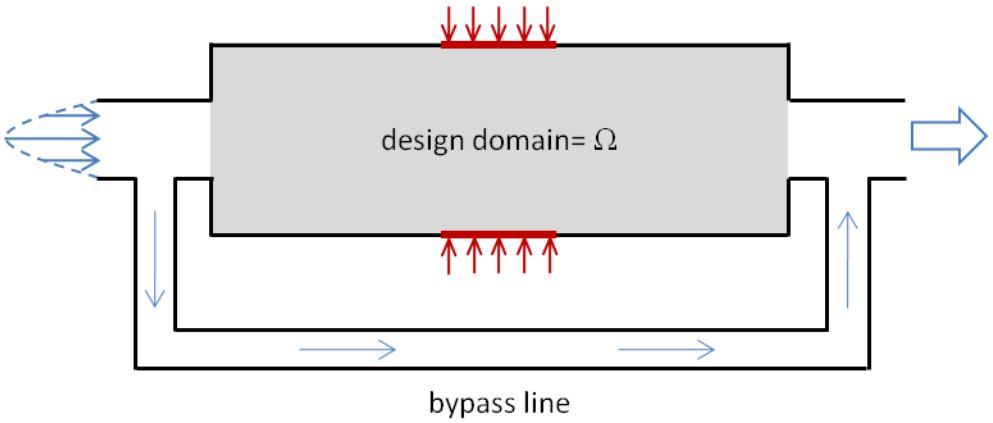

Figure 4.3.7. [P11] Modified analysis domain of P9 with bypass line

4.3.3. Multi-objective design

As for the third insight, rather than increasing the penalization parameter, I recognize that the false-flow motion in the solid structure causes a very high pressure drop, as shown in Figure 4.3.8. Therefore, controlling pressure drop by constricting or minimizing it would likely circumvent this numerical issue. To control pressure drop together with temperature minimization, I solve a multi-objective problem by selecting minimization of mean temperature and kinetic energy dissipation in the design domain. The minimization of kinetic energy dissipation is a well-known objective function, frequently used in the previous research [39, 48-51]. It results in minimization of pressure drop in the system [39] and is also easier to be implemented than limiting pressure drop itself. Then, the new objective function is as follows:

$$F_1(\varphi) = c_1\left\{\frac{1}{2}\left(\nabla\mathbf{u}, \mu_f \nabla\mathbf{u}\right) + \left(\mathbf{u}, \alpha(\varphi)\mathbf{u}\right)\right\} + c_2 \frac{\int T - T_0 \, dV}{\int 1 dV}. \tag{4.3.6}$$

c_1 and c_2 are scaling coefficients can be determined by adaptive weighting strategies described in [124]. In these examples, c_i is determined as

$$c_i = \left\| \frac{\partial F_i}{\partial \boldsymbol{\varphi}} \right\|^{-1}. \tag{4.3.7}$$

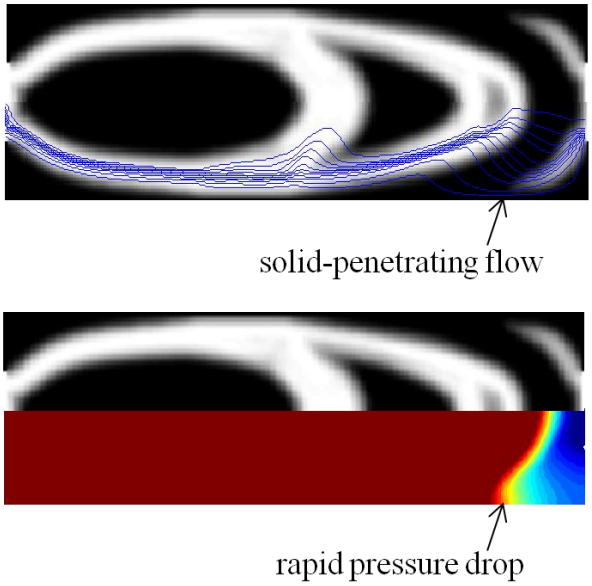

Figure 4.3.8. [P9] Design result and pressure profile of the 2D cooling channel problem

The design result and temperature profile with this multi-objective is shown in Figure 4.3.9(a) and (b) when ReH=100. A flow path has now been created near the outlet in order to minimize kinetic energy dissipation. Pressure drop is much smaller than the previous case, as shown in Figure 4.3.10. It is noted that the pressure drop results are slightly increases as the optimization progresses. This is the result that the optimizer changes intermediate porous region into solid or fluid region.

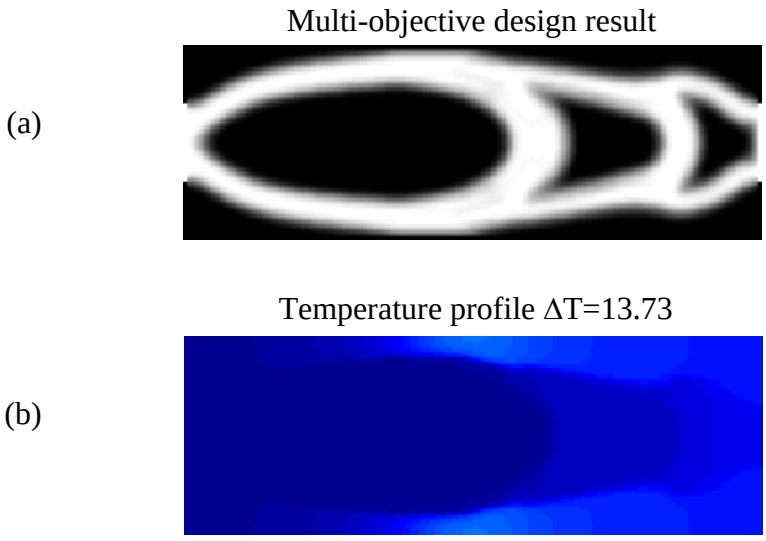

Figure 4.3.9. [P9] Design result of 2D cooling channel problems with new multi-objective function, Reh=100 (a) design result (b) temperature profile

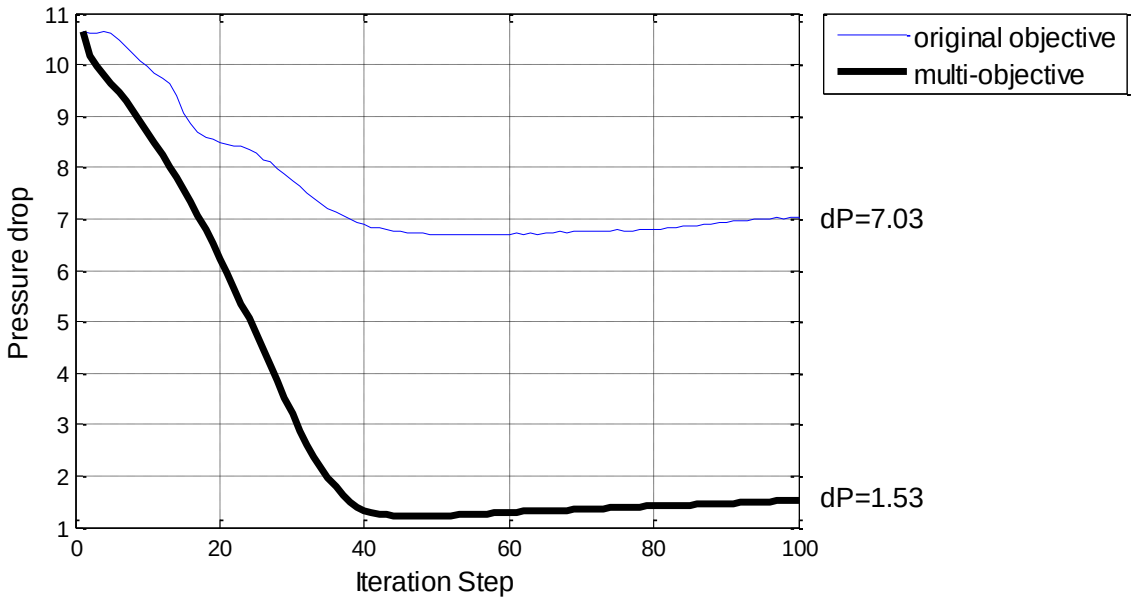

Figure 4.3.10. [P9] Pressure drop results according to the objective function

The temperature profile of the new design is slightly worse than the previous design result. However, if I compare it with the correct temperature result without false-flow motion, the temperature profile of the new design is much better. Note that Figure 4.3.9(a) shows two recirculation zones in the middle which should be avoided from a practical standpoint. These recirculation zones occurred due to the volume constraint. If I increase the solid volume in the design domain, the design results first fill out the recirculation zone allowing the flow path to remain. It should be mentioned that this multi-objective strategy should only be used for convection-dominated cases. For conduction-dominated cases, their design results always try to create unnecessary flow paths, which lead to a less effective cooling system structure.

4.4. Design of thermal-fluid cooling system

This section presents topology optimization problems of convective cooling systems. The design goal is to minimize mean temperature in the design domain but, to prevent the blocking wall design and solid-penetrating flow motion, multi-objective function described in equation (4.3.6) is used. 5% move limit is applied to prevent the boundary oscillations and consequent convergence issues. The density filter is also applied to obtain mesh-independent design solution. Then, the effects of the Reynolds number and Prandtl number change are discussed with design results.

4.4.1. 2D cooling channel designs

I designed 2D cooling channel previously depicted in Figure 4.3.1 by using the multi-objective function, equation (4.3.6). The material properties of antifreeze and air, whose Pr is 7.2 and 0.72 respectively, are used for the coolant with fixed inlet Reynolds numbers from 10 to 1000. The material properties of aluminum are used for the solid material. The solid volume fraction V* is set to 0.6 for all cases to observe the effect of different Reh and Pr numbers. The design variables are initially set to the same value as the solid volume fraction, V*. The mesh size is 360×120 and the degree of freedom is approximately 1.75×10^5 in the fluid analysis. The number of design variables is 4.32×10^4.

When antifreeze (Pr=7.2) is used, it leads to the three different optimization results, depending on the Reynolds number (Reh=10, 100, 1000) as presented in Figure 4.4.1. At low speed flow, the solid region is attached to the two heating areas in the middle of the top and bottom. However, as the Reynolds number is increased, the solid region is detached from the heating areas and coolant flow directly impinges on the heat source. With slower flow, the heat conduction effect becomes greater than the heat convection effect, and therefore it is better to have solid structures functioning as cooling fins to maximize the cooling effect by heat conduction. On the contrary, at higher Reynolds flow, the cooling effect by heat convection becomes dominant and thus direct cooling is preferable to attaching cooling fins to the heating area.

Figure 4.4.2 shows the optimization results when air is used for the coolant (Pr=0.72). The cases of Reh=10, 100 and 1000 are tested in the same manner. Unlike the antifreeze cases, the optimization results show similar structures in that aluminum is attached to

heating areas. Since the Prandtl number of air is much lower than antifreeze, the heat conduction effect is greater than the heat convection in all three cases. Topological changes are expected when the inlet fluid speed is increased, but I leave the analysis in the turbulent flow range for the future research. Although the Péclet numbers of the design shown in Figure 4.4.1(b) and Figure 4.4.2 (c) are the same as 72, the two design results are inconsistent with each other. Also the Péclet numbers in Figure 4.4.1(c) and Figure 4.4.2(d) are the same as 720, the design results are inconsistent with each other. Therefore overall design results should not be generalized by setting the same Péclet number.

(a)

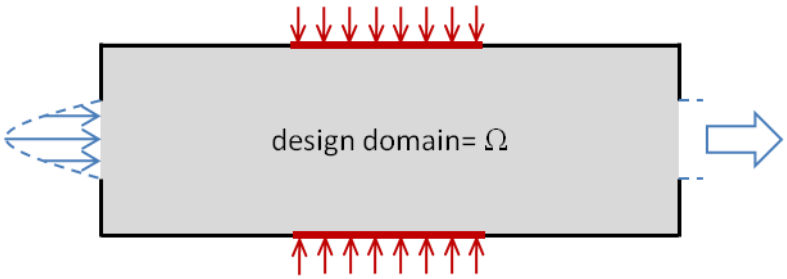

ReH=10 Pr=7.2

(b)

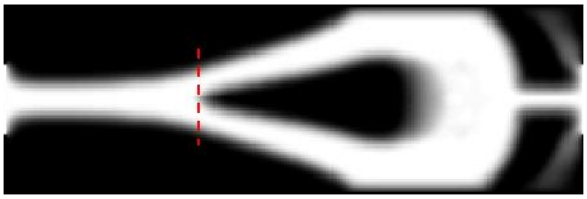

ReH=100 Pr=7.2

(c)

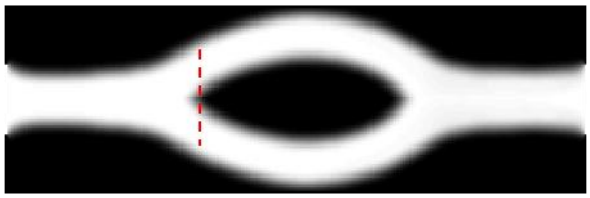

ReH=1000 Pr=7.2

(d)

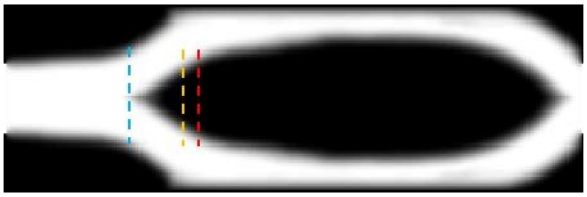

Figure 4.4.1. [P9] 2D design result with antifreeze (50%) flow (a) design domain (b) ReH=10, Pr=7.2 (c) ReH=100, Pr=7.2 (d) ReH=1000, Pr=7.2

(a)

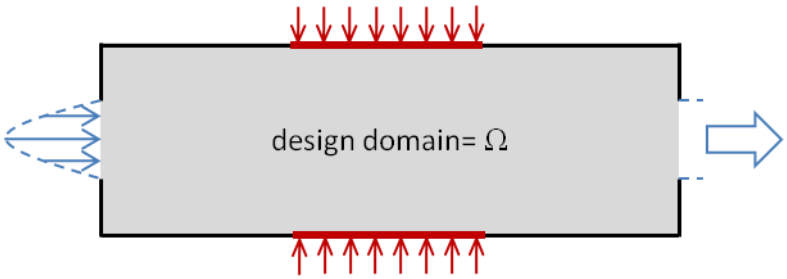

ReH=10 Pr=0.72

(b)

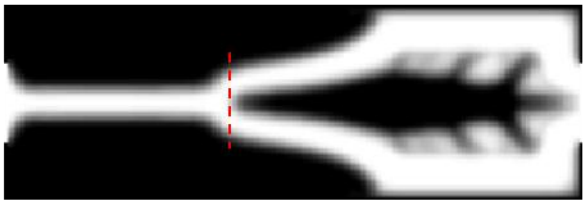

ReH=100 Pr=0.72

(c)

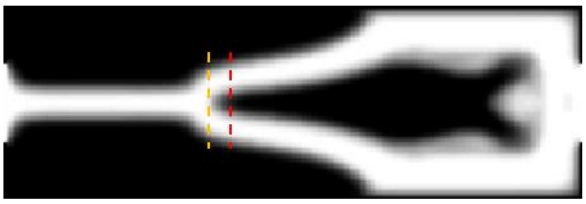

ReH=1000 Pr=0.72

(d)

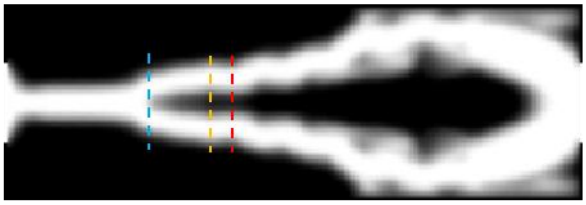

Figure 4.4.2. [P9] 2D design result with air flow (a) design domain (b) ReH=10, Pr=0.72 (c) ReH=100, Pr=0.72 (d) ReH=1000, Pr=0.72

4.4.2. 3D cooing channel designs

3D design optimization results are presented for the cooling system design as depicted in Figure 4.4.3. The initial condition, boundary condition and material properties are similar to those for the 2D cooling channel design, but the Prandtl number is set to 6.67. The mesh size is 120×40×40, and the degree of freedom in the fluid analysis is approximately 8.14×10^5.

The same multi-objective function is used as shown in section 4.3.3, and the solid volume constraint is set to 0.91. This optimization problem is stated as:

$$\text{Minimize} \qquad F_1(\varphi) = c_1 \frac{\int T - T_0 \, dV}{\int 1 dV} + c_2 \left\{ \frac{1}{2} \left(\nabla \mathbf{u}, \mu_f \nabla \mathbf{u} \right) + \left(\mathbf{u}, \alpha(\varphi) \mathbf{u} \right) \right\} \tag{4.4.1}$$

$$\text{Subject to} \qquad \rho_f \boldsymbol{v} \cdot \nabla \boldsymbol{v} - \mu_f \nabla^2 \boldsymbol{v} + \alpha(\varphi) \boldsymbol{v} + \nabla p = \boldsymbol{f} \tag{4.4.2}$$

$$\rho_f C_p \boldsymbol{v} \cdot \nabla T - \nabla \cdot \left(k(\varphi) \nabla T \right) = 0 \tag{4.4.3}$$

$$\int_\Omega \varphi \, d\Omega = V^* = 0.91 \tag{4.4.4}$$

$$0 \le \varphi \le 1 \tag{4.4.5}$$

The number of design variables is 1.92×10^5. The design variables are initially set to the same value as the solid volume fraction V^*.

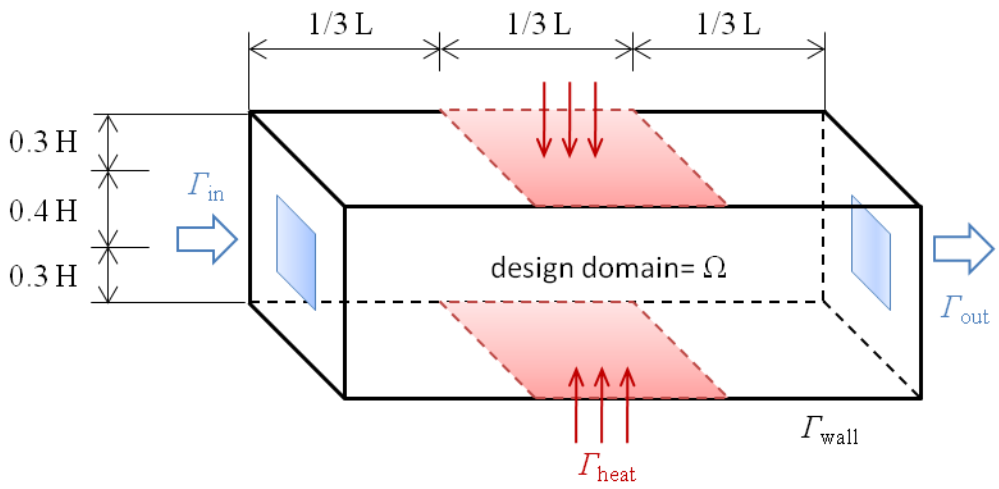

(a)

Material	aluminum, antifreeze (50%)
Reynolds, Prandtl number	ReH=10, 100, 400 1000 / Pr=6.67
Domain and mesh size	L×H = 3×1, (120×40×40)
Shape function (***v***, *p*, *T*)	H8H8-H8
Stabilization method	GLS
Brinkman penalization	$\alpha_s = 10^6$

(b)

Optimizer	SLP
Shape function (φ)	U1
Interpolation function	RAMP
Filtering method	density filter
Additional constraint	5% move limit

(c)

Figure 4.4.3. [P12] 3D cooling channel design (a) design domain and boundary conditions (b) analysis setup (c) optimization setup

Figure 4.4.4 and Figure 4.4.5 show the optimization results depending on the inlet Reynolds numbers. Overall, the optimization results show a similar trend to the 2D cooling system design results. For low Reh flow, the multi-objective optimization result is almost identical to the result when only the minimization of the kinetic energy dissipation is used for the objective function. In this case, the heat convection effect is not dominant and, as a result, the effect of flow motion change is limited. For higher speed flow, to maximize the convective cooling effect, the flow channel directly impinges on the heating areas.

It is noted that the design results and non-dimensionalized temperature profiles show no difference depending on the change of heat influx value ‘q’ for the following reasons. First material properties are assumed as constant irrelevant to temperature change. Second the governing equation is not fully coupled with each other; the change of heat influx and following temperature change don’t influence fluid velocity and, as a result, the heat transfer equation is linear to heat influx with the same heat convection.

(a)

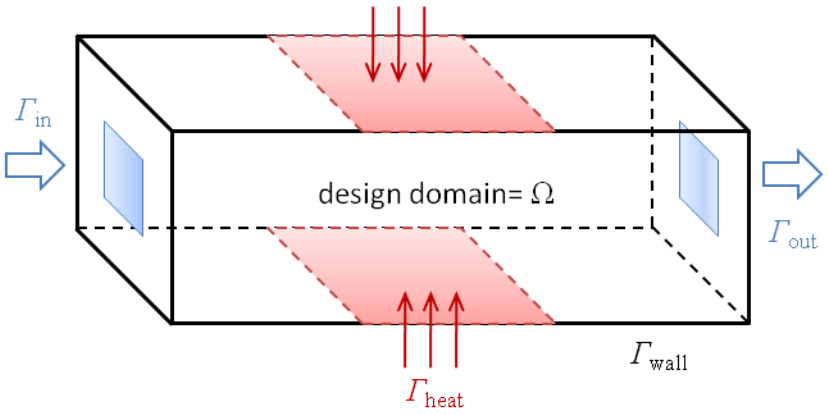

(b)

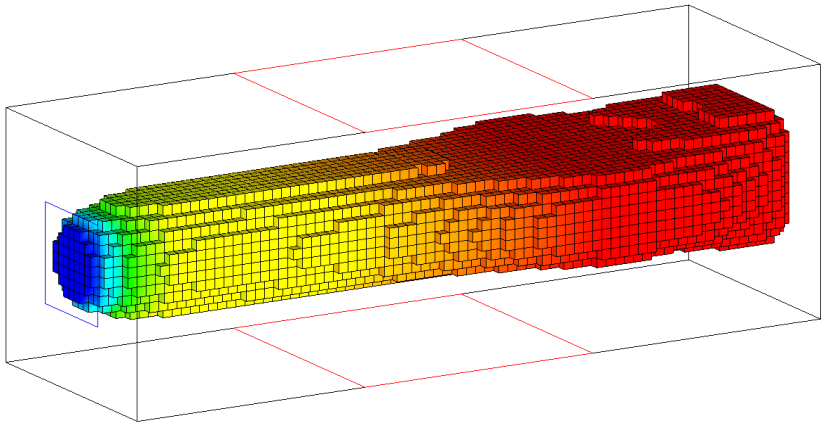

ReH=10

(c)

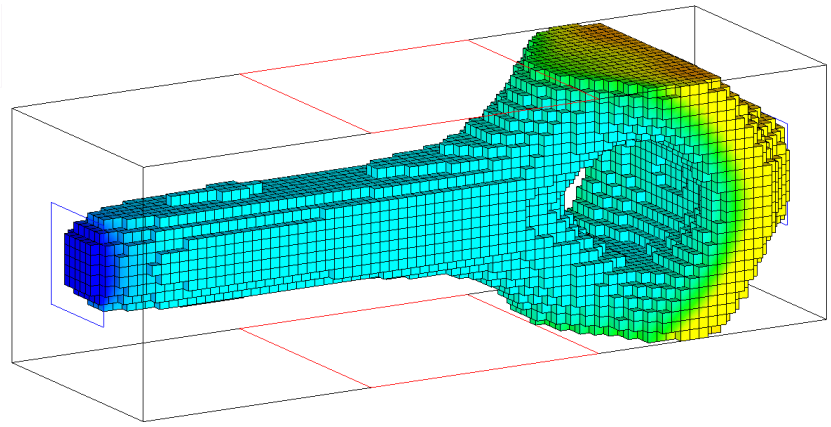

ReH=100

Figure 4.4.4. [P12] 2D design result with air flow (a) design domain (b) ReH=10, Pr=0.72 (c) ReH=100, Pr=0.72 (d) ReH=1000, Pr=0.72

(a)

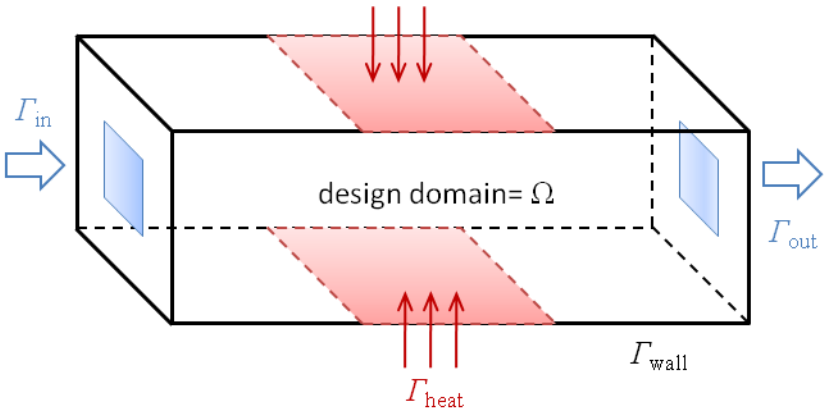

(d)

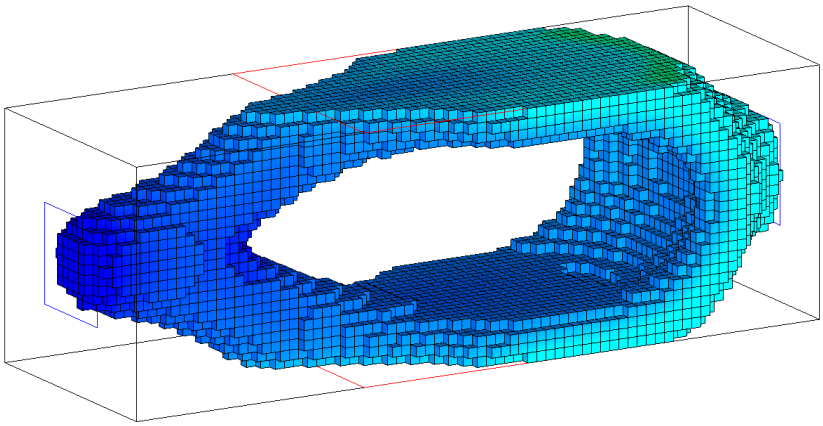

ReH=400

(e)

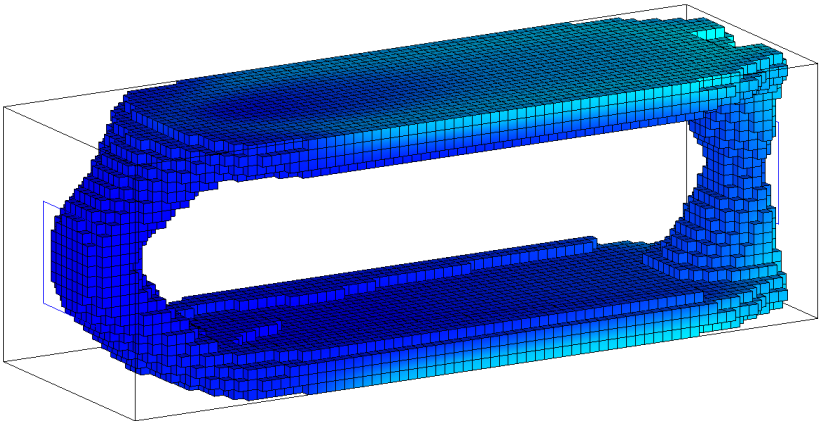

ReH=1000

Figure 4.4.5. [P12] 2D design result with air flow (a) design domain (b) ReH=10, Pr=0.72 (c) ReH=100, Pr=0.72 (d) ReH=1000, Pr=0.72

4.5. Summary

In this chapter, the topology optimization method of convective cooling systems was presented. The main design purpose was to design a flow channel to minimize temperature. After relaxation schemes of the thermal conductivity were revisited, the adjoint sensitivity method for weakly coupled multiphysics systems was formulated, extending the adjoint sensitivity formulation for steady-state nonlinear systems.

The Brinkman penalization, which is successfully applied to the topology optimization of single physics Navier-Stokes flow systems as shown in chapter 3, fails to enforce the zero-velocity condition inside solid structures and the no-slip boundary condition at solid surfaces. This happens when the design results block all possible coolant flow paths. Such designs conflict with the principle of mass conservation and given boundary conditions. As a result, the mass conservation law and given boundary conditions override the Brinkman penalization, creating solid-penetrating false flow. Since the mathematically calculated cooling effect with the false flow is usually superior, optimizers prefer to design the blocking walls ignoring the Brinkman penalization.

If a fixed flow path from inlets to outlets is given, there is no possible conflict between the design and the physical laws. Thus, the topology optimization method produces physically correct design results. Therefore, providing a fixed-flow path inside or outside of the design domains resolves this numerical issue. However, the flow path inside the design domain is heuristically given, and the flow path outside the design domain increases computational cost.

Mathematically, the false flow generates a high pressure drop when it penetrates solid structures. Therefore, a multi-objective function to minimize both the pressure drop and temperature was implemented to circumvent the numerical issue and successfully produces physically acceptable optimization results. Implementing the multi-objective function enabled the solution of example problems of 2D and 3D convective cooling systems, and the effect of Reynolds number and Prandtl number changes were explored.

CHAPTER 5

CONCLUSION

5.1. Concluding remarks

This dissertation investigates the topology optimization of convective cooling systems, extending previous topology optimization research of Stokes flow systems and heat conduction systems. The flow analysis results are used to solve the thermal transport equation without using the heat convection coefficient. For accurate and cost-effective analysis, the stabilized finite element methods and the adjoint sensitivity for weakly coupled multiphysics systems are implemented. Numerical instabilities are presented and discussed at the system analysis and design optimization levels. 2D and 3D flow channels are designed as design examples to minimize the kinetic energy dissipation or to minimize the temperature in the system.

Thermal-fluid analysis for topology optimization

This study introduces a fictitious domain approach, which uses an immersed boundaries concept, Brinkman penalization and the homogenized property of thermal

conductivity. By implementing this analysis method, this study extends the region topology optimization from linear Stokes flow and heat conduction systems to convective cooling systems that are nonlinear coupled multiphysics systems. A guideline for setting a proper lower bound of the Brinkman penalization parameter is presented. When the Brinkman penalization parameter is greater than 10^6 ($Da=10^{-6}$), the zero-velocity condition in solid regions and the no-slip boundary condition at solid boundaries are satisfied. To establish a stable and cost-effective method, various stabilized finite element methods are examined, and the Newton-Raphson method is used with a simultaneous stabilization tensor update scheme and Reynolds-Ramping initial guess strategy. Numerical issues such as velocity and pressure oscillations are presented.

These numerical instabilities occur because the velocity gradient changes too sharply at the fluid-solid interfaces for the stabilized finite element solution to correctly capture the velocity profile. The oscillation becomes severe when the Reynolds number increases. Although mesh refinement can smooth this oscillation, it is not viable because it increases the computation cost of the topology optimization. The GLS stabilization method produces the weakest oscillation, but the difference in solutions produced by different stabilization tensors is not significant.

Topology optimization of Navier-Stokes flow systems

The topology optimization of Navier-Stokes flow systems is investigated, extending previous topology optimization researches of Stokes flow systems to nonlinear Navier-Stokes flow system. The adjoint sensitivity method is implemented, and relaxation schemes used in previous topology optimization of Stokes flow systems are revised.

Element-scale cavities and consequent boundary oscillation phenomenon, which prevent design convergence, are presented and investigated. These numerical instabilities result from the numerical issues in the system analysis such as pressure oscillation at the immersed boundaries. A move-limit successfully suppresses the numerical instabilities while the density filter, the sensitivity filter and higher interpolation functions for design variables are not effective. Using this approach, I present 2D and 3D design problems and interpret the physics in the design solutions. The objective function is the minimization of kinetic energy dissipation or drag minimization. The design solutions minimize skin friction with a low Reynolds number while minimizing pressure drag, creating a thin streamlined shape with a high Reynolds number.

Topology optimization of convective cooling systems

The topology optimization of convective cooling systems is investigated, extending and combining previous topology optimization research of Navier-Stokes flow systems and heat conduction systems. The main design purpose is to design a flow channel to maximize cooling efficiency. The adjoint sensitivity method is formulated for nonlinear multiphysics problems, and relaxation schemes used in previous topology optimization are revised. The optimizer frequently tries to produce physically impossible design results that have a conflict between the Brinkman penalization from the mass conservation law and given boundary conditions. This is because the mathematically calculated cooling effect is superior given this conflict. However, in reality, no coolant flow can run through the system designed, so the temperature is very high. This numerical issue can be circumvented by providing a fixed-flow path or by solving a multi-objective function that

minimizes both temperature and pressure drop. Finally, by implementing the multi-objective function, example problems of 2D and 3D convective cooling systems are solved and the effect of Reynolds number and Prandtl number changes are discussed.

5.2. Future works

Following are some of the interesting directions to which this research can be extended.

Implementing fully coupled physical properties

This dissertation reviewed the thermal-fluid analysis method, which includes the Brinkman-penalized Navier-Stokes equation (2.2.3) and the homogenized thermal transport equation (2.2.6). In the momentum equation, the material properties relating to temperature are assumed as constants, so as to decouple temperature and enable cost effective analysis. However, the material properties, such as fluid density and viscosity should be assumed as functions of temperature instead of constants in order to obtain accurate solutions when the temperature varies significantly. In such cases, the velocity, pressure and temperature profiles should be calculated simultaneously, while this study solves the momentum equation and the energy equation sequentially. An analysis of the differences between the optimum shapes obtained under different conditions of the physical properties would be a valuable contribution.

Topology optimization to minimize the thermal stress

The main goal of this study is to applying the topology optimization in designing convective cooling systems, and I designed several cooling channels minimizing the mean temperature in the systems. Yet, in some applications, thermal stress is a more critical factor than the mean temperature. For example, non-uniform temperature distribution in an engine head induces thermo mechanical stresses in the structure and may cause cracks, as shown in Figure 5.2.1. The increased risk of fatigue-failure connected to the higher thermal loads requires a careful optimization of the coolant gallery design [8]. Therefore, designing the optimal structure maximizing the stiffness or minimizing the compliance of structure would be a valuable contribution. The proposed methodology is to decouple structural and thermal-fluid analysis. First, the thermal-fluid analysis is performed in order to evaluate the temperature distribution within the system. Then, the structural analysis is carried out with the temperature result. Ignoring the fluid-structure interaction might represent a good trade-off between accuracy and computational cost.

Figure 5.2.1. Crack growth in the engine head [8]

Adding the effect of the viscous dissipation

From practical standpoint, the present work neglects the effect of the viscous dissipation term on heat transfer. Although this computational model is expected to be reasonably accurate for most applications, this viscous dissipation term can be important when the viscosity and velocity gradients are high. Furthermore, the multi-objective function (4.4.1), used to resolve the blocking wall design, includes the kinetic dissipation terms. Therefore, an investigation of the alterations induced by viscous dissipation in the optimum channel shape would enhance our understanding.

APPENDIX

APPENDIX A
VARIATIONAL MULTISCALE STABILIZATION METHOD FOR THE BRINKMAN-PENALIZED NAVIER-STOEKS EQUATION

A.1. Multiscale decomposition

The weak formulation of the Brinkman penalized Navier-Stokes equation is given by

$$\langle \boldsymbol{w}, \alpha \boldsymbol{v} \rangle_{\Omega} + \langle \boldsymbol{w}, \rho_f \boldsymbol{v} \cdot \nabla \boldsymbol{v} \rangle_{\Omega} + \langle \nabla \boldsymbol{w}, 2\mu_f \nabla \boldsymbol{v} \rangle_{\Omega} - \langle div\, \boldsymbol{w}, p \rangle_{\Omega} = \langle \boldsymbol{w}, \boldsymbol{f} \rangle_{\Omega} + \langle \boldsymbol{w}, \boldsymbol{t} \rangle_{\Gamma_N} \quad \text{(A.1.1)}$$

$$\langle q, div\, \boldsymbol{v} \rangle_{\Omega} = 0 \quad \text{(A.1.2)}$$

where $\langle \cdot, \cdot \rangle_{\Omega} = \int_{\Omega} (\cdot)\, d\Omega$ is the inner product in L^2, $\boldsymbol{w}$ an weighting function. We consider the bounded domain Ω discretized into n non-overlapping region Ω^e (element domains) with boundaries Γ^e. Decompose the velocity field into coarse scales (resolvable scales) and fine scales (sub-grid scales) as

$$\begin{aligned} \boldsymbol{w} &= \underset{\text{coarse}}{\bar{\boldsymbol{w}}(\boldsymbol{x})} + \underbrace{\boldsymbol{w}'(\boldsymbol{x})}_{\text{fine}} \\ \boldsymbol{v} &= \underset{\text{coarse}}{\bar{\boldsymbol{v}}(\boldsymbol{x})} + \underset{\text{fine}}{\boldsymbol{v}'(\boldsymbol{x})} \\ \boldsymbol{w}' &= \boldsymbol{v}' = 0 \qquad \text{on } \Gamma^e \end{aligned} \quad \text{(A.1.3)}$$

We now substitute the trial solutions $\boldsymbol{v}$ and the weighting functions $\boldsymbol{w}$ in the standard variational form as

$$\left\{\begin{array}{l}\left\langle \bar{\boldsymbol{w}}+\boldsymbol{w}', \alpha\left(\bar{\boldsymbol{v}}+\boldsymbol{v}'\right)\right\rangle_{\Omega}+\left\langle \bar{\boldsymbol{w}}+\boldsymbol{w}', \rho_f\left(\bar{\boldsymbol{v}}+\boldsymbol{v}'\right)\cdot\nabla\left(\bar{\boldsymbol{v}}+\boldsymbol{v}'\right)\right\rangle_{\Omega} \\ \quad +\left\langle \nabla\left(\bar{\boldsymbol{w}}+\boldsymbol{w}'\right), 2\mu_f\nabla\left(\bar{\boldsymbol{v}}+\boldsymbol{v}'\right)\right\rangle_{\Omega}-\left\langle div\left(\bar{\boldsymbol{v}}+\boldsymbol{v}'\right), p\right\rangle_{\Omega}\end{array}\right\}=\left\langle \bar{\boldsymbol{w}}+\boldsymbol{w}', \boldsymbol{f}\right\rangle_{\Omega}+\left\langle \bar{\boldsymbol{w}}+\boldsymbol{w}', \boldsymbol{t}\right\rangle_{\Gamma_N}$$

(A.1.4)

$$\left\langle q, div\left(\bar{\boldsymbol{v}}+\boldsymbol{v}'\right)\right\rangle_{\Omega}=0 \tag{A.1.5}$$

By employing the linearity of the weighting function, the Brinkman penalized Navier-Stokes equation can be divided into coarse and fine-scale parts as

coarse:

$$\left\{\begin{array}{l}\left\langle \bar{\boldsymbol{w}}, \alpha\left(\bar{\boldsymbol{v}}+\boldsymbol{v}'\right)\right\rangle_{\Omega}+\left\langle \bar{\boldsymbol{w}}, \rho_f\boldsymbol{v}^c\cdot\nabla\left(\bar{\boldsymbol{v}}+\boldsymbol{v}'\right)\right\rangle_{\Omega} \\ \quad +\left\langle \nabla\bar{\boldsymbol{w}}, 2\mu_f\nabla\left(\bar{\boldsymbol{v}}+\boldsymbol{v}'\right)\right\rangle_{\Omega}-\left\langle div\,\bar{\boldsymbol{w}}, p\right\rangle_{\Omega}\end{array}\right\}=\left\langle \bar{\boldsymbol{w}}, \boldsymbol{f}\right\rangle_{\Omega}+\left\langle \bar{\boldsymbol{w}}, \boldsymbol{t}\right\rangle_{\Gamma_N} \tag{A.1.6}$$

$$\left\langle q, div\left(\bar{\boldsymbol{v}}+\boldsymbol{v}'\right)\right\rangle_{\Omega}=0 \tag{A.1.7}$$

fine:

$$\left\{\begin{array}{l}\left\langle \boldsymbol{w}', \alpha\left(\bar{\boldsymbol{v}}+\boldsymbol{v}'\right)\right\rangle_{\Omega}+\left\langle \boldsymbol{w}', \rho_f\boldsymbol{v}^c\cdot\nabla\left(\bar{\boldsymbol{v}}+\boldsymbol{v}'\right)\right\rangle_{\Omega} \\ \quad +\left\langle \nabla\boldsymbol{w}', 2\mu_f\nabla\left(\bar{\boldsymbol{v}}+\boldsymbol{v}'\right)\right\rangle_{\Omega}-\left\langle div\,\boldsymbol{w}', p\right\rangle_{\Omega}\end{array}\right\}=\left\langle \boldsymbol{w}', \boldsymbol{f}\right\rangle_{\Omega} \tag{A.1.8}$$

Here, $\boldsymbol{v}^c$ is the last solution from the Newton-Raphson iteration.

A.2. Solution of the fine-scale problem

Rearrange fine-scale equation as

$$\begin{aligned}
&\left\langle \boldsymbol{w}', \alpha \boldsymbol{v}' \right\rangle_{\Omega} + \left\langle \boldsymbol{w}', \rho_f \boldsymbol{v}^c \cdot \nabla \boldsymbol{v}' \right\rangle_{\Omega} + \left\langle \nabla \boldsymbol{w}', 2\mu_f \nabla \boldsymbol{v}' \right\rangle_{\Omega} \\
&\quad = \left\langle \boldsymbol{w}', \boldsymbol{f} \right\rangle_{\Omega} - \left\langle \boldsymbol{w}', \nabla p \right\rangle_{\Omega} - \left\langle \boldsymbol{w}', \alpha \bar{\boldsymbol{v}} \right\rangle_{\Omega} - \left\langle \boldsymbol{w}', \rho_f \boldsymbol{v}^c \cdot \nabla \bar{\boldsymbol{v}} \right\rangle_{\Omega} - \left\langle \nabla \boldsymbol{w}', 2\mu_f \nabla \bar{\boldsymbol{v}} \right\rangle_{\Omega} \\
&\quad = \left\langle \boldsymbol{w}', \left(\boldsymbol{f} - \nabla p - \alpha \bar{\boldsymbol{v}} - \rho_f \boldsymbol{v}^c \cdot \nabla \bar{\boldsymbol{v}} + 2\mu_f \nabla \bar{\boldsymbol{v}} \right) \right\rangle_{\Omega} = \left\langle \boldsymbol{w}', \bar{\boldsymbol{r}} \right\rangle_{\Omega}
\end{aligned} \tag{A.2.1}$$

where $\bar{\boldsymbol{r}} = \boldsymbol{f} - \nabla p - \alpha \bar{\boldsymbol{v}} - \rho_f \boldsymbol{v}^c \cdot \nabla \bar{\boldsymbol{v}} + 2\mu_f \nabla \bar{\boldsymbol{v}}$. Assume the fine scale $\boldsymbol{v}'$ and $\boldsymbol{w}'$ are represented via bubble functions as

$$\begin{aligned}
\boldsymbol{v}_i' |_{\Omega^e} &= b_1^e \boldsymbol{\beta}_i \ , \\
\boldsymbol{w}_i' |_{\Omega^e} &= b_2^e \boldsymbol{\gamma}_i
\end{aligned} \tag{A.2.2}$$

Then, the equation becomes:

$$\boldsymbol{\gamma}^T \begin{bmatrix} \int_{\Omega^e} b_2^e \alpha b_1^e \, d\Omega^e \boldsymbol{I} + \int_{\Omega^e} b_2^e \rho_f \boldsymbol{v}^c \cdot \nabla b_1^e \, d\Omega^e \boldsymbol{I} + \\ \mu_f \int_{\Omega^e} \nabla b_2^e \cdot \nabla b_1^e \, d\Omega^e \boldsymbol{I} + \mu_f \int_{\Omega^e} \nabla b_2^e \otimes \nabla b_1^e \, d\Omega^e \end{bmatrix} \boldsymbol{\beta} = \boldsymbol{\gamma}^T \int_{\Omega^e} b_2^e \bar{\boldsymbol{r}} \, d\Omega^e \tag{A.2.3}$$

Because $\boldsymbol{\beta}$ is arbitrary, we have

$$\boldsymbol{\beta} = \boldsymbol{K}^{-1} \boldsymbol{R} \tag{A.2.4}$$

Here,

$$\boldsymbol{K} = \int_{\Omega^e} b_2^e \alpha b_1^e \, d\Omega^e \boldsymbol{I} + \int_{\Omega^e} b_2^e \rho_f \boldsymbol{v}^c \cdot \nabla b_1^e \, d\Omega^e \boldsymbol{I} + \mu_f \int_{\Omega^e} \nabla b_2^e \cdot \nabla b_1^e \, d\Omega^e \boldsymbol{I} + \mu_f \int_{\Omega^e} \nabla b_2^e \otimes \nabla b_1^e \, d\Omega^e \tag{A.2.5}$$

$$\boldsymbol{R} = \int_{\Omega^e} b_2^e \bar{\boldsymbol{r}} \, d\Omega^e \tag{A.2.6}$$

We now reconstruct the fine-scale filed over the element domain as

$$\boldsymbol{v}' = b_1^e \boldsymbol{\beta} = b_1^e \boldsymbol{K}^{-1} \boldsymbol{R} \tag{A.2.7}$$

A.3. Solution of the coarse-scale problem with incompressible constraint

The coarse-scale problem (A.1.5) can be written as

$$\left\langle q, \, div \bar{\boldsymbol{v}} \right\rangle_\Omega - \left\langle \nabla q, \, \boldsymbol{v}' \right\rangle_\Omega = 0 . \tag{A.3.1}$$

Substitute $\boldsymbol{v}'$ from (A.2.7) to get

$$\left\langle q, \, div \bar{\boldsymbol{v}} \right\rangle_\Omega - \left\langle \nabla q, \, b_1^e \boldsymbol{K}^{-1} \boldsymbol{R} \right\rangle_\Omega = 0 . \tag{A.3.2}$$

Consider the second term on the left-hand side of (A.3.2)

$$
\begin{aligned}
-\left\langle \nabla q,\, \boldsymbol{v}' \right\rangle_{\Omega} &= -\left\langle \nabla q,\, b_1^e \boldsymbol{K}^{-1} \boldsymbol{R} \right\rangle_{\Omega} \\
&= -\left\langle \nabla q,\, b_1^e \boldsymbol{K}^{-1} \left(\int_{V^e} b_2^e \, dV^e \right) \bar{\boldsymbol{r}} \right\rangle_{\Omega} \\
&= -\left\langle \nabla q,\, \boldsymbol{\tau} \bar{\boldsymbol{r}} \right\rangle_{\Omega} \qquad .
\end{aligned} \tag{A.3.3}
$$

Here,

$$
\boldsymbol{\tau} = \left(b_1^e \int_{V^e} b_2^e \, dV^e \right) \left[\begin{array}{l} \int_{V^e} b_2^e \alpha b_1^e \, dV^e \boldsymbol{I} + \int_{V^e} b_2^e \rho_f \boldsymbol{v}^c \cdot \nabla b_1^e \, dV^e \boldsymbol{I} + \\ \mu_f \int_{V^e} \nabla b_2^e \cdot \nabla b_1^e \, dV^e \boldsymbol{I} + \mu_f \int_{V^e} \nabla b_2^e \otimes \nabla b_1^e \, dV^e \end{array} \right]^{-1} . \tag{A.3.4}
$$

Consequently, the coarse-scale equation (A.3.1) becomes

$$
\left\langle q,\, div \bar{\boldsymbol{v}} \right\rangle_{\Omega} + \left\langle \nabla q,\, \boldsymbol{\tau} \left(\alpha \bar{\boldsymbol{v}} + \rho_f \boldsymbol{v}^c \cdot \nabla \bar{\boldsymbol{v}} + \nabla p - 2\mu_f \nabla \bar{\boldsymbol{v}} - \boldsymbol{f} \right) \right\rangle_{\Omega} = \left\langle \nabla q,\, \boldsymbol{\tau} \boldsymbol{f} \right\rangle_{\Omega} . \tag{A.3.5}
$$

Now, extract the fine-scale velocity field from coarse-scale equation (A.1.6) as

$$
\left\{ \begin{array}{c} \left\langle \bar{\boldsymbol{w}}, \alpha \bar{\boldsymbol{u}} \right\rangle_{\Omega} + \left\langle \bar{\boldsymbol{w}}, \rho_f \boldsymbol{v}^c \cdot \nabla \bar{\boldsymbol{v}} \right\rangle_{\Omega} + \left\langle \nabla \bar{\boldsymbol{w}}, 2\mu_f \nabla \bar{\boldsymbol{v}} \right\rangle_{\Omega} - \left\langle div \bar{\boldsymbol{w}}, p \right\rangle_{\Omega} \\ + \left\langle \bar{\boldsymbol{w}}, \alpha \boldsymbol{v}' \right\rangle_{\Omega} + \left\langle \bar{\boldsymbol{w}}, \rho_f \boldsymbol{v}^c \cdot \nabla \boldsymbol{v}' \right\rangle_{\Omega} + \left\langle \nabla \boldsymbol{w}', 2\mu_f \nabla \bar{\boldsymbol{v}} \right\rangle_{\Omega} \end{array} \right\} = \left\langle \bar{\boldsymbol{w}},\, \boldsymbol{f} \right\rangle_{\Omega} + \left\langle \bar{\boldsymbol{w}}, \boldsymbol{t} \right\rangle_{\Gamma_N} . \tag{A.3.6}
$$

Applying integration by pars as

$$
\left\langle \bar{\boldsymbol{w}}, \rho_f \boldsymbol{v}^c \cdot \nabla \boldsymbol{v}' \right\rangle_{\Omega} = \left\langle \bar{\boldsymbol{w}}, \rho_f \left(\boldsymbol{v}^c \cdot \boldsymbol{n} \right) \boldsymbol{v}' \right\rangle_{\Gamma} - \left\langle \boldsymbol{v}^c \cdot \nabla \bar{\boldsymbol{w}}, \boldsymbol{v}' \right\rangle_{\Omega} \tag{A.3.7}
$$

$$
\left\langle \nabla \bar{\boldsymbol{w}}, 2\mu_f \nabla \boldsymbol{v}' \right\rangle_{\Omega} = \left\langle \nabla \bar{\boldsymbol{w}}, 2\mu_f \boldsymbol{v}' \right\rangle_{\Gamma} - \left\langle \Delta \bar{\boldsymbol{w}}, 2\mu_f \boldsymbol{v}' \right\rangle_{\Omega} \tag{A.3.8}
$$

Then the equation becomes

$$\left\{\begin{array}{c}\left\langle \bar{\boldsymbol{w}}, \alpha\bar{\boldsymbol{v}}\right\rangle_{\Omega} + \left\langle \bar{\boldsymbol{w}}, \rho_f \boldsymbol{v}^c \cdot \nabla\bar{\boldsymbol{v}}\right\rangle_{\Omega} + \left\langle \nabla\bar{\boldsymbol{w}}, 2\mu_f \nabla\bar{\boldsymbol{v}}\right\rangle_{\Omega} - \left\langle div\,\bar{\boldsymbol{w}}, p\right\rangle_{\Omega} \\ + \left\langle \bar{\boldsymbol{w}}, \alpha\boldsymbol{v}'\right\rangle_{\Omega} - \left\langle \boldsymbol{v}^c \cdot \nabla\bar{\boldsymbol{w}}, \boldsymbol{v}'\right\rangle_{\Omega} - \left\langle \Delta\bar{\boldsymbol{w}}, 2\mu_f \boldsymbol{v}'\right\rangle_{\Omega}\end{array}\right\} = \left\langle \bar{\boldsymbol{w}}, \boldsymbol{f}\right\rangle_{\Omega} + \left\langle \bar{\boldsymbol{w}}, \boldsymbol{t}\right\rangle_{\Gamma_N}$$

(A.3.9)

Substitute ***v***'

$$\begin{aligned}&\left\langle \bar{\boldsymbol{w}}, \alpha\boldsymbol{v}'\right\rangle_{\Omega} - \left\langle \boldsymbol{v}^c \cdot \nabla\bar{\boldsymbol{w}}, \boldsymbol{v}'\right\rangle_{\Omega} - \left\langle \Delta\bar{\boldsymbol{w}}, 2\mu_f \boldsymbol{v}'\right\rangle_{\Omega} \\ &\quad = \left\langle \left(-\alpha\bar{\boldsymbol{w}} + \boldsymbol{v}^c \cdot \nabla\bar{\boldsymbol{w}} + 2\mu_f \Delta\bar{\boldsymbol{w}}\right), -\boldsymbol{v}'\right\rangle_{\Omega} \\ &\quad = \left\langle \left(-\alpha\bar{\boldsymbol{w}} + \boldsymbol{v}^c \cdot \nabla\bar{\boldsymbol{w}} + 2\mu_f \Delta\bar{\boldsymbol{w}}\right), \boldsymbol{\tau}\left(-\boldsymbol{f} + \alpha\bar{\boldsymbol{u}} + \rho_f \boldsymbol{v}^c \cdot \nabla\bar{\boldsymbol{v}} - 2\mu_f \nabla\bar{\boldsymbol{v}} + \nabla p\right)\right\rangle_{\Omega}\end{aligned}$$

(A.3.10)

The weak form of the momentum equation finally becomes

$$\begin{aligned}&\left\langle \bar{\boldsymbol{w}}, \alpha\bar{\boldsymbol{u}}\right\rangle_{\Omega} + \left\langle \bar{\boldsymbol{w}}, \rho_f \boldsymbol{v}^c \cdot \nabla\bar{\boldsymbol{v}}\right\rangle_{\Omega} + \left\langle \nabla\bar{\boldsymbol{w}}, 2\mu_f \nabla\bar{\boldsymbol{v}}\right\rangle_{\Omega} - \left\langle div\,\bar{\boldsymbol{w}}, p\right\rangle_{\Omega} \\ &+ \left\langle \left(-\alpha\bar{\boldsymbol{w}} + \boldsymbol{v}^c \cdot \nabla\bar{\boldsymbol{w}} + 2\mu_f \Delta\bar{\boldsymbol{w}}\right), \boldsymbol{\tau}\left(\alpha\bar{\boldsymbol{v}} + \rho_f \boldsymbol{v}^c \cdot \nabla\bar{\boldsymbol{v}} - 2\mu_f \nabla\bar{\boldsymbol{v}} + \nabla p\right)\right\rangle_{\Omega} \\ &\quad = \left\langle \bar{\boldsymbol{w}}, \boldsymbol{f}\right\rangle_{\Omega} + \left\langle \bar{\boldsymbol{w}}, \boldsymbol{t}\right\rangle_{\Gamma_N} + \left\langle -\alpha\bar{\boldsymbol{w}} + \boldsymbol{v}^c \cdot \nabla\bar{\boldsymbol{w}} + 2\mu_f \Delta\bar{\boldsymbol{w}}, \boldsymbol{\tau}\boldsymbol{f}\right\rangle_{\Omega}\end{aligned}$$

(A.3.11)

Here, the stabilization tensor is given by (A.3.4).

BIBLIOGRAPHY

[1] M. P. Bendsøe and N. Kikuchi, "Generating Optimal Topologies in Structural Design Using a Homogenization Method," *Computer Methods in Applied Mechanics and Engineering*, vol. 71, pp. 197-224, 1988.

[2] G. H. Kim, *et al.*, *Battery thermal management system design modeling*: National Renewable Energy Laboratory, 2006.

[3] S. Al-Hallaj and J. Selman, "Thermal modeling of secondary lithium batteries for electric vehicle/hybrid electric vehicle applications," *Journal of power sources*, vol. 110, pp. 341-348, 2002.

[4] K. Shukuya, *et al.*, "A New Battery System for the Estima Hybrid Minivan," 2002.

[5] M. G. Gavali, *et al.*, "Optimization of Water Jacket Using CFD for Effective Cooling of Water-Cooled Diesel Engines," presented at the Symposium on International Automotive Technology, 2007.

[6] S. Shih, *et al.*, "Engine knock toughness improvement through water jacket optimization," presented at the Powertrain & Fluid Systems Conference & Exhibition, 2003.

[7] J. Ye, *et al.*, "Coolant Flow Optimization in a Racing Cylinder Block and Head Using Cfd Analysis and Testing," in *Motorsports Engineering Conference & Exposition*, 400 Commonwealth Dr , Warrendale, PA, 15096, USA, 2004.

[8] G. Cantore, *et al.*, "Optimization of a cooling circuit in an internal combustion engine for marine applications," presented at the Internation Conference on Engines for Automobile, 2005.

[9] N. León, *et al.*, "Automatic shape variations for optimization and innovation, Shape Optimization of Cylinderhead Gasket using CFD," *IFIP International Federation for Information Processing*, vol. 250, p. 179, 2007.

[10] F. Farina, *et al.*, "Thermal design of integrated motor drives for traction applications," in *Power Electronics and Applications, 2005 European Conference on*, 2005, pp. 10 pp.-P.10.

[11] Z. Ping, *et al.*, "Research on the Cooling System of a 4QT Prototype Machine Used for HEV," *Energy Conversion, IEEE Transactions on*, vol. 23, pp. 61-67, 2008.

[12] I. Khorunzhii, *et al.*, "Modelling of a pin-fin heat converter with fluid cooling for power semiconductor modules," *International Journal of Energy Research*, vol. 27, pp. 1015-1026, 2003.

[13] K. Park, *et al.*, "Numerical shape optimization for high performance of a heat sink with pin-fins," *Numerical Heat Transfer Part A: Applications*, vol. 46, pp. 909-927, 2004.

[14] Y.-T. Yang and H.-S. Peng, "Numerical study of pin-fin heat sink with un-uniform fin height design," *International Journal of Heat and Mass Transfer*, vol. 51, pp. 4788-4796, 2008.

[15] Y.-T. Yang and H.-S. Peng, "Numerical study of the heat sink with un-uniform fin width designs," *International Journal of Heat and Mass Transfer*, vol. 52, pp. 3473-3480, 2009.

[16] K.-S. Lee, *et al.*, "Optimal shape and arrangement of staggered pins in the channel of a plate heat exchanger," *International Journal of Heat and Mass Transfer*, vol. 44, pp. 3223-3231, 2001.

[17] K. Park and D.-H. Choi, "Shape Optimization of a plate-fin type heat sink with triangular-shaped vortex generator," *Journal of Mechanical Science and Technology*, vol. 18, pp. 1590-1603, 2004.

[18] K. Park, *et al.*, "The application of the CFD and Kriging method to an optimization of heat sink," *International Journal of Heat and Mass Transfer*, vol. 49, pp. 3439-3447, 2006.

[19] A. Husain and K. Kwang-Yong, "Shape Optimization of Micro-Channel Heat Sink for Micro-Electronic Cooling," *Components and Packaging Technologies, IEEE Transactions on*, vol. 31, pp. 322-330, 2008.

[20] C. Silva, *et al.*, "Optimization of Fin Performance in a Laminar Channel Flow Through Dimpled Surfaces," *Journal of Heat Transfer*, vol. 131, pp. 021702-9, 2009.

[21] A. Samad, *et al.*, "Multi-objective optimization of a dimpled channel for heat transfer augmentation," *Heat and Mass Transfer*, vol. 45, pp. 207-217, 2008.

[22] D. Kuhl, *et al.*, "Structural optimization of rocket engine cooling channels," presented at the AIAA/ASME/SAE/ASEE Joint Propulsion Conference and Exhibit, 34th, Cleveland, OH, 1988.

[23] D. Balagangadhar and S. Roy, "Design sensitivity analysis and optimization of steady fluid-thermal systems," *Computer Methods in Applied Mechanics and Engineering*, vol. 190, pp. 5465-5479, 2001.

[24] C.-H. Cheng and M.-H. Chang, "Shape design for a cylinder with uniform temperature distribution on the outer surface by inverse heat transfer method," *International Journal of Heat and Mass Transfer*, vol. 46, pp. 101-111, 2003.

[25] S. Tiwari, *et al.*, "Heat transfer enhancement in cross-flow heat exchangers using oval tubes and multiple delta winglets," *International Journal of Heat and Mass Transfer*, vol. 46, pp. 2841-2856, 2003.

[26] G. Fabbri, "Heat transfer optimization in corrugated wall channels," *International Journal of Heat and Mass Transfer*, vol. 43, pp. 4299-4310, 2000.

[27] R. Hilbert, *et al.*, "Multi-objective shape optimization of a heat exchanger using parallel genetic algorithms," *International Journal of Heat and Mass Transfer*, vol. 49, pp. 2567-2577, 2006.

[28] R. S. Matos, *et al.*, "Optimally staggered finned circular and elliptic tubes in forced convection," *International Journal of Heat and Mass Transfer*, vol. 47, pp. 1347-1359, 2004.

[29] E. Nobile, *et al.*, "Geometric Parameterization and Multiobjective Shape Optimization of Convective Periodic Channels," *Numerical Heat Transfer Part B: Fundamentals*, vol. 50, pp. 425-453, 2006.

[30] M. Manzan, *et al.*, "Multi-objective Optimization for Problems Involving Convective Heat Transfer," in *Optimization and Computational Fluid Dynamics*, ed, 2008, pp. 217-266.

[31] E. Duplain and B. R. Baliga, "Computational optimization of the thermal performance of internally finned ducts," *International Journal of Heat and Mass Transfer,* vol. 52, pp. 3929-3942, 2009.

[32] G. Fabbri, "Heat transfer optimization in internally finned tubes under laminar flow conditions," *International Journal of Heat and Mass Transfer,* vol. 41, pp. 1243-1253, 1998.

[33] G. Fabbri, "Effect of viscous dissipation on the optimization of the heat transfer in internally finned tubes," *International Journal of Heat and Mass Transfer,* vol. 47, pp. 3003-3015, 2004.

[34] B. Mohammadi and O. Pironneau, *Applied shape optimization for fluids*: Oxford University Press, USA, 2001.

[35] M. P. Bendsøe and O. Sigmund, *Topology optimization: theory, method and applications*: Springer, 2003.

[36] O. Sigmund and J. Petersson, "Numerical instabilities in topology optimization: A survey on procedures dealing with checkerboards, mesh-dependencies and local minima," *Structural and Multidisciplinary Optimization,* vol. 16, pp. 68-75, 1998.

[37] C. S. Jog and R. B. Haber, "Stability of finite element models for distributed-parameter optimization and topology design," *Computer Methods in Applied Mechanics and Engineering,* vol. 130, pp. 203-226, 1996.

[38] G. W. Jang, *et al.*, "Topology optimization using non-conforming finite elements: three-dimensional case," *International Journal for Numerical Methods in Engineering,* vol. 63, pp. 859-875, 2005.

[39] T. Borrvall and J. Petersson, "Topology optimization of fluids in Stokes flow," *International Journal for Numerical Methods in Fluids,* vol. 41, pp. 77-107, Jan 2003.

[40] A. Bejan and D. A. Nield, *Convection in Porous Media*. New York: Springer, 1999.

[41] I. Ramiere, *et al.*, "Fictitious domain methods to solve convection-diffusion problems with general boundary conditions," presented at the AIAA Computational Fluid Dynamics Conference, Toronto, Ontario Canada, 2005.

[42] K. Khadra, *et al.*, "Fictitious domain approach for numerical modelling of Navier-Stokes equations," *International Journal for Numerical Methods in Fluids,* vol. 34, pp. 651-684, Dec 30 2000.

[43] P. Angot, *et al.*, "A penalization method to take into account obstacles in incompressible viscous flows," *Numerische Mathematik,* vol. 81, pp. 497-520, Feb 1999.

[44] P. Angot, "Analysis of singular perturbations on the brinkman problem for fictitious domain models of viscous flows," *Mathematical Methods in the Applied Sciences,* vol. 22, pp. 1395-1412, Nov 10 1999.

[45] N. Wiker, *et al.*, "The Darcy-Stokes Topology Optimization Problem," in *IUTAM Symposium on Topological Design Optimization of Structures, Machines and Materials*, ed, 2006, pp. 551-558.

[46] N. Wiker, *et al.*, "Topology optimization of regions of Darcy and Stokes flow," *International Journal for Numerical Methods in Engineering,* vol. 69, pp. 1374-1404, Feb 12 2007.

[47] A. Gersborg-Hansen, *et al.*, "Topology optimization of channel flow problems," *Structural and Multidisciplinary Optimization,* vol. 30, p. 181, 2005.

[48] A. Gersborg-Hansen, *et al.*, *Topology Optimization of Mass Distribution Problems in Stokes Flow* vol. 137: Springer Netherlands, 2006.

[49] L. H. Olesen, *et al.*, "Topology optimization of Navier-Stokes flow in microfluidics," in *European Congress on Computational Methods in Applied Sciences and Engineering*, 2004, p. 224.

[50] L. H. Olesen, *et al.*, "A high-level programming-language implementation of topology optimization applied to steady-state Navier-Stokes flow," *International Journal for Numerical Methods in Engineering,* vol. 65, pp. 975-1001, Feb 12 2006.

[51] N. Aage, *et al.*, "Topology optimization of large scale stokes flow problems," *Structural and Multidisciplinary Optimization,* vol. 35, pp. 175-180, Feb 2008.

[52] T.-C. Liang, "Cutoffs in chaotic map mixing and topology optimization of microfluidic channels," The department of Aeronautics and Astronautics, Stanford University, 2008.

[53] C. S. Andreasen, *et al.*, "Topology optimization of microfluidic mixers," *International Journal for Numerical Methods in Fluids*, 2008.

[54] F. Okkels and H. Bruus, "Scaling behavior of optimally structured catalytic microfluidic reactors," *Physical Review E*, vol. 75, Jan 2007.

[55] G. H. Yoon, "Topology Optimization for Stationary Fluid-Structure Interaction Problems Using a New Monolithic Formulation," presented at the 8th. World Congress on Computational Mechanics (WCCM8), Lisbon, Portugal, 2009.

[56] G. Pingen, *et al.*, "3 D Topology Optimization of Fluids by the Lattice Boltzmann Method," *11 th AIAA/ISSMO Multidisciplinary Analysis and Optimization Conference*, 2006.

[57] G. Pingen, *et al.*, "Topology optimization of flow domains using the lattice Boltzmann method," *Structural and Multidisciplinary Optimization*, vol. 34, pp. 507-524, Dec 2007.

[58] X. B. Duan, *et al.*, "Optimal shape control of fluid flow using variational level set method," *Physics Letters A*, vol. 372, pp. 1374-1379, Feb 25 2008.

[59] X. B. Duan, *et al.*, "Shape-topology optimization of stokes flow via variational level set method," *Applied Mathematics and Computation*, vol. 202, pp. 200-209, Aug 2008.

[60] X.-B. Duan, *et al.*, "Shape-topology optimization for Navier-Stokes problem using variational level set method," *Journal of Computational and Applied Mathematics*, vol. 222, pp. 487-499, 2008.

[61] P. Häußler, *et al.*, "Topology and Shape Optimization Methods for CFD Problems," in *24th CADFEM Users'Meeting 2006, International Congress on FEM Technology*, 2006.

[62] C. Othmer, *et al.*, "Computation of topological sensitivities in fluid dynamics: cost function versatility," in *European Conference on Computational Fluid Dynamics*, 2006.

[63] A. Donoso and O. Sigmund, "Topology optimization of multiple physics problems modelled by Poisson's equation," *Latin American Journal of Solids and Structures* vol. 1, pp. 169-189, 2004.

[64] T. Gao, *et al.*, "Topology optimization of heat conduction problem involving design-dependent effect," *CJK-OSM 4: The Fourth China-Japan-Korea Joint Symposium on Optimization of Structural and Mechanical Systems,* pp. 291-296, 2006.

[65] T. Gao, *et al.*, "Topology optimization of heat conduction problem involving design-dependent heat load effect," *Finite Elements in Analysis and Design,* vol. 44, pp. 805-813, 2008.

[66] A. Gersborg-Hansen, *et al.*, "Topology optimization of heat conduction problems using the finite volume method," *Structural and Multidisciplinary Optimization,* vol. 31, pp. 251-259, Apr 2006.

[67] S. H. Ha, *et al.*, "Level set based topological shape optimization of nonlinear heat conduction problem using explicit boundary," *CJK-OSM 4: The Fourth China-Japan-Korea Joint Symposium on Optimization of Structural and Mechanical Systems,* pp. 119-124, 2006.

[68] T. E. Bruns, "Topology optimization of convection-dominated, steady-state heat transfer problems," *International Journal of Heat and Mass Transfer,* vol. 50, pp. 2859-2873, 2007.

[69] S. Heo, *et al.*, "The robust design for micro electro-thermal actuators," *Smart Structures and Materials 2004: Smart Electronics, Mems, Biomems and Nanotechnology,* vol. 5389, pp. 241-247, 2004.

[70] G. H. Yoon and Y. Y. Kim, "The element connectivity parameterization formulation for the topology design optimization of multiphysics systems," *International Journal for Numerical Methods in Engineering,* vol. 64, pp. 1649-1677, 2005.

[71] H. Moon, *et al.*, "Reliability-based topology optimization of thermal systems considering convection heat transfer," in *10th AIAA/ISSMO Multidisciplinary Analysis and Optimization Conference*, Albany, New York, 2004.

[72] S. Y. Yoo and Y. Y. Kim, "The Topology Optimization of Three-dimensional Cooling Fins by the Internal Element Connectivity Parameterization Method," 2007.

[73] A. Iga, *et al.*, "Topology optimization for thermal conductors considering design-dependent effects, including heat conduction and convection," *International Journal of Heat and Mass Transfer,* vol. 52, pp. 2721-2732, 2009.

[74] B.-C. Chen and N. Kikuchi, "Topology optimization with design-dependent loads," *Finite Elements in Analysis and Design,* vol. 37, pp. 57-70, 2001.

[75] J. Donea and A. Huerta, *Finite element methods for flow problems*: John Wiley & Sons Inc, 2003.

[76] J. N. Reddy and D. K. Gartling, *The finite element method in heat transfer and fluid dynamics*: CRC, 2010.

[77] A. N. Brooks and T. J. R. Hughes, "Streamline upwind/Petrov-Galerkin formulations for convection dominated flows with particular emphasis on the incompressible Navier-Stokes equations," *Computer Methods in Applied Mechanics and Engineering,* vol. 32, pp. 199-259, 1982.

[78] T. J. R. Hughes and A. Brooks, "A multidimensional upwind scheme with no crosswind diffusion," *Finite element methods for convection dominated flows,* vol. 34, pp. 19-35, 1979.

[79] T. E. Tezduyar, "Stabilized Finite-Element Formulations for Incompressible-Flow Computations," *Advances in Applied Mechanics, Vol 28,* vol. 28, pp. 1-44, 1992.

[80] T. E. Tezduyar, *et al.*, "Incompressible-Flow Computations with Stabilized Bilinear and Linear Equal-Order-Interpolation Velocity-Pressure Elements," *Computer Methods in Applied Mechanics and Engineering,* vol. 95, pp. 221-242, Mar 1992.

[81] T. J. R. Hughes and L. P. Franca, "A new finite element formulation for computational fluid dynamics: VII. The Stokes problem with various well-posed boundary conditions: symmetric formulations that converge for all velocity/pressure spaces," *Computer Methods in Applied Mechanics and Engineering,* vol. 65, pp. 85-96, 1987.

[82] T. J. R. Hughes, *et al.*, "A new finite element formulation for computational fluid dynamics: V. Circumventing the Babuska-Brezzi condition: A stable Petrov-Galerkin formulation of the Stokes problem accommodating equal-order interpolations," *Computer Methods in Applied Mechanics and Engineering,* vol. 59, pp. 85-99, 1986.

[83] T. J. R. Hughes, *et al.*, "A new finite element formulation for computational fluid dynamics: VIII. The Galerkin/least-squares method for advective-diffusive equations," *Computer Methods in Applied Mechanics and Engineering,* vol. 73, pp. 173-189, 1989.

[84] T. J. Hughes and T. E. Tezduyar, "Finite element methods for first-order hyperbolic systems with particular emphasis on the compressible Euler equations, Comput," *Methods Appl. Mech. and Engrg,* vol. 45, p. 217?284, 1984.

[85] T. J. R. Hughes, "Multiscale Phenomena - Greens-Functions, the Dirichlet-to-Neumann Formulation, Subgrid Scale Models, Bubbles and the Origins of Stabilized Methods," *Computer Methods in Applied Mechanics and Engineering,* vol. 127, pp. 387-401, Nov 1995.

[86] A. Masud and T. J. R. Hughes, "A stabilized mixed finite element method for Darcy flow," *Computer Methods in Applied Mechanics and Engineering,* vol. 191, pp. 4341-4370, 2002.

[87] A. Masud, "A stabilized mixed finite element method for Darcy-Stokes flow," *International Journal for Numerical Methods in Fluids,* vol. 54, pp. 665-681, Jun-Jul 2007.

[88] A. Masud and R. A. Khurram, "A multiscale/stabilized finite element method for the advection-diffusion equation," *Computer Methods in Applied Mechanics and Engineering,* vol. 193, pp. 1997-2018, 2004.

[89] G. Hauke and A. Garcia-Olivares, "Variational subgrid scale formulations for the advection-diffusion-reaction equation," *Computer Methods in Applied Mechanics and Engineering,* vol. 190, pp. 6847-6865, 2001.

[90] A. Masud and R. Khurram, "A multiscale finite element method for the incompressible Navier-Stokes equations," *Computer Methods in Applied Mechanics and Engineering,* vol. 195, pp. 1750-1777, 2006.

[91] T. Tezduyar and Y. Park, "Discontinuity-capturing finite element formulations for nonlinear convection-diffusion-reaction equations," *Computer Methods in Applied Mechanics and Engineering,* vol. 59, pp. 307-325, 1986.

[92] G. Le Beau and T. Tezduyar, "Finite element computation of compressible flows with the SUPG formulation," *Advances in finite element analysis in fluid dynamics, FED,* vol. 123, pp. 21-27, 1991.

[93] T. E. Tezduyar and Y. Osawa, "Finite element stabilization parameters computed from element matrices and vectors," *Computer Methods in Applied Mechanics and Engineering,* vol. 190, pp. 411-430, 2000.

[94] T. Tezduyar and S. Sathe, "Stabilization parameters in SUPG and PSPG formulations," *Journal of computational and applied mechanics,* vol. 4, pp. 71-88, 2003.

[95] F. Shakib, *et al.*, "A New Finite-Element Formulation for Computational Fluid-Dynamics .10. The Compressible Euler and Navier-Stokes Equations," *Computer Methods in Applied Mechanics and Engineering,* vol. 89, pp. 141-219, Aug 1991.

[96] T. E. Tezduyar, "Finite elements in fluids: Stabilized formulations and moving boundaries and interfaces," *Computers & Fluids,* vol. 36, pp. 191-206, Feb 2007.

[97] R. Codina, "On stabilized finite element methods for linear systems of convection–diffusion-reaction equations," *Computer Methods in Applied Mechanics and Engineering,* vol. 188, pp. 61-82, 2000.

[98] R. Codina, "A stabilized finite element method for generalized stationary incompressible flows," *Computer Methods in Applied Mechanics and Engineering,* vol. 190, pp. 2681-2706, 2001.

[99] Q. Liu and O. V. Vasilyev, "A Brinkman penalization method for compressible flows in complex geometries," *Journal of Computational Physics,* vol. 227, pp. 946-966, 2007.

[100] A. Evgrafov, "The limits of porous materials in the topology optimization of stokes flows," *Applied Mathematics and Optimization,* vol. 52, pp. 263-277, Nov-Dec 2005.

[101] J. K. Guest and J. H. Prevost, "Topology optimization of creeping fluid flows using a Darcy-Stokes finite element," *International Journal for Numerical Methods in Engineering,* vol. 66, pp. 461-484, Apr 16 2006.

[102] J. K. Guest and J. H. Prevost, "Optimizing multifunctional materials: Design of microstructures for maximized stiffness and fluid permeability," *International Journal of Solids and Structures,* vol. 43, pp. 7028-7047, Nov 2006.

[103] M. Ismail, *et al.*, "A CFD-based experimental analysis on the effect of free stream cooling on the performance of micro processor heat sinks," *International Communications in Heat and Mass Transfer,* vol. 35, pp. 771-778, 2008.

[104] X. Yu, *et al.*, "Development of a plate-pin fin heat sink and its performance comparisons with a plate fin heat sink," *Applied thermal engineering,* vol. 25, pp. 173-182, 2005.

[105] S. C. Lin and C. L. Huang, "An integrated experimental and numerical study of forward-curved centrifugal fan," *Experimental Thermal and Fluid Science,* vol. 26, pp. 421-434, 2002.

[106] A. Evgrafov, "Topology optimization of slightly compressible fluids," *Zamm-Zeitschrift Fur Angewandte Mathematik Und Mechanik,* vol. 86, pp. 46-62, Jan 2006.

[107] J. Heinrich and C. Vionnet, "The penalty method for the Navier-Stokes equations," *Archives of Computational Methods in Engineering,* vol. 2, pp. 51-65, 1995.

[108] J. C. Heinrich and D. W. Pepper, *Intermediate finite element method: fluid flow and heat transfer applications* vol. 1: Hemisphere Pub, 1999.

[109] T. E. Tezduyar, *et al.*, "Stabilized formulations for incompressible flows with thermal coupling," *International Journal for Numerical Methods in Fluids,* vol. 57, pp. 1189-1209, Jul 30 2008.

[110] C. Ramon, "On stabilized finite element methods for linear systems of convection–diffusion-reaction equations," *Computer Methods in Applied Mechanics and Engineering,* vol. 188, pp. 61-82, 2000.

[111] A. Masud and J. Kwack, "A stabilized mixed finite element method for the first-order form of advection-diffusion equation," *International Journal for Numerical Methods in Fluids,* vol. 57, pp. 1321-1348, Jul 30 2008.

[112] D. K. Gartling, *et al.*, "Simulation of coupled viscous and porous flow problems," *International Journal of Computational Fluid Dynamics,* vol. 7, pp. 23-&, 1996.

[113] H. A. Eschenauer and N. Olhoff, "Topology optimization of continuum structures: A review," *Applied Mechanics Reviews,* vol. 54, p. 331, 2001.

[114] P. Michaleris, *et al.*, *Tangent Operators and Design Sensitivity Formulations for Transient Nonlinear Coupled Problems with Applications to Elasto-plasticity*: Theoretical and Applied Mechanics, University of Illinois at Urbana-Champaign, 1993.

[115] M. Bendsøe and O. Sigmund, *Topology optimization: theory, methods, and applications*: Springer Verlag, 2003.

[116] T. Borrvall and J. Petersson, "Topology optimization using regularized intermediate density control," *Computer Methods in Applied Mechanics and Engineering,* vol. 190, pp. 4911-4928, 2001.

[117] B. Bourdin, "Filters in topology optimization," *International Journal for Numerical Methods in Engineering,* vol. 50, pp. 2143-2158, Mar 30 2001.

[118] A. Gersborg-Hansen, "Topology optimization of flow problems," Ph.D. thesis, Department of Mathmatics, Technical University of Denmark, 2007.

[119] A. Gersborg-Hansen, *et al.*, "Topology optimization of channel flow problems," *Structural and Multidisciplinary Optimization,* vol. 30, pp. 181-192, Sep 2005.

[120] N. Wiker, *et al.*, "The Darcy-Stokes topology optimization problem," *IUTAM Symposium on Topological Design Optimization of Structures, Machines and Materials: Status and Perspectives,* vol. 137, pp. 551-558, 2006.

[121] O. Pironneau, "On optimum design in fluid mechanics," *Journal of Fluid Mechanics Digital Archive,* vol. 64, pp. 97-110, 1974.

[122] O. Sigmund, "Morphology-based black and white filters for topology optimization," *Structural and Multidisciplinary Optimization*, vol. 33, pp. 401-424, 2007.

[123] Q. Li, *et al.*, "Evolutionary topology optimization for temperature reduction of heat conducting fields," *International Journal of Heat and Mass Transfer*, vol. 47, pp. 5071-5083, Nov 2004.

[124] J. Lee, *et al.*, "Topology optimization of switched reluctance motors for the desired torque profile," *Structural and Multidisciplinary Optimization*, pp. 1-14, 2010.